# TWO PARTICLE CORRELATIONS AND EXCITED STATE POPULATIONS IN NUCLEUS-NUCLEUS COLLISIONS

By

Fan Zhu

A DISSERTATION

Submitted to
Michigan State University
in partial fulfillment of the requirements
for the Degree of

DOCTOR OF PHILOSOPHY

Department of Physics and Astronomy

1992

ABSTRACT

TWO PARTICLE CORRELATIONS AND EXCITED STATE POPULATIONS IN NUCLEUS-NUCLEUS COLLISIONS

By

Fan Zhu

Two particle correlation functions and excited state populations were measured for the $^{3}$He + Ag reactions at E/A=67 MeV and the $^{36}$Ar + $^{197}$Au reactions at E/A=35 MeV. In the former experiment, measurements were performed with a position sensitive high resolution hodoscope as a standalone device. In the latter experiment, measurements were performed by combining the high resolution hodoscope with the Miniball, a $4\pi$ multifragment detection array.

These two experiments addressed several outstanding problems in the interpretation of two particle correlation functions and emission temperatures. For the $^{3}$He + Ag reactions at E/A=67 MeV, $p-p$ and $d-\alpha$ correlation functions were measured to address the scaling of two particle correlation functions with the size of the projectile. These measurements revealed that the correlation functions for charged particles scale naturally with the radius of the projectile, consistent with an emission volume which is initially defined by the overlap of a much smaller projectile with a much larger target. The radii extracted from $d-\alpha$ correlations were much smaller than the ones extracted from $p-p$ correlations, an effect which may be related to the fact that deuterons and $\alpha$ particles have shorter mean free paths within the nuclear medium. The populations of excited states were also measured at forward and at

backward angles in order to compare the emission temperatures for pre-equilibrium and equilibrium emission mechanisms. A low emission temperature of about 1 MeV was obtained for $^{6}$Li particles evaporated at backward angles. This low temperature was consistent, however, with a hybrid pre-equilibrium transport and equilibrium evaporation model. Much larger temperature of about 4 MeV were observed for pre-equilibrium processes measured at forward angles.

Impact parameter selected excited state populations were measured for $^{36}$Ar + $^{197}$Au reactions at E/A=35 MeV in order to better understand the population inversions observed in a previous measurement of $^{14}$N + Ag reactions at E/A=35 MeV. These impact parameter selected measurements revealed such population inversions to be an effect most prominent in low multiplicity peripheral reactions. When the multiplicity of charge particles is increased to the value consistent with central collisions, the excited state population approaches the statistical model predictions for T $\approx$ 4 MeV.

To my wife

*Jia Lu*

# ACKNOWLEDGMENTS

First and foremost, I would like to express my sincere thanks to my thesis adviser, Prof. Bill Lynch. His guidance, support and encouragement are absolutely crucial for the finish of this dissertation. His deep understanding of physics problems, both experimental and theoretical; his attitude about doing physics research, paying attention to every details; his persistence on getting a problem fixed, a project done, have a profound influence on my career. Special thanks go to Prof. Konrad Gelbke for his interest in my research and career. His invaluable advice and suggestions benefited a lot to me for finishing my thesis work and gave me more confidence.

I want to express my gratitude to other members of my guidance committee, Prof. Alex Brown, Prof. Phillip Duxebury, Prof. S.D. Mahanti, and Prof. Daniel Stump. Their generous advice and suggestions on the thesis are appreciated.

A lot of people have helped and collaborated on my thesis experiments and their analysis one way or the other. It would not be possible to get my thesis done without the help of the following people, whom I owe a great deal for their help and their friendship, W. Bauer, D.R. Bowman, J. Dinius, W.G. Gong, Y.D. Kim, T. Murakami, T.K. Nayak, R. Pelak, L. Phair, R.T. de Souza, M.B. Tsnag, C. Williams, and H.M. Xu from National Superconducting Cyclotron Laboratory of Michigan State University; K. Kwiakowski, R. Planeta, S. Rose, V.E. Viola, Jr., L.W. Woo, S. Yennello, and J. Zhang from Indiana University Cyclotron Facility. Special thanks go to Dr. M.B. Tsang and Dr. T. Murakami for their help and patience while I was a fresh graduate student just starting to work on my thesis.

There are many fellow graduate students and post-doctors whom I have enjoyed working and living together, Y. Chen, Z. Chen, M. Gong, N. Ju, B. Li, T. Li, M. Lisa, G. Peaslee, X. Wu, L. Zhao, G. Zheng and the name goes on, you know who

you are, I thank you all. For the other three of the 1985 CUSPEA "the gang of four" at MSU, W. Gong, Y. Li, and B.Pi, the good memories will last forever.

I give my thanks to the Physics Department and the Cyclotron Laboratory for giving me the financial support during my graduate study for my degree. I want to express my thanks to all the staff members of the laboratory, especially J. Youkon, D. Swan, and J. Ottarson.

Last but not the least, I appreciate the understanding and love of my parents in China. Their high expectation for me is always a long lasting motivation to work harder and achieve higher goals. I owe a great debt to my beloved wife, Jia Lu, for enduring the hardship of a graduate student, and giving me love and affection to carry through.

# Contents

# List of Figures

# List of Tables

# Chapter 1

# Introduction

## 1.1 Overview

For low incident energies, the reactions between target and projectile nuclei happen slowly and can be frequently separated into two steps, the formation of a compound nucleus and the subsequent particle emission from this compound nucleus [Bohr 36]. Experimentally measured particles thus mainly reflect this later stage of the reaction, in which one has a fully equilibrated compound nucleus. In more energetic intermediate energy nuclear reactions, this two step reaction assumption is not valid any longer. Particle emission process occurs throughout the reaction, as the system evolves from initial contact to a fully equilibrated residue. Because two particle correlation functions are sensitive to the space-time extent of the reaction region, such measurements have been used extensively to study the space-time evolution of the nuclear reaction [Gelb 87, Boal 90b]. These measurements generally reveal larger measured correlation functions for higher energy particles corresponding to smaller source sizes, and smaller correlation functions for lower energy particles corresponding to larger source sizes. Such observations are consistent with the emission of more energetic particles during the earlier stages of the nuclear reaction, where the source size more closely approximates the overlap volume of the projectile and target nuclei and the emission

of lower energy particles during later stages of the nuclear reaction when the system becomes equilibrated and the source size and lifetime are much larger. If this interpretation is correct, such energy dependences should be most dramatic for light ion induced reactions on heavy targets, due to the extreme difference between the small size of the initial configurations involving the overlap of projectile and the target, and the much larger size of the equilibrated target-like residue. Contrary to this simple picture, comparison of two proton correlation function for p and $^{14}N$ induced reactions on a Ag target, displayed no sensitivity to the size of projectile, casting serious doubt upon the connection between the correlation function and source size [Cebr 89]. These measurements, however, included all protons above threshold, and were therefore dominated by low energy protons which may contain large contributions from compound nuclear evaporation processes. In this dissertation, I present measurements of the $^{3}He + Ag$ reaction at $E_{beam}$=200 MeV, which have helped to resolve this controversy [Zhu 91].

The investigation of the properties of nuclear matter at high temperature and density ($T > 0, \rho > \rho_0$) is a primary motivation for measurements of heavy ion reactions. If local thermal equilibrium is achieved in a nuclear reaction, the temperature of the excited nuclear system can be obtained from measurements of the population of excited states. Systematic studies of the incident energy dependence of the excited state populations over an energy range of $E/A = 20 - 200MeV$ were consistent with a gradual increase in temperature with incident energy in the range of 3-5 MeV [Gelb 87, Chen 87a]. A recent test of the concept of local thermal equilibrium, however, revealed population inversion in the excited states of $^{10}B$ nuclei emitted in the $^{14}N$ + Ag reaction at $E/A = 35MeV$, in addition to non-thermal populations for many other intermediate mass fragments [Naya 89, Naya 92]. It is conceivable that this effect may be primarily due to contributions from peripheral reactions which

may be dominated by non-equilibrium transport phenomena [Awes 84, Vand 84]. In my second thesis experiment, we measured $^{36}Ar + ^{197}Au$ reactions at E/A=35 MeV, using the Miniball $4\pi$ array as a reaction filter in order to investigate whether these non-thermal excited state populations disappear for central collisions [Zhu 92].

## 1.2 Intensity Interferometry

When two identical particles are emitted from a source at small relative momenta, their wavefunction will manifest interference effects. These effects stem from the quantum symmetry of the wavefunction with respect to particle exchange; their nature depends upon whether the particles obey Bose-Einstein or Fermi-Dirac statistics. These identical particle effects are sensitive to the phase space proximity of the two particles and therefore are not only sensitive to their relative momentum, but also to their spatial proximity and the time of emission from the source. Hanbury-Brown and Twiss (HBT) were the first to take advantage of these interference effects and developed a two photon intensity interferometry method in 1956 to measure the diameter of bright visual stars [HBT 56]. Since then, this method has been extended to measurements in nuclear physics and particle physics to measure the space time extent of sources for particle emission [Boal 90b].

The intensity interferometry method was first applied to nuclear or particle physics by Goldhaber et al in 1960 to the interpretation of correlation between identical pions [Gold 60]. Early theoretical investigations of pion correlations were carried out by Kopylov [Kopy 74]. Later on, measurements of pion correlations in reactions between complex nuclei were performed by a number of investigators [Fung 78, Zajc 84, Gelb 87, Boal 90a]. To illustrate how one can extract a source size from this method, let's consider this example of pion interferometry as indicated in the schematic dia-

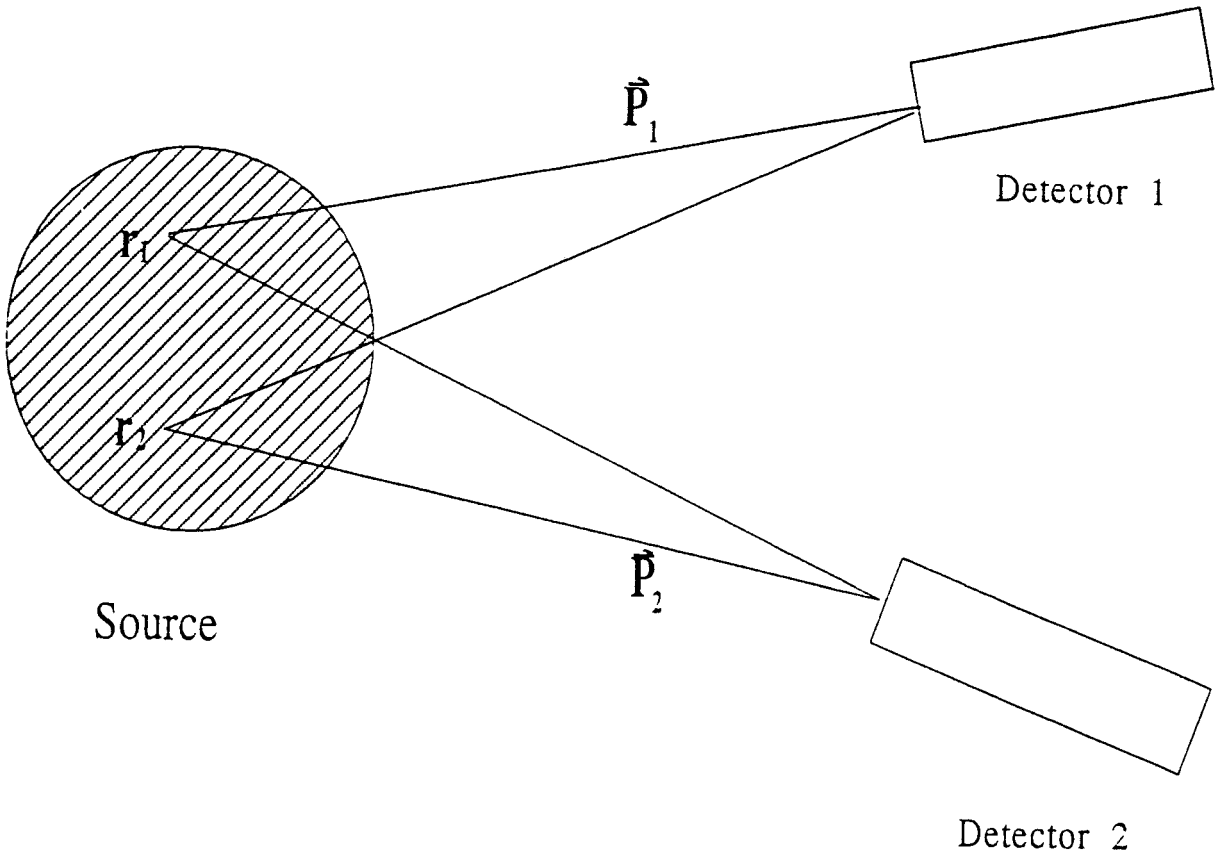


Figure 1.1: Schematic diagram showing intensity interferometry. It is sensitive to the source size and life time.

gram in Figure 1.1. Let's assume that two pions are detected from the same reaction event in coincidence, and $\rho(x,p) = \rho(x)\cdot P(p)$ be the impact parameter averaged space time probability distribution of pion emission with momentum p from the reaction; here, both x and p are four vectors, $x = (\vec{r},t), p = (\vec{p},E)$. $P(p)$ is the probability of detecting pion with momentum p in singles. If the two pions are emitted incoherently at space time points $x_1, x_2$, the joint probability $P(p_1,p_2)$ of observing the two pions with momentum $p_1$ and $p_2$ is frequently approximated by the overlap of their individual probability distributions and their final state wave function.

$$P(p_1,p_2) = \int_{source} \mid \Psi(x_1,p_1,x_2,p_2) \mid^2 \rho(x_1)P(p_1)\rho(x_2)P(p_2)d^4x_1 d^4x_2 \tag{1.1}$$

where $\Psi(x_1,p_1,x_2,p_2)$ is the wave function of the two pions with momentum $p_1$ and $p_2$.

If one assumes for simplicity, that the interactions between the pions are weak, and one neglects the Coulomb final state interactions with the rest of the system, one can approximate the relative wave function by

$$\Psi(x_1,p_1,x_2,p_2) = \frac{1}{\sqrt{2}}[e^{ip_1x_1}e^{ip_2x_2} + e^{ip_1x_2}e^{ip_2x_1}] \tag{1.2}$$

A correlation function may be defined in terms of the two particle and single particle momentum distributions,

$$1 + R(p_1,p_2) = \frac{P(p_1,p_2)}{P(p_1)P(p_2)} \tag{1.3}$$

where $P(p_1,p_2)$ is the probability of detecting the two pions in coincidence, and $P(p_1)$ and $P(p_2)$ are the probabilities of detecting one pion in singles. After a few simple manipulations, we can get a formula for the correlation function,

$$R(q) = \mid F_{12}(q) \mid^2 \tag{1.4}$$

where $F_{12}(q)$ is the Fourier transformation of the source density distribution $\rho(x)$,

$$F_{12}(q) = \int e^{iqx}\rho(x)d^4x \tag{1.5}$$

and $q = p_1 - p_2$ is the relative momentum of the two pions.

From Equation 1.4 the correlation function is simply related to the Fourier transform of the source density. Clearly, it is sensitive to the space-time extent of the source for pion emission. One may use this property to measure the source size and lifetime of pion emission.

To give a concrete example, we further approximate the source space and time distributions by Gaussian distribution functions

$$\rho(x) = \rho(r,t) = \frac{1}{\pi^{3/2}r_0^3}\, e^{-r^2/r_0^2} \frac{1}{\pi^{1/2}\tau}\, e^{-t^2/\tau^2} \tag{1.6}$$

After performing the Fourier transformation, we obtain the correlation function,

$$1 + R(q,E) = 1 + exp(-\frac{1}{2}q^2r_0^2 - \frac{1}{2}E^2\tau^2) \tag{1.7}$$

where $r_0$ is the radius and $\tau$ is the lifetime of the emission source. Figure 1.2 shows a plot of the correlation function as a function of the two pion relative momentum for different values of the source radius parameter $r_0$. For simplicity, the lifetime $\tau$ is chosen to be zero. All correlation functions display maxima at q = 0 due to Bose statistics when the pions are in the same momentum state. It is important to note how the correlation function depends on the source size parameter $r_0$. For smaller source radii $r_0$, the peak in the correlation function extends to larger values of relative momenta q. Similarly, as the source lifetime is decreased for fixed source radius, the peak in the correlation function also extends to larger values of the relative energy E. In this fashion, measurement of the correlation function are sensitive to the size and the lifetime of the source which emits pions.

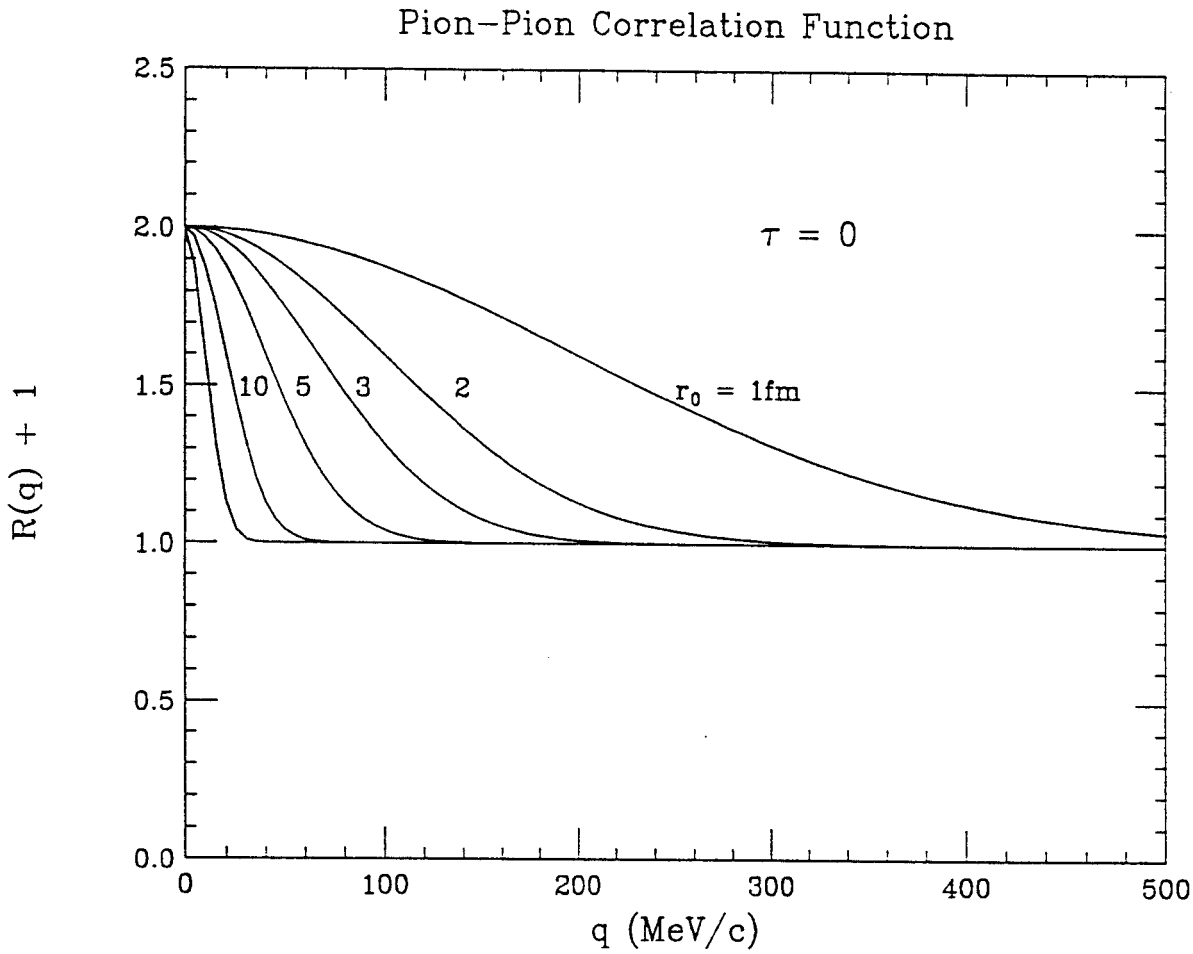


Figure 1.2: Theoretical calculation of pion - pion correlation functions, assuming a gaussian source distribution with lifetime $\tau = 0$.

In intermediate energy heavy ion interactions, the pion multiplicity is too small for practical pion-pion correlation function measurements. Comparable information can be obtained from proton-proton correlation measurements using a technique proposed by Koonin in 1977 [Koon 77]. Unlike pions, the interactions between the two protons are influenced by the strong nuclear interaction as well as the Coulomb interaction in addition to the identical particle effects, which govern the pion correlations. Unlike pions, the total wave function of the two protons will be antisymmetric with respect to the exchange of the two particles because protons are fermions. The space wave function for the two protons is spatially symmetric when the proton spins are in the antisymmetric spin singlet state and spatially antisymmetric when the protons are in the symmetric spin triplet state. If we assume the spin triplet and singlet state are populated randomly in phase space, then the spatial wave function can be written as,

$$\Psi_{12}(p_1, p_2) = \frac{1}{4} \mid \Psi_q^1(r) \mid^2 + \frac{3}{4} \mid \Psi_q^3(r) \mid^2 \tag{1.8}$$

where $\Psi_q^1(r)$ is the wave function corresponding to the spin singlet state $S_0^1$ (S=0), and $\Psi_q^3(r)$ is the wavefunction corresponding to the spin triplet state $S_1^3$ (S=1). Due to the strong nuclear interaction between the protons, the Schrodinger equation must be solved numerically to get the wave function. In order to extract the source size, a simple Gaussian source density distribution function is frequently be assumed for proton emission,

$$\rho(r,t) = \frac{1}{\pi^{3/2} r_0^3} e^{-(r-V_0 t)^2/r_0^2} \frac{1}{\pi^{1/2}\tau} e^{-t^2/\tau^2} \tag{1.9}$$

where $r_0$ represent the size of the emission source, and $\tau$ represent the lifetime of the source. If one assumes, for simplicity, a negligible nuclear reaction lifetime, one obtains in analogy of Equation 1.7,

$$1 + R(p_1, p_2) \;=\; \frac{1}{(2\pi)^{3/2}\, r_0^3} \int dr\; exp(-r^2/2r_0^2)$$

$$\{\frac{1}{4} \mid {}^1\Psi_q(r) \mid^2 + \frac{3}{4} \mid {}^3\Psi_q(r) \mid^2\} \tag{1.10}$$

Correlation functions have been calculated with Equation 1.10 using two proton wavefunction $\Psi_{12}(p_1, p_2)$, which was obtained by numerically solving the Schrodinger equation with the Reid soft core nuclear potential [Reid 68]. The resulting correlation function is shown in Figure 1.3. At $q \approx 0$, the long range repulsive Coulomb interaction between the two protons prohibit the two protons ever having exactly the same momentum, so $R(q) = -1$. The correlation functions shows a maxima at $q \approx 20$ MeV/c due to the attractive strong interaction between the two protons in the singlet state $S_0^1$. At larger relative momenta $q > 80$ MeV/c, the interactions between the two protons are much weaker and the correlation function vanishes.

The magnitude of the maximum at $q \approx 20$ depends on the spatial overlap of the two detected protons. Due to the short range of the nuclear force, the smaller the source size and the shorter its lifetime, the more likely the two protons will have strong final state interactions, correspondingly larger correlation functions. This is illustrated in Figure 1.3, for the limit of instantaneous emission. Clearly, the peak of the correlation function increases with decreasing $r_0$, the radius of the gaussian source for proton emission. Similarly, for fixed source radius, the peak of the correlation function will increase for decreasing source lifetime.

This property has been widely used to measure the source size and lifetime in the heavy ion induced reactions [Gelb 87, Boal 90a]. Generally, the measured correlation functions increase monotonically with the energy of the emitted protons [Lync 83, Chen 87a]. This can be explained by considering the time dependence of preequilibrium processes as schematically described in Figure 1.4. Generally speaking, when a light projectile impinges upon a heavy target, the highest energy particles are emitted during the earliest stage of the nuclear reaction, and the correlation func-

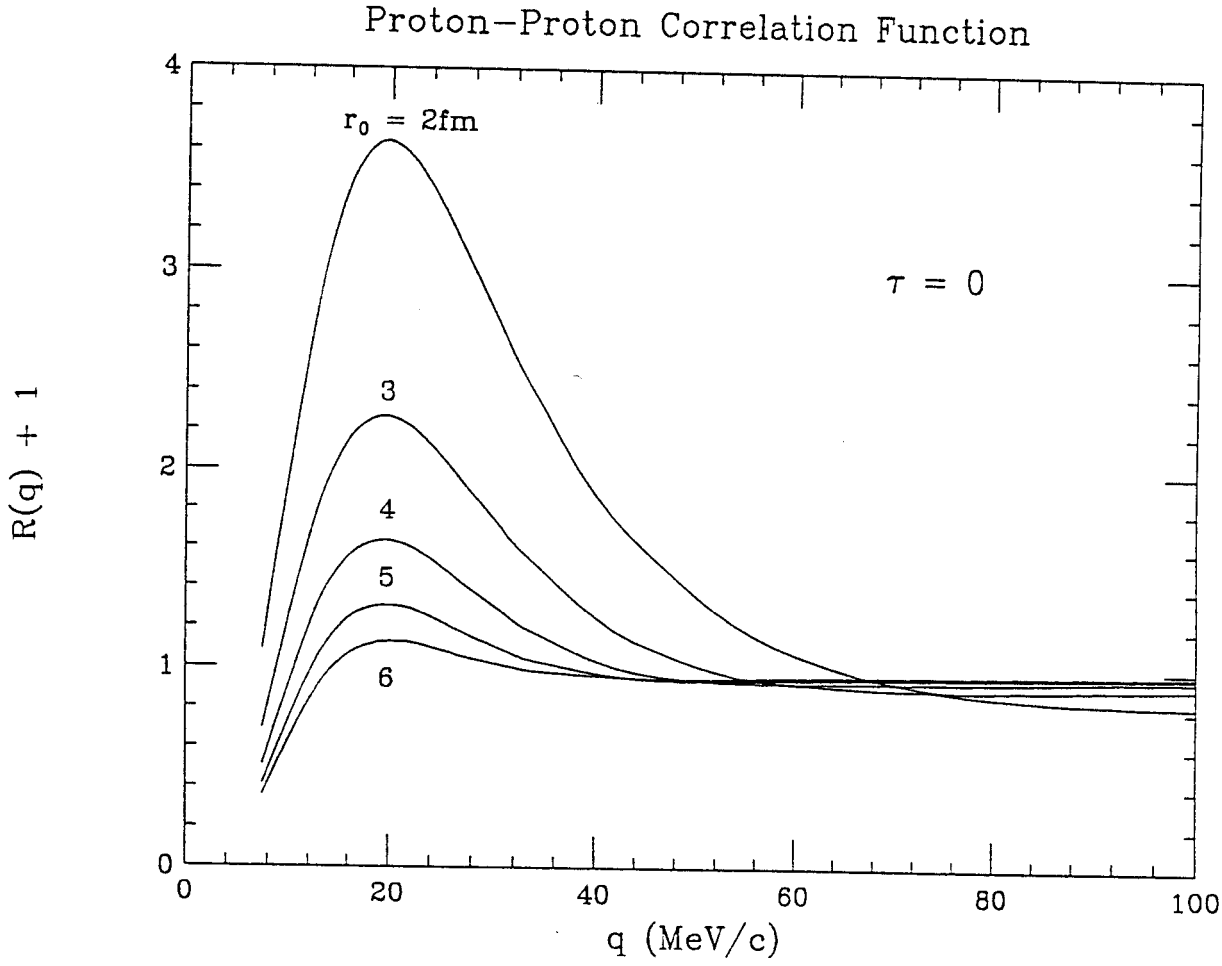


Figure 1.3: Theoretical calculations of proton-proton correlation functions assuming a gaussian source distribution with a negligible lifetime.

tion therefore reflects a small source size corresponding to the overlap of the projectile and the target at the time of initial contact. As the nuclear system evolves toward equilibrium, slower, ie, lower energy protons are emitted; the correlation functions for such lower energy protons will reflect the larger source size at this later stage of the nuclear reaction. Such energy dependence of correlation functions might be expected to be most dramatic for light ion induced reactions on heavy targets, due to the extreme difference between the small size of the initial configurations involving the projectile and a few target nucleus and the much larger size of the equilibrated target-like residue. A comparison of two-proton correlation functions for p+Ag and $^{14}$N + Ag reactions at 500 MeV, which included all protons above the detection thresholds, however, displayed practically no sensitivity to the size of the projectile [Cebr 89], casting doubt upon the connection between two particle correlation function and the size of the emitting source. In this thesis, measurements of two-proton correlations were performed for $^{3}$He induced reactions as functions of the energies of the detected protons. These measurements were compared to other measurements performed with heavier projectiles in an effort to resolve this controversy. This comparison suggests a natural scaling of the correlation functions for energetic protons with the projectile mass. The extracted source size scale with $A_{proj}^{1/3}$ [Zhu 91].

## 1.3 Temperature of nuclear excited system

In phase space models, particle production is largely determined by the internal energy per nucleon of the system, or equivalently by the nuclear temperature. While intensity interferometry provides information about the space time evolution of a nuclear reaction, information about the manner in which the system distributes its energy into internal and collective degrees of freedom requires additional observables. In intermediate energy collisions (MeV 10 $<$ E/A $<$ 100 MeV) the extraction of

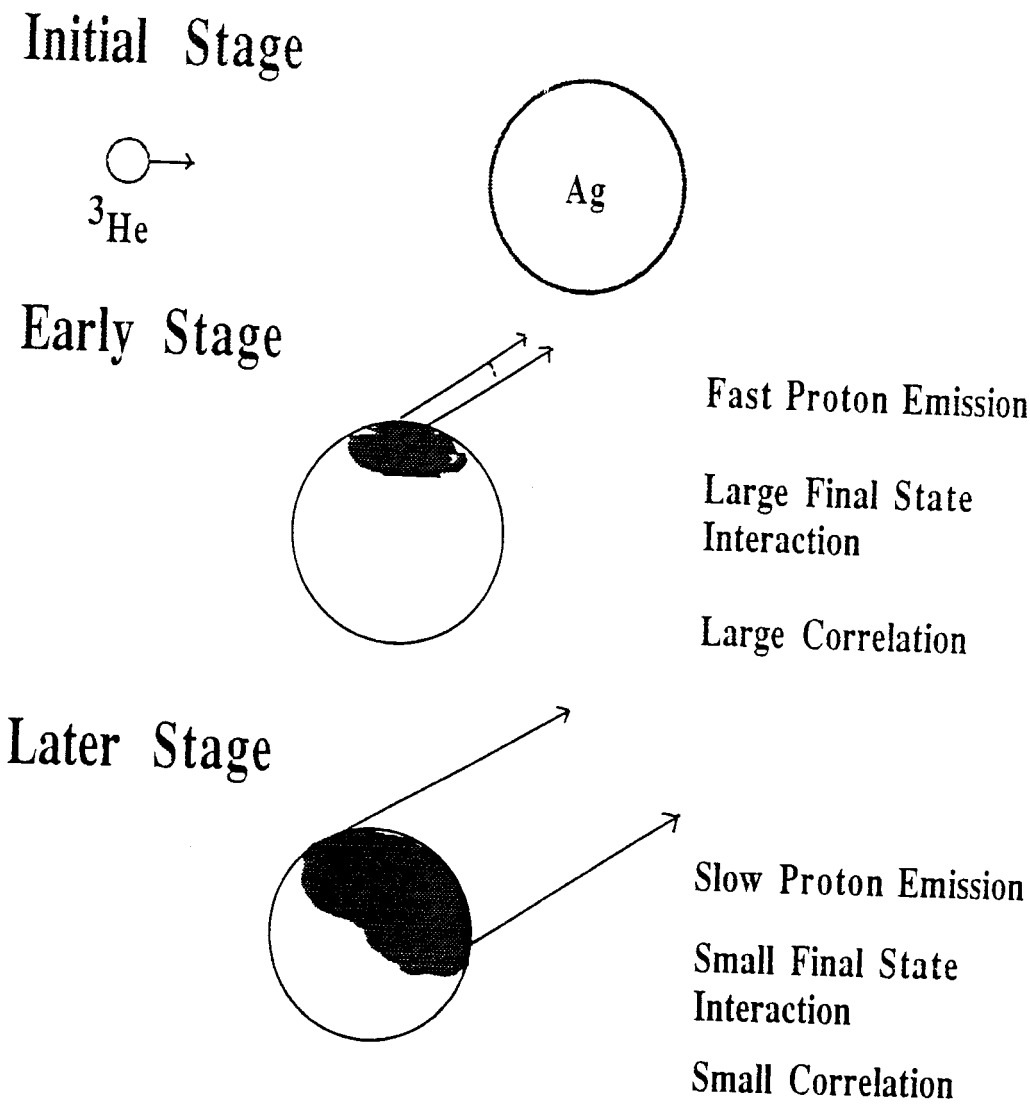


Figure 1.4: A schematic diagram showing the evolution of the nuclear reaction from initial contact to the final and more equilibrium stages.

information about the internal excitation of the system is complicated by the importance of pre-equilibrium emission mechanisms. Indeed, the time honored technique for deducing the nuclear temperature from kinetic energy spectra of emitted particles turned out to be more sensitive to collective motion than to internal excitation.

To better understand this point, let us consider how temperature has been previously measured in nuclear physics. Considerable effort has been expended in the investigation of the temperatures of compound nuclei formed in low energy nucleus reactions. In such collisions, the reaction can be separated into two steps, 1) the formation and 2) the decay of a compound nucleus as proposed by Bohr in 1936 [Bohr 36]. In such compound nuclei, all degrees of freedom are populated according to the available phase space. From detailed balance, one may show that the energy spectra of emitted particles are proportional to a Boltzman factor,

$$\frac{d^2\sigma}{dEd\Omega} \propto e^{-E/T} \tag{1.11}$$

where E is the kinetic energy, and T is the instantaneous emission temperature defined as

$$\frac{1}{T} = \frac{d[\ln \rho(E^*)]}{dE^*}. \tag{1.12}$$

Here $\rho(E^*)$ is the level density and $E^*$ is the excitation energy of the daughter nucleus after emission of the particle of interest [Weis 37]. By measuring the energy spectrum, the temperature of the emitting system can therefore be deduced.

In the relativistic ( E/A $>$ 0.5GeV/A ) nuclear interactions, the nuclear fireball model has been invoked to explain the exponential or *thermal* slopes of the proton energy spectra [West 76]. This model assumes a thermally equilibrated participant zone formed by the overlap of projectile and target nuclei. This region is assumed to contain most of the incident energy of the participant nucleons from the projectile

and target nuclei which lie in the overlap volume; the other nucleons form the spectator matter which remains relatively *cold.* The temperature of such fireballs can be deduced by generalizing the thermal properties of a compound nucleus and fitting the kinetic energy spectrum of participant nucleons by a Maxewellian distribution. Generally, *spectral* temperatures thereby deduced, increase with increasing beam energy. At recent AGS experiments at 14.5 GeV/A, similar analyse of the transverse energy spectra for different particles have yielded temperatures ranging from 126 MeV to 187 MeV [Abbo 90].

In both of these two extreme energy domains, the nuclear temperature plays an important role in describing the nuclear reaction.

At intermediate energies, similar analyse has been performed to deduce temperatures by fitting the energy spectra, with a non-relativistic Maxewellian distribution,

$$\begin{aligned} \frac{d^2\sigma}{dEd\Omega} &= C\sqrt{E - V_c}e^{-E_s/T} \\ E_s &= E - V_c + E_0 - 2\sqrt{E_0 - V_C}\cos\theta. \end{aligned} \tag{1.13}$$

Here $V_c$ is the kinetic energy gained by the Coulomb repulsion from the emitting source, T is the temperature of the emitting source, and $E_0 = \frac{1}{2}mv^2$, where m is the mass of the detected particle, v is the velocity of the source in the laboratory frame. $\theta$ is the angle of the emitted particle in the laboratory frame.

While the kinetic energy spectrum is easy to measure in an experiment, it can have many non-thermal contributions from collective motion which may sufficiently enhance the spectral temperature as to render it useless for determining the internal excitation of the reacting system. One must therefore investigate different observables in order to deduce the temperature. One such technique involves the measurements of the populations of excited states [Morr 84, Poch 85]. It relies on the fact that when thermal and chemical equilibrium is achieved in a nuclear reaction, the populations of

excited states of a fragment which is in equilibrium with the remaining large system will obey the Boltzman distribution,

$$\frac{n_1}{n_2} = e^{-(E_1-E_2)/T}. \tag{1.14}$$

Measurements of excited state populations were initially performed for particle stable excited states [Morr 84, Xu 86, Lee 90]. In this case, the excited state populations were deduced from measurements of $\gamma$ rays in coincidence with fragments detected in their ground states. For example, if a $^7Li^*$ nucleus in its 0.478 MeV excited state is emitted in the $^{14}$N + Ag reaction, the $\gamma$ ray decay of this excited nucleus may be deduced from the coincidence detection of a $^7Li$ in its ground state and a 0.478 MeV $\gamma$ ray. Singles measurements of this $^7Li$ yield provides information about the sum of the yield in the 0.478 MeV particle stable excited state and in the ground state. The ratio of the population of $^6Li$ nuclei in the 0.478 MeV excited state to the total particle stable yield can be deduced and used to extract the temperature of the emission system via Equation 1.14. The extracted temperatures from such lower lying particle stable excited states are extremely low ( T $\approx$ 1 MeV) [Morr 84]. This occurs because the sequential decay from high lying excited states of heavier nuclei preferentially feed the ground state populations and consequently alter the ratio of the excited state population to the ground state population. Nevertheless, information about the temperature of the system can be obtained if one measures a large number of particle stable excited states [Xu 86]. If such data are compared to calculations which account for the sequential decay, much larger temperatures of about 3 MeV have been obtained from the decay of particle stable excited states [Xu 86, Lee 90].

Above the particle decay threshold, high lying excited states will preferentially decay by particle emission. Here the intervals between energy levels can be rather large, and subsequently, the sensitivity of temperatures extracted from these lev-

els to sequential feeding is smaller [Poch 85]. A large number of experiments have been performed to extract the excited state populations of emitted particle unstable fragments. Shown in Figure 1.5 are the emission temperatures extracted from the populations of excited states as a function of incident energy for a variety of reactions. Three open squares and solid circles are from ref. [Chen 87b], they represent temperatures extracted for the $^{16}O$ + $^{197}Au$ reaction at E/A=94 MeV [Chen 87b], the $^{40}Ar$ + $^{197}Au$ reaction at E/A=60 MeV [Poch 87], and the $^{14}N$ + $^{197}Au$ reaction at E/A=35 MeV [Chit 86]. The solid square corresponds to the $^{14}N$ + Ag reaction at E/A=35 MeV [Naya 92]. The open diamond corresponds to the $^{40}Ar$ + $^{197}Au$ reaction at E/A=200 MeV [Kund 91]. The solid diamond corresponds to the $^{14}N$ + Ag reaction at E/A=35 MeV [Bloc 87]. These data points were extracted from the populations of particle unstable excited states. We also show the temperature extracted from particle stable excited states. The open circle corresponds to the $^{32}S$ + Ag reaction at E/A=22.3 MeV [Xu 89]. There appears to be a slight increase of the extracted temperatures with increasing incident beam energy. Considering the wide energy range from $E/A = 22.5 - 200$ MeV, nevertheless, the temperatures extracted from excited state populations do not increase very much and are far below the temperatures extracted from kinetic energy spectra with Equation 1.13. The solid and dashed lines correspond to BUU calculations for emission temperatures of an equilibrated target-like residue produced in $^{40}Ar$ + $^{124}Sn$ collisions at an impact parameter of $b = 0$, with stiff (dashed line) and soft (solid lines) equation of state (EOS) [Xu 92]. The BUU calculations qualitatively reproduce the measured emission temperatures. Calculations assuming a stiff EOS yield larger temperatures than calculations assuming a soft EOS.

Measurements of excited state population can also be used to test if the thermal equilibrium is reached in a heavy ion reaction. For example, in thermal particle

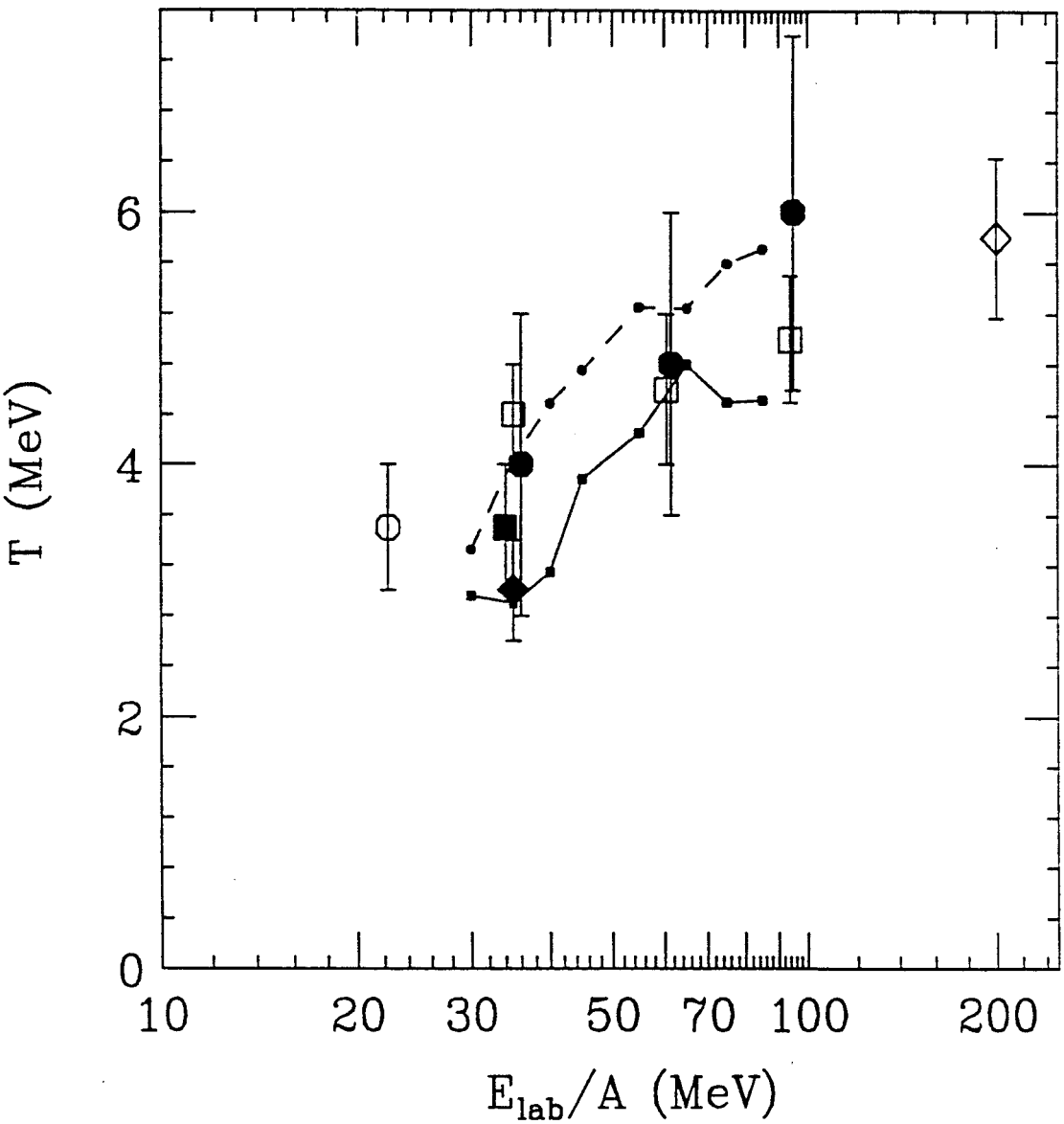


Figure 1.5: Systematic measurement of emission temperature from excited state populations as a function of incident beam energy. The lines are BUU calculations and the points are experimental measurements.

production models, populations of more than two excited states of a given nucleus must all be consistent with a single temperature. Such a test has been performed for the $^{14}$N + Ag reaction at E/A =35 MeV [Naya 89, Naya 92]. The measured population probabilities of excited states in $^{10}B$ nuclei are shown as solid points in Figure 1.6, as a function of the excitation energy. The third group of excited states at $E^* \approx 6$ MeV does not follow the exponential decrease of the population probabilities, a trend expected from the Boltzman factor. Even sequential feeding calculations, shown as shaded rectangles in the figure, performed for an initial temperature of $T = 4$ MeV, do not exhibit a population inversion and therefore can not explain the big discrepancy displayed for the third excited state. Non-statistical populations were also observed for other fragments emitted in this reaction. These non-statistical populations suggest that the system has not yet reached equilibrium.

This previous measurement, however, was performed without an impact parameter selection. The observed non-statistical populations might be another manifestation of non-equilibrium excitation energy distributions observed previously for peripheral collisions [Awes 84, Vand 84]. More exclusive measurements are clearly needed to address this question.

For the $^{36}Ar + ^{197}Au$ reaction at E/A =35 MeV, we measured excited state populations with the high resolution hodoscope and used the charged particle multiplicity in the MSU Miniball $4\pi$ multifragment detection array as an indicator of the centrality of the nuclear reaction [Kim 89]. With this array, it was possible to distinguish peripheral collisions at large impact parameters which lead to the production of only a small multiplicity of charged particles, from central collisions at small impact parameters which produce a large multiplicity of charged particles.

The thesis is organized as follows. Details of the experimental apparatus are given in chapter 2. Detailed data analysis procedures, including calculations of the

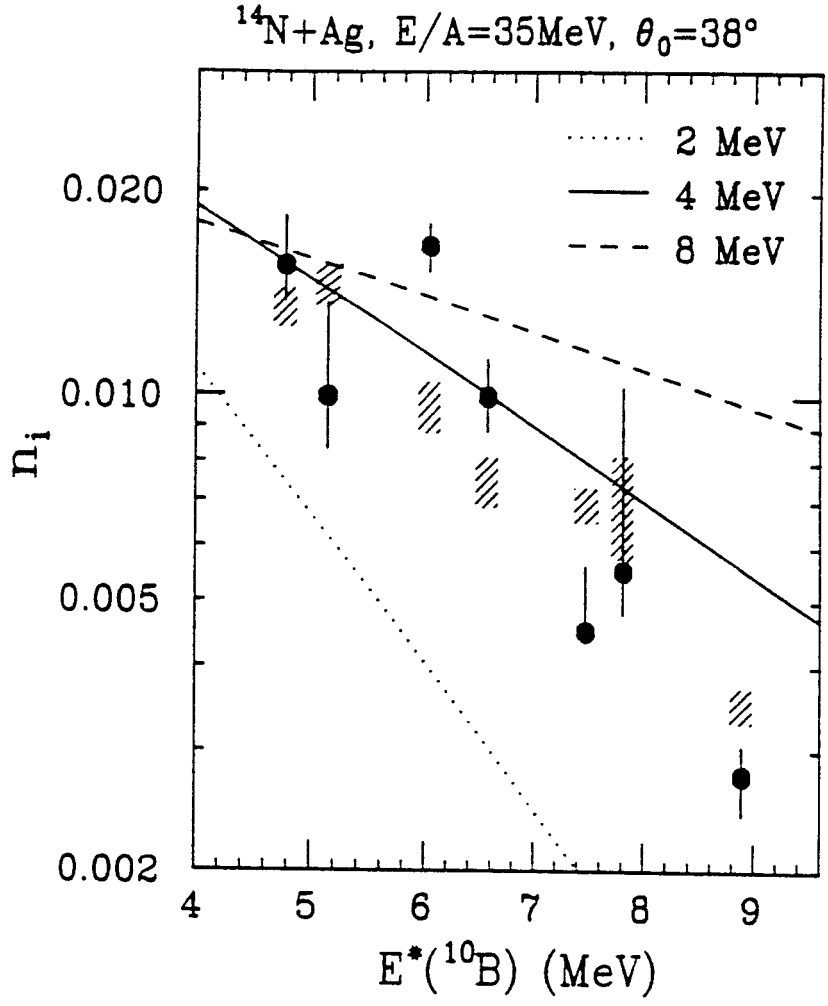


Figure 1.6: The population probability of $^{10}$B excited states for the $^{14}$N + Ag reaction at E/A =35 MeV [Naya 89].

hodoscope response function and corrections for sequential feeding, are discussed in chapter 3. Investigations of the $^{3}He + Ag$ reaction at $E_{beam} = 200$ MeV are discussed in chapter 4. Investigations of the $^{36}Ar + ^{197}Au$ reaction at E/A = 35 MeV are discussed in chapter 5. A summary is given in chapter 6.

# Chapter 2

# Experimental Details

This thesis consist of the results of two distinct experiments. Two major apparatus have been used to perform these experiments, 1) a 13 element high resolution hodoscope and 2) the MSU $4\pi$ Miniball array. For measurements of the $^{3}$He + Ag reaction at $E_{beam}$ = 200 MeV, the hodoscope alone was used to measure the particle coincidence events. For the $^{36}$Ar + $^{197}$Au reaction at E/A = 35 MeV, the hodoscope was modified to fit into the MSU $4\pi$ Miniball array. In this latter experiment, the decays of particle unstable fragments were gated by the impact parameter filter deduced from the charged particle multiplicity measured by the MSU $4\pi$ Miniball array. These two devices are described in more detail in this chapter.

## 2.1 The 13 elements high resolution hodoscope and $^{3}$He + Ag reaction at $E_{beam}$ = 200 MeV

A hodoscope has been developed to measure the decays of particle unstable intermediate mass fragments [Mura 89]. Since the cross section and the energy separation of the relevant excited states of these fragments are often small, this array must have both high efficiency and high excitation energy resolution. In order to achieve a high efficiency for detecting the coincidence particles, a big solid angle coverage is essential.

So the hodoscope is located very close to the target. In order to have a good excitation energy resolution, both good energy resolution and good angular resolution of the two individually detected decay particles which are emitted by the particle unstable fragment are essential. $\Delta E - E$ telescopes consisting of silicon detectors and NaI(Tl) scintillators provide the necessary energy resolution and particle identification. Two orthogonal single wire gas counters are placed in front of each telescope to give an x-y position readout. The resulting hodoscope therefore provides good resolution for both energy and position measurements.

### 2.1.1 general description of the hodoscope

The front view of the 13 element hodoscope is shown in figure 2.1. It consists of 9 light particle telescopes and 4 heavy fragment telescopes. Each light particle telescope consists of a 200 $\mu$m non-planer surface barrier silicon detector of 450 mm$^2$ surface area, a 5mm lithium drifted silicon detectors (Si(Li)) of 500 mm$^2$ surface area and followed by a 10cm thick NaI(Tl) stopping detector. The 5 mm Si(Li) detectors were fabricated with a total dead layer less than 15 $\mu$m. This dead layer occurs at the back surface of the detector which faces the NaI(Tl) detector. The light particle telescopes are optimized to detect light particles of Z $\leq$ 2 and can stop protons of 200 MeV energy. The heavy fragment telescopes were originally designed to detect charged particles with Z $\geq$ 3. Each telescope consists of 75 $\mu$m and 100 $\mu$m of surface barrier silicon detectors of 300 mm$^2$ surface area, and a 5 mm Si(Li) detector of 400 mm$^2$ surface area. In our measurement of $^3$He + Ag reactions at 200 MeV beam energy, light ions of $Z \leq 3$ fragments were the main focus of the measurement, however. To increase the energy dynamic range of the heavy fragment telescopes, an additional 5 mm Si detector was added to the back of each heavy fragment telescope. The position information for each individual telescope is obtained with two single wire

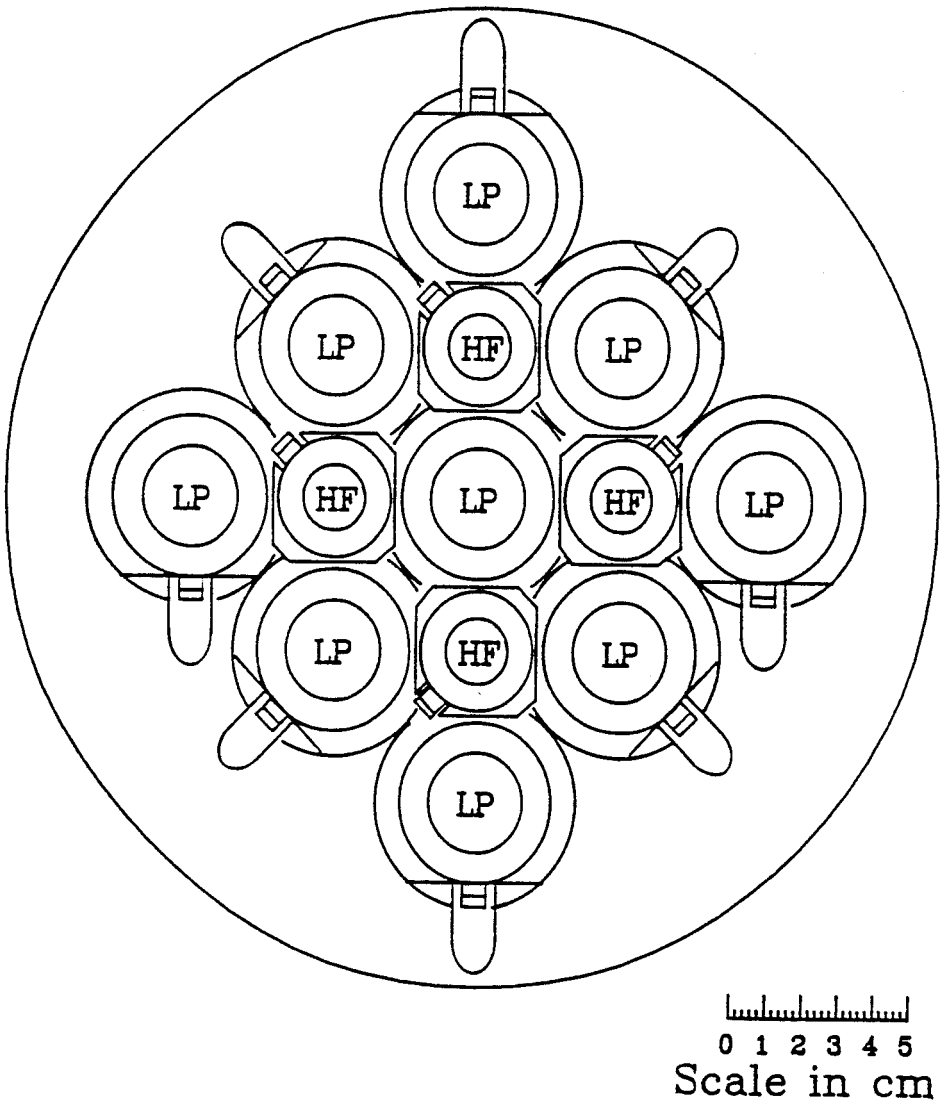


Figure 2.1: Schematic diagram of front view of the high resolution hodoscope, it consists of 9 light particle telescopes (LP) and 4 heavy fragment telescopes (HF).

gas proportional counters, each providing one coordinate of the x - y read out. These gas counters are placed at the front of each telescope. The front and rear windows of the gas counters are 6 $\mu$m Mylar ($(C_{10}H_8O_4)_n$) aluminized on the interior side to provide a cathode surface. A 1.5 $\mu$m Mylar foil, aluminized on both sides, separates the x and y position counters. Anode wires made of 7.6 $\mu$m wire, bisect each of the x (or y) counters. These wires are insulated from the body of the proportional counters by a G-10 feedthrough.

The efficiency and long term stability of the gas counters were tested with a variety of gas mixtures. A mixture of 80% Isobutane ($(CH_3)_2CHCH_3$) and 20% methylal ($CH_2(OCH_3)_2$) was chosen to reduce the possibility of aging effects caused by polymerization on the cathode and anode surfaces [Naya 92]. The gas counters operate at gas pressures ranging from 50-100 torr and voltages ranging from 900-1250V. A typical setting was 80 torr and 1200V. The 4 heavy fragment detectors were grouped together and controlled with one gas handling system, the 9 light particle detectors were grouped together and controlled by another gas handling system. A constant gas flow rate is maintained for all telescopes such that 20% of the counter gas was replaced every minute.

### 2.1.2 Energy calibration

The energy calibrations were performed separately for the Silicon detectors and the NaI(Tl) detectors. The linear response of the silicon detectors to the energy deposition by the ions makes its energy calibration quite straight forward. An energy deposition of 3.61 eV will produce an electron hole pair in a silicon detector [Goul 82]. A precision capacitor of 4.432 pf can be used to inject charge into the preamplifier input, which insures that a 10 V voltage tail pulse will inject a charge equivalent to 100 MeV energy deposition in the silicon detector. Different energy depositions in the silicon detector

can then be simulated by different voltages on the pulser. A precision calibration of the overall normalization of the pulser system was done by comparing to signals from an $^{241}$Am alpha source. The extension of this calibration to higher energies was done by using the precision potentiometer of the pulser at different potentiometer settings. Gain shifts of the electronics during the experiment were monitored by pulsers applied to the test inputs of the preamplifiers. An $^{241}$Am alpha source was used before and after the experiment to further monitor the gain shift of the silicon detector.

Because of the nonlinear response of NaI(Tl) detectors to energy and because the detectors responded differently to different particle types, very detailed energy calibrations have to be done for each particle type. Recoil protons, produced by the bombardment of a polypropylene($CH_2$) target by 200 MeV $^3He$ ions, was used to calibrate the NaI(Tl) detectors. Additional energy calibration points were obtained by cross calibrating against the energy loss in a 5 mm silicon detector. The gain shift of the NaI(Tl) detector was stabilized by monitoring gain shifts using the particle identification lines in the $\Delta E - E$ spectrum, shown in Figure 2.2.

### 2.1.3 Gas detector position calibration

When a charged particle passes through the gas detector, it ionize the gas inside the gas counter. The ionized electrons drift and diffuse along the electric field lines to the anode wire, where they are multiplied. Since the electric fields are roughly perpendicular to the wire, the charge density along the wire (x direction ) is a direct reflection of the x coordinate of the fragment's trajectory through the gas counter. Charge sensitive preamplifiers are connected to both ends of anode wire to amplify the charge which flows from the electron distribution on the wire to the respective preamplifier input. This charge deposited on each preamplifier is inversely proportional to the resistance of the wire plus preamplifier that the charge must traverse to

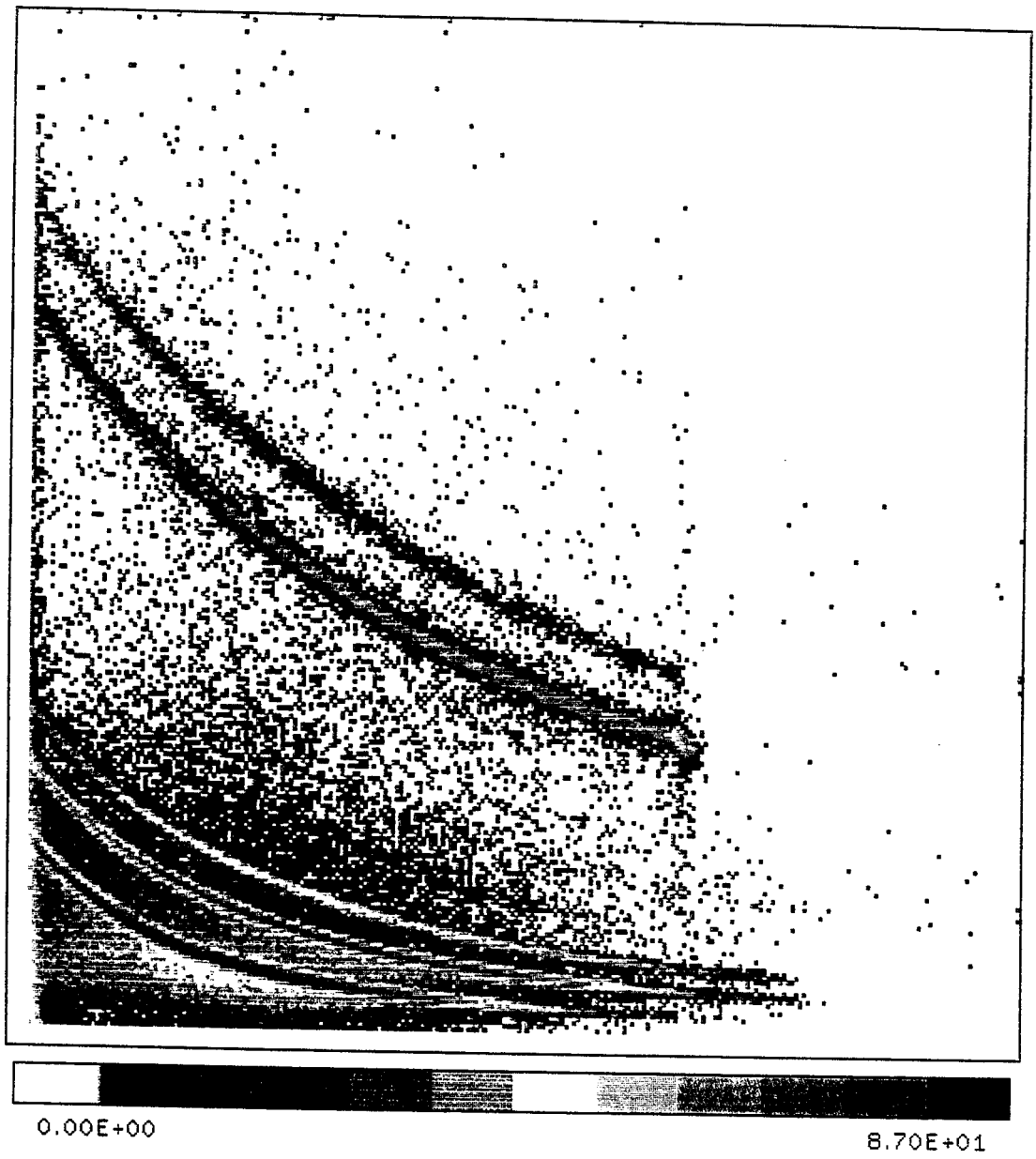


Figure 2.2: The two dimensional ΔE-E plot for the energy deposited in the 5 mm silicon detector (vertical) vs energy left in the NaI(Tl) detector (horizontal) obtained for the $^3$He + Ag reaction at $E_{beam}$ = 200 MeV.

reach a virtual ground at the base of the amplifying transistor in the preamplifier. Since the preamplifiers have a low input impedance, the dominant contribution to this resistance comes from the resistance of the wire between the point where the charge is deposited on the wire and the preamplifier. Therefore, to a good approximation, the position along the wire coordinate is given by,

$$x = \frac{L}{L+R} \tag{2.1}$$

where L (left) and R (right) are the voltages recorded by the ADC's for the signals from the respective ends of the anode wire. A position calibration is done by putting a mask in front of the hodoscope. This mask has holes of 1 mm diameter which are separated by 1.5 mm. The mask is placed at 16.5cm from the target. A $^{244}$Cm point alpha source is positioned at the target location to illuminate the calibration mask and ionize the gas counter. Non-linear fits to the calibration spectra are used to correct for non-cartesian effects in the simple charge division read out obtained using Equation 2.1:

$$\begin{aligned} X &= a_0 + a_1 X_m + a_2 Y_m + a_3 X_m^2 + a_4 X_m Y_m + a_5 Y_m^2 \\ &\quad + a_6 X_m^3 + a_7 X_m^2 Y_m + a_8 X_m Y_m^2 + a_9 Y_m^3 \end{aligned}$$

and

$$\begin{aligned} Y &= b_0 + b_1 X_m + b_2 Y_m + b_3 X_m^2 + b_4 X_m Y_m + b_5 Y_m^2 \\ &\quad + b_6 X_m^3 + b_7 X_m^2 Y_m + b_8 X_m Y_m^2 + b_9 Y_m^3 \end{aligned} \tag{2.2}$$

Here $X_m$ and $Y_m$ are the positions directly obtained by the charge division method from Eq. 2.1. The $a_i$ and $b_i$ coefficients were obtained by fitting the measured mask spectrum. The mask image of one detector is shown in figure 2.3. The widths correspond to 1 mm holes in the calibration mask, which are separated by about 1.5 mm.

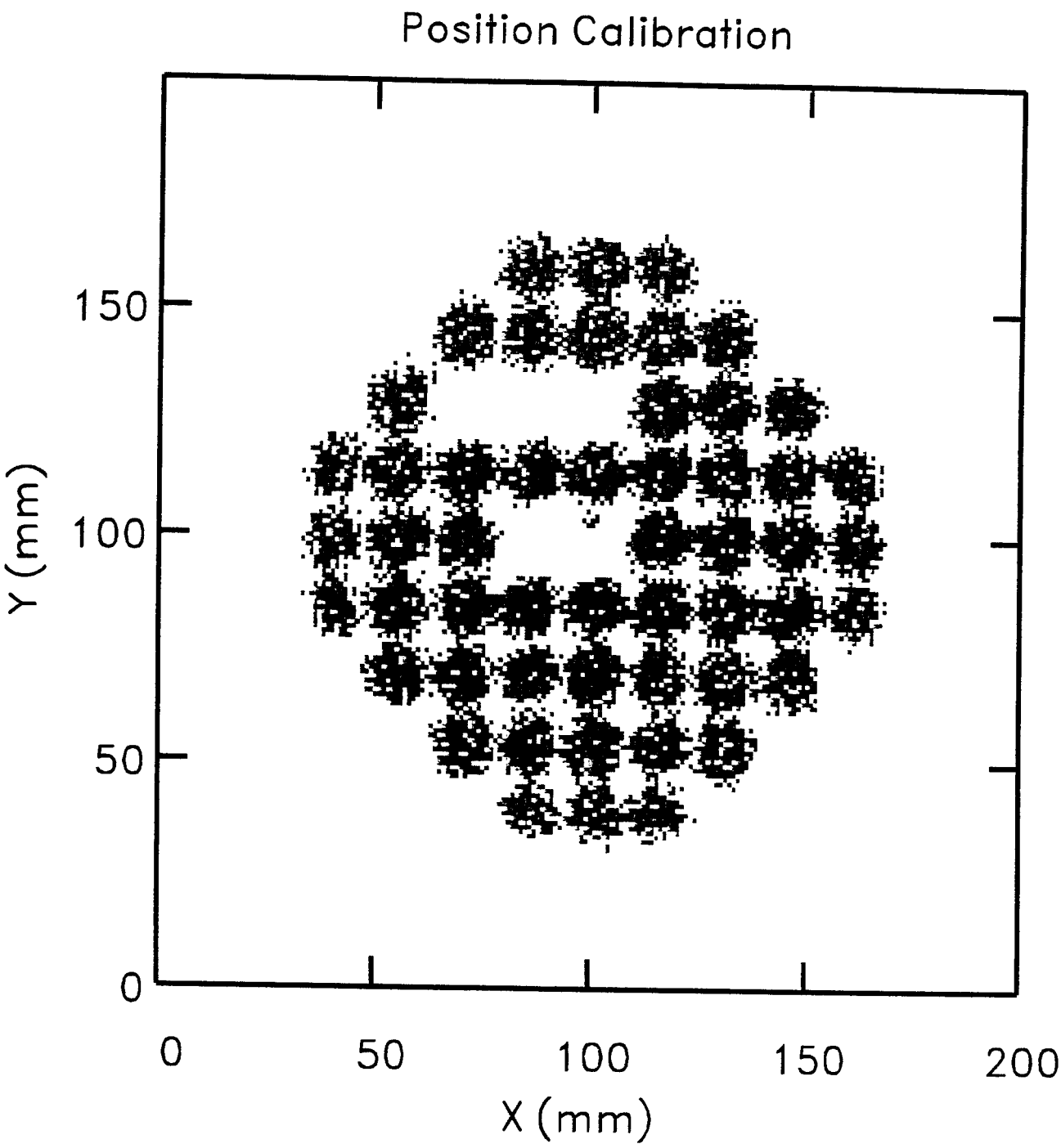


Figure 2.3: Two dimensional plot of position calibration mask image for $^3$He + Ag reaction at $E_{beam}$ = 200 MeV.

### 2.1.4 Particle identification

The particle identification method comes from the fact that energy loss in a detector depends on particle types. The energy loss of an ion passing through a medium is described by the well known Bethe-Bloch formula,

$$-\frac{dE}{dx} = 4\pi n \cdot \frac{e^4}{m} \cdot \frac{q_{eff}^2}{v^2} \cdot ln[\frac{2mv^2}{I(1-\beta^2} - \beta^2 - S - D] \tag{2.3}$$

where n is the number density of electrons in the medium; e and m are the charge and mass of the electrons respectively; $q_{eff}$ is the effective charge of the ion; v is the velocity of the ion; $\beta = v/c$; I is the ionization potential of the medium; S corrects for the electron shell effect; and D is a density correction factor.

For non-relativistic particles, $v^2 = 2E/M$, and one can neglect the shell and density corrections. Since the logarithm varies slowly with energy, equation 2.3 can be simplified as

$$\frac{dE}{dx} \propto \frac{Mq_{eff}^2}{E} \tag{2.4}$$

This formula simply says that energy loss in a thin $\Delta$E detector depends on its particle type ($Mq_{eff}^2$) and is inversely proportional to its energy E. For our particle identification, we use an empirical formula [Goul 75] for the stopping range of a particle in the detector material,

$$R \propto E^b/Mq_{eff}^2 \tag{2.5}$$

where E, R, M and $q_{eff}$ denote the energy, range, mass and effective charge of the detected fragment, respectively. Consider a particle which penetrats through the first silicon detector of a telescope which has a thickness T. This particle deposits $\Delta$E

energy in the first silicon detector and stops in the next detector where it deposits energy E. From Eq. 2.5, we obtain

$$Mq_{eff}^2 \propto ((E+\Delta E)^b - E^b)/T \tag{2.6}$$

To further make our particle identification independent of its energy, we adopt an empirical particle identification (PID) formula, defined as the following [Shim 79],

$$\begin{aligned} PID &= \ln(Mq_{eff}^2) \\ &= \ln(b\Delta E) + (b-1)\ln(E+c\Delta E) - b\ln(300) \\ b &= 1.825 - 0.18\frac{\Delta E[MeV]}{T[\mu m]} \\ c &= 0.5 \end{aligned} \tag{2.7}$$

Most of the time, we used planar ΔE detectors. As an example, the obtained particle identification function is shown in figure 2.4 for the $^{36}$Ar + $^{197}$Au reaction. The horizontal axis represents the particle identification and the vertical axis represents the particle energy. For the whole energy range, we get a straight line for a particle. Because of economical reasons, we used non-planar 200 $\mu m$ silicon ΔE detector for the $^3$He + Ag reaction. The thickness of the detector is therefore non-uniform. Since the PID function depends on the thickness of the ΔE detector, I have to compensate for this effect. The position information becomes very important here. The thickness is assumed to be dependent upon the distance to the center of the detector,

$$\begin{aligned} T(\rho) &= T_0 \cdot f(\rho) \\ f(\rho) &= exp(-\lambda\rho^2) \end{aligned} \tag{2.8}$$

where $\rho = \sqrt{x^2+y^2}$ is the distance from the center of the detector. The actual PID function is thus modified to compensate for the effects of non uniformity,

$$PID = PID + \lambda * \rho^2 \tag{2.9}$$

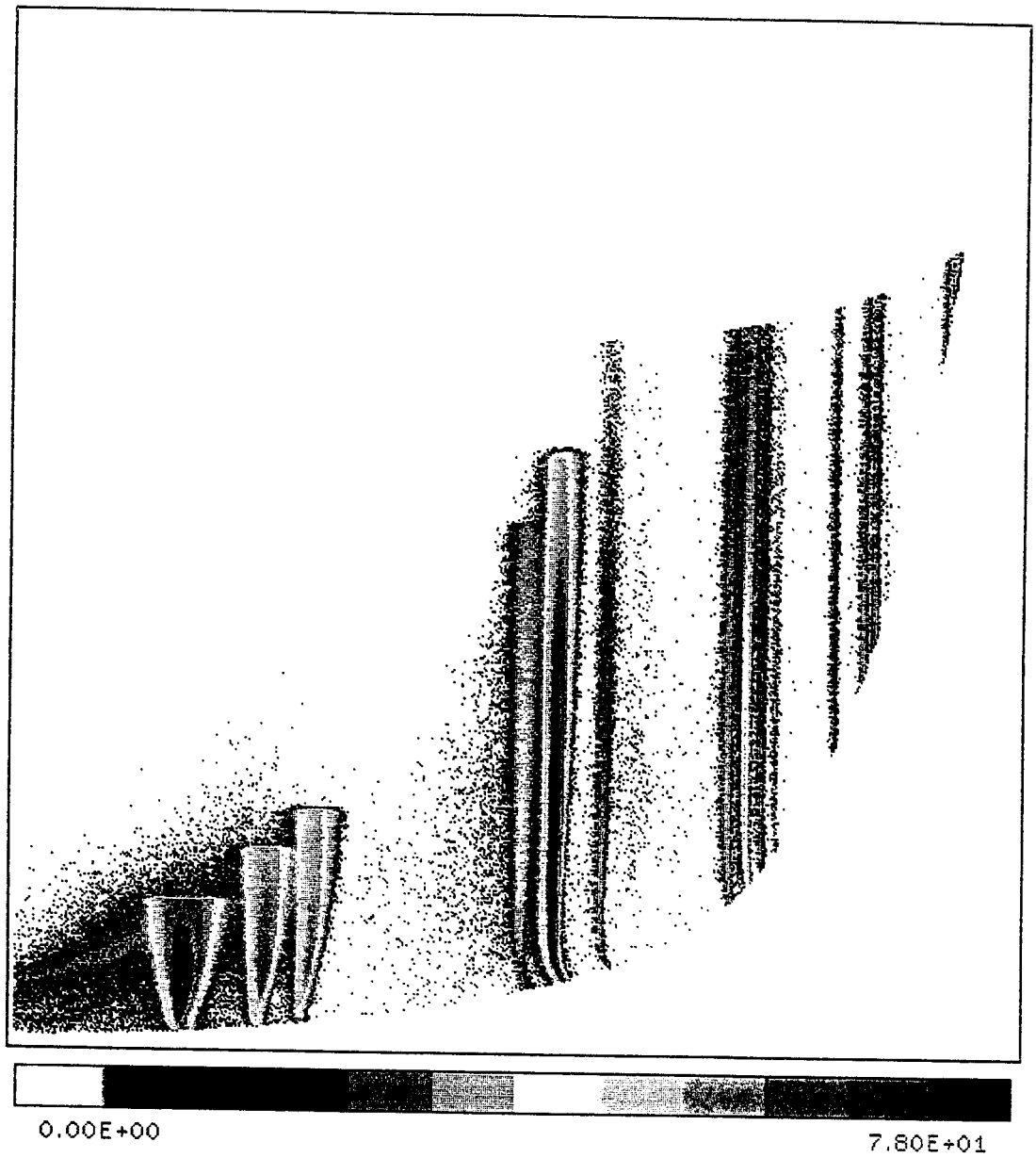


Figure 2.4: The two dimensional PID - E plot of particle identification function for $^{36}Ar + ^{197}Au$ reaction.

where $\lambda$ is the free parameter to adjust the PID dependence on the ionization position on the detector. The obtained particle identification function is shown in figure 2.5 for $^3$He + Ag reaction for p, d, t, $^3$He and $^4$He particles. We can clearly separate the particles very well.

### 2.1.5 Electronics setup for the Hodoscope

The electronics diagram for the hodoscope is shown in figure 2.6. On the top of the figure, the signals from the first and third elements of each hodoscope are sent to charge sensitive preamplifiers, followed by shaping amplifiers. The slow output of each amplifier is a gaussian signal with amplitude proportional to total collected charge. This signal is then sent to a Amplitude to Digital Converter (ADC) for digitization and is subsequently read by the computer. The linear signals from all silicon detectors, gas counters, and NaI(Tl) detectors are digitized the same way.

The second element of each telescopes was used to generate the trigger for each telescope. The fast output from the shaping amplifier of this detector was sent to a Constant Fraction Discriminator (CFD). The logic signal from this discriminator was sent to a 32 channel majority logic box along with the logic signals from the other 12 telescopes. The coincidence box generated an output to the pre-master box whenever 2 telescopes fired in coincidence. The logic signal from each telescope was also sent to a Down Scale (DS) module, which passed 5% signals on to a fan in/out module along with the other 12 telescopes to generate a singles event trigger, which went into the pre-master. Thus, singles and coincidence hodoscope events were taken simultaneously. When the computer is reading ADC's, it will send a busy signal to the master trigger box to veto all the events while it is busy. The master trigger generates start signals for the Time to Digital Converters (TDC), gate signals for the ADCs and gate signals for the bit registers.

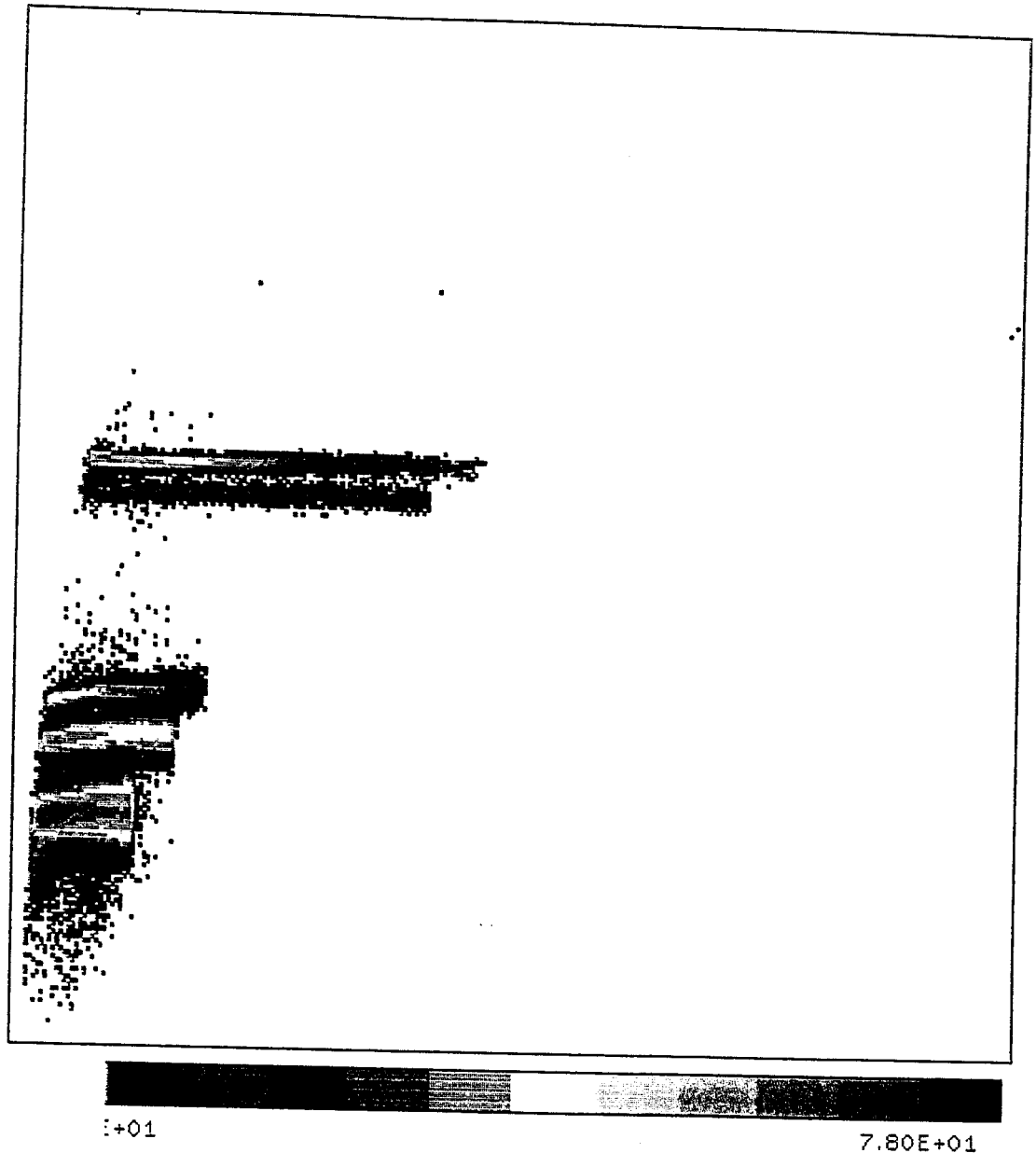


Figure 2.5: The two dimensional PID - E plot of particle identification function for $^3$He + Ag reaction.

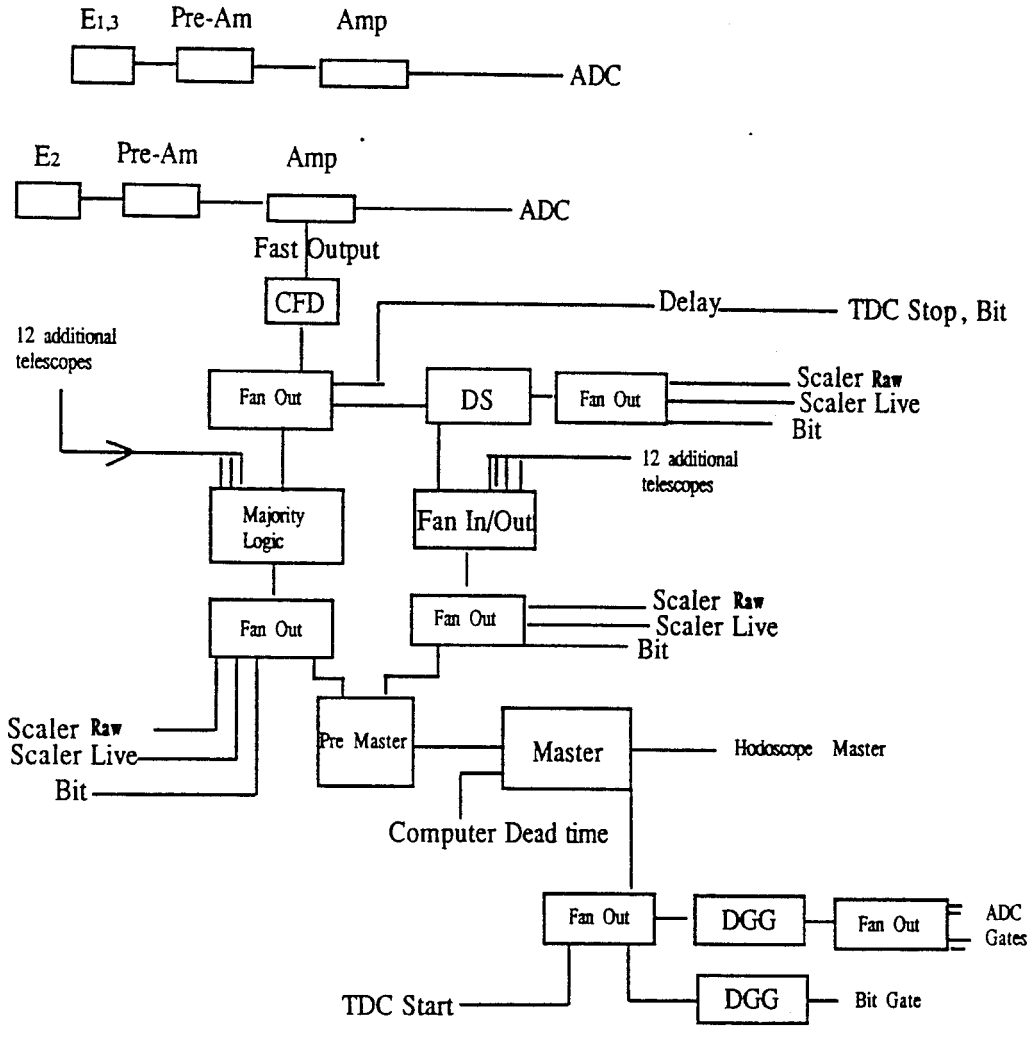


Figure 2.6: The hodoscope electronics diagram.

## 2.2 MSU $4\pi$ Miniball array and $^{36}Ar + ^{197}Au$ reaction at E/A = 35 MeV, in coincidence with hodoscope.

The MSU $4\pi$ Miniball array was used in the $^{36}Ar + ^{197}Au$ experiment to provide an impact parameter filter for particle unstable decay fragments detected in the hodoscope. In this experiment, we used rings 2-11 of the array which covered an angular range of $16^0$ - $160^0$ in the laboratory. In order to fit the hodoscope into the Miniball array, the nine NaI(Tl) detectors from the hodoscope were replaced by 400 $\mu$m silicon veto detectors, and excess material at the front end of the hodoscope was removed to make it smaller. In addition, 27 phoswich detectors out of the 176 detectors in rings 2 - 11 of the original array were removed to allow the insertion of the hodoscope. The remaining Miniball array covered a solid angle of 77% of $4\pi$.

The electronics diagram for Miniball, shown in Figure 2.7, is taken from [Kim 92a]. Each phoswich detector of the $4\pi$ Miniball array consists of a 40 $\mu$m thin fast plastic foil and a 2 cm CsI crystal which provides charged particle detection with a low threshold. A Photo Multiplier Tube (PMT) located at the back of the detector collects the total scintillation light produced by both the fast plastic and CsI crystals. Particle identification is achieved by integrating the PMT signal over several distinct timing gates. To achieve this, the anode current from the PMT is split into four signals. One is used as a trigger, and the other three are digitized by three Fast Encoding Readout Analog to digital converters (FERA) where the signals are integrated over three distinct timing intervals. A fast integration over the first 35 ns of the PMT signal selects light from the plastic scintillator signal (we call this the Fast signal). Two distinct timing gates are set for the CsI(Tl) signals. One integrates over $150ns \leq t \leq 550ns$ (we call this the Slow signal), and the other integrates over $1.5\mu s \leq t \leq 3.0\mu s$

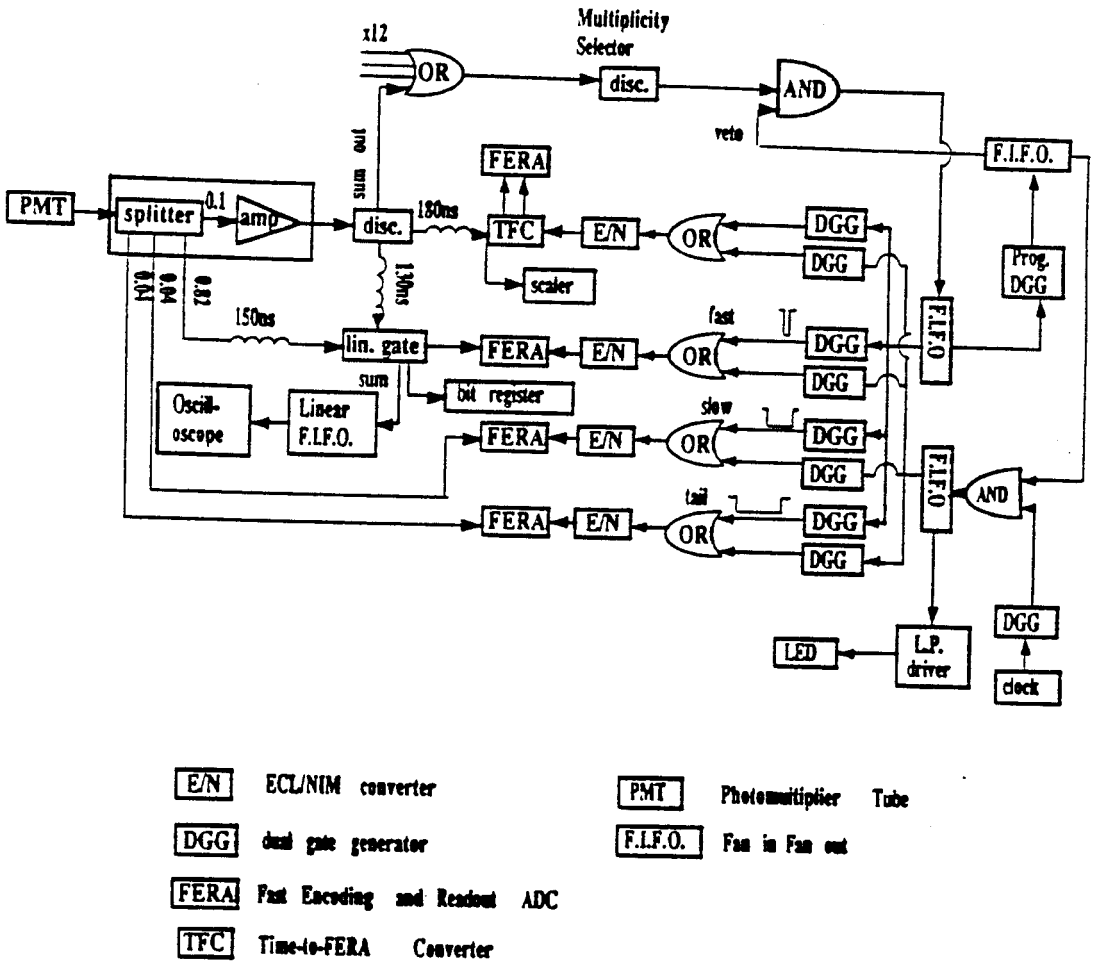


Figure 2.7: The Miniball electronics diagram.

(we call this the Tail signal). To improve the particle identification, a linear gate is used for the Fast signal so we can set an integration timing gate individually for each detector. A typical plot of the Fast vs. Slow signals, shown in Figure 2.8, indicates the elemental resolution which was achieved for the Miniball elements during this experiment. Since the primary function of the Miniball in this experiment was to provide an impact parameter filter based on charged particle multiplicity, individual charges in the Miniball detector were not individually analyzed. The slow moving heavy particles stopped in the fast plastic which did not have a slow signal were also not analyzed. Including the energy loss in the $5mg/cm^2$ Pb-Sn absorber foil, placed at the front of each phoswich detector, the threshold for particle identification in the Miniball is about $E/A \approx 2$, 3, 4 MeV for $Z = 3$, 10, and 18 fragments. More details about the Miniball $4\pi$ array are given in ref. [Souz 90, Kim 92a].

A schematic diagram is shown in Figure 2.9 for the trigger circuit of this coincidence experiment which requires the coincidence of the pre-master triggers of hodoscope and the Miniball array. The main concern of the coincidence electronics set up is to clear the random events of the Miniball array when there is no hodoscope event (or no master event). Since the tail signal takes about 3.5 $\mu s$ to digitize, a Miniball premaster will generate a signal of about $4\mu s$ to veto all the incoming events during this time. If a coincidence event happens, a longer computer dead time due to data taking will also veto the incoming events. If there is no coincidence master event, we want to abort the digitization process of the FERAs to reduce the computer dead time. A fast clear will be generated to clear the FERA modules unless it is vetoed by the master signal.

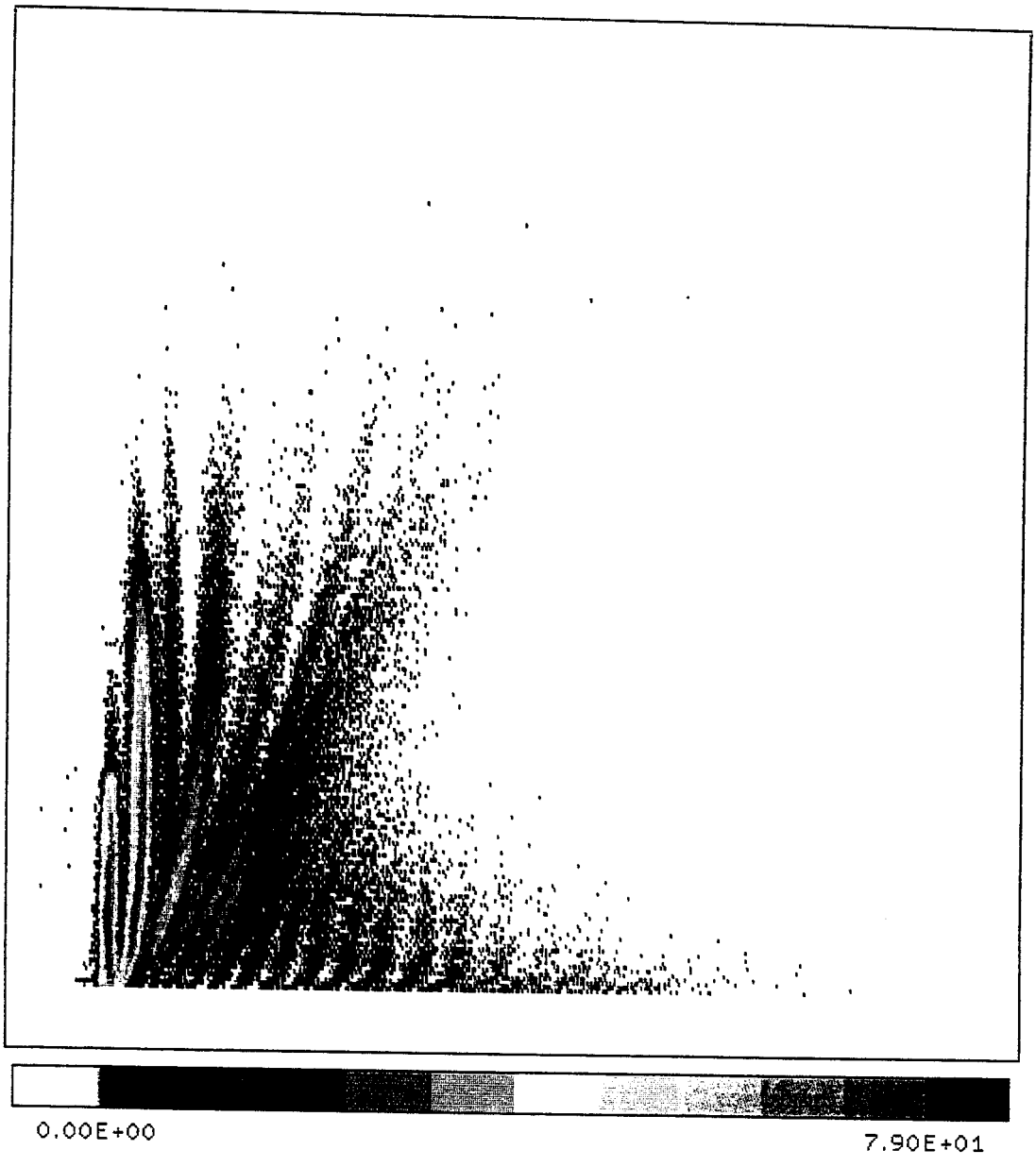


Figure 2.8: The diagram of a Miniball phoswich detector Fast vs Slow plot in the reaction of $^{36}Ar + ^{197}Au$ at E/A = 35 MeV.

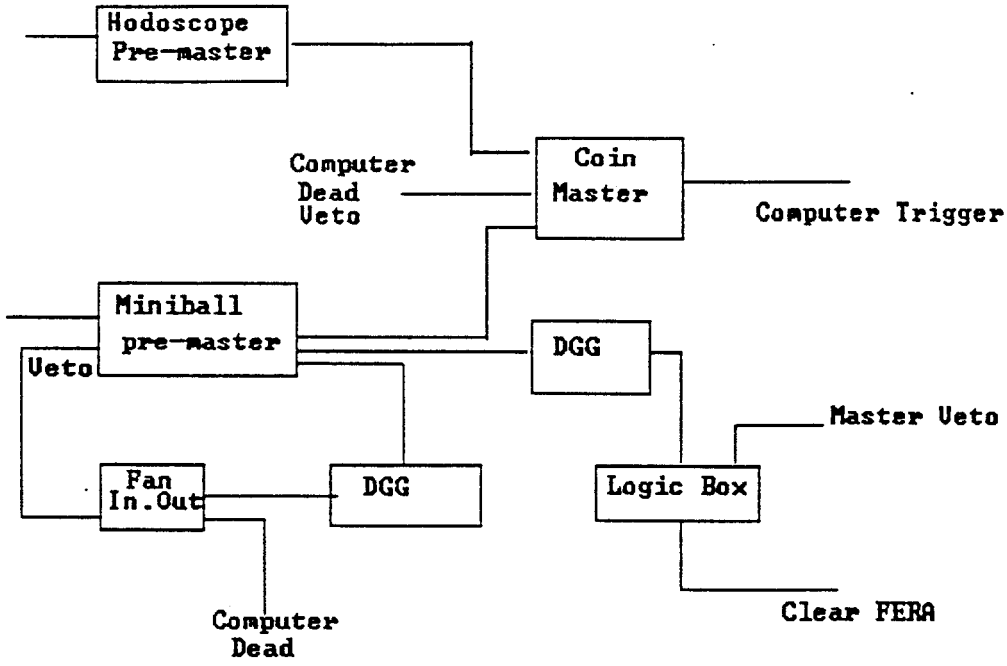


Figure 2.9: The Hodoscope-Miniball coincidence electronics diagram.

# Chapter 3

# Correlation function and excited state population analysis

As mentioned in chapter 1, we use two distinct techniques to study pre-equilibrium processes in nuclear collisions. One involves the measurement of two particle correlation functions to investigate the space and time extent of the system which emits the particles we detect. The other involves the measurement of excited state populations to investigate the internal excitation achieved in the reaction. In this chapter, I will discuss the relationship between these two techniques, and the detailed procedures needed to construct and interpret the correlation functions and excited state populations. The procedures to assess the influence of sequential feeding from higher lying particle unstable states upon the population probabilities will also be discussed.

## 3.1 General description of correlation function and excited state population

The relationship between correlation function and excited state populations measurement has been investigated in the limit of thermal equilibrium by Jennings et al. [Jenn 86]. To illustrate the connection between these two observables, we reproduce their arguments here.

In the limit that the two detected particles interact mainly with each other and the interaction with the rest of the system may be neglected, the density of states of these two particles can be separated into two parts,

$$\rho(p_1, p_2) = \rho_0(P) \cdot \rho(q) \tag{3.1}$$

Here $\rho_0(P) = VP^2/(2\pi^2)$ is the density of states associated with the center of mass motion of the two particles. V is the volume of the system and P is the total momentum of the two particles. The second term $\rho(q)$ is the density of states of relative motion of the two particles. It can be further separated into,

$$\rho(q) = \rho_0(q) + \Delta\rho(q) \tag{3.2}$$

where $\rho_0(q)$ is the density of states of non-interacting particles, and $\Delta\rho(q)$ contain the modifications of the phase space due to the interactions between the two particles. The non-interacting term $\rho_0(q)$ can be written as,

$$\rho_0(q) = (2s_1 + 1) \cdot (2s_2 + 1) \cdot \frac{Vq^2}{2\pi^2} \tag{3.3}$$

where $s_1$ and $s_2$ are spins of the two particles respectively. The interacting term, $\Delta\rho(q)$ can be written as [Land 80, Huan 63],

$$\Delta\rho(q) = \frac{1}{\pi} \cdot \sum_{J,a}(2J + 1) \cdot \frac{\partial\delta_{J,a}}{\partial q} \tag{3.4}$$

where $\partial\delta_{J,a}/\partial q$ is the phase shift caused by the interactions between the two particles. J is the total angular momentum of the particle pair and $\alpha$ indicates the other quantum numbers of the channel. For a thermal distribution, the yield of $i$th particle (i=1,2) is,

$$Y_i(p_i) \propto \rho_0(p_i) \cdot e^{-E_i/T} d^3p_i \tag{3.5}$$

and the yield of the two interacting particles is,

$$Y_{12}(p_1, p_2) \propto \rho(P, q) \cdot e^{-(E_1+E_2)/T} d^3p_1 d^3p_2 \tag{3.6}$$

Combining these two expressions, one can write the correlation function as,

$$\begin{aligned} R(q) &= \frac{Y_{12}(p_1, p_2)}{Y_1(p_1) \cdot Y_2(p_2)} - 1 \\ &= \frac{2\pi}{(2s_1+1)(2s_2+1) \cdot V \cdot q^2} \sum_{J,a} (2J+1) \cdot \frac{\partial \delta_{J,a}}{\partial q} \end{aligned} \tag{3.7}$$

The correlation functions described by the thermal model thus depend inversely upon the volume of the source and not upon the temperature of the system. The dependence upon the interaction is represented by the phase shift term $\delta_{J,a}/\partial q$ . Further calculation by Jennings et al. [Jenn 86] have shown that the shape of the correlation predicted by Equation 3.7 is similar to those predicted by other, more frequently used, interferometry formulas. It should be noted that the result of equation 3.7 depends on the property that the kinetic energy distribution of emitted fragments is characterized by the same temperature as the population probabilities. For non-equilibrium processes, like we measured in this dissertation, this assumption is not satisfied. Correlation functions may then depend on the temperature of the emitting system.

The population of excited states is given by the interaction term of Equation 3.2 and the Boltzman factor,

$$\frac{dn(E)}{dE} = N \cdot e^{-E/T} \cdot \Delta\rho(q) \tag{3.8}$$

So in the thermal limit, the temperature of the reaction system can be obtained by measuring this excitation energy spectrum.

In the next two sections, I will show the detailed procedures used to extract the information about the reaction from these two techniques.

## 3.2 Correlation function analysis

The correlation function is defined experimentally by a ratio of coincidence and singles yields,

$$1 + R(P,q) = C_{12} \frac{\sum Y_{12}(p_1,p_2)}{\sum Y_1(p_1)Y_2(p_2)} \tag{3.9}$$

Here, $p_1$ and $p_2$ are the momenta of the two particles in the laboratory, $P = p_1 + p_2$ is the total momentum and $q = \mid \mu(v_1 - v_2) \mid$ is the relative momentum of the two particles. For each experimental gating condition, the sums on Equation 3.9 are extended over all energies, positions and detector combinations corresponding to specific relative and total momentum bins. The normalization constant $C_{12}$ in Equation 3.9 is chosen so that R(P,q) vanishes at large relative momenta where final state interactions between the two particles become negligible.

Theoretically, the two particle correlation function can be obtained from any theory which makes predictions for the one body Wigner transform or phase space distribution. We use a generalized formalism developed by Pratt [Prat87, Gong 90]. In this formalism, the two proton correlation functions is calculated via the equation,

$$1 + R(P,q) = \int d^3r F_P(r) \mid \phi(q,r) \mid^2 \tag{3.10}$$

Here $\phi$(q,r) is the two-particle relative wave function. The source density distribution $F_p(r)$ is obtained from one particle Wigner transform according to,

$$F_P(r) = \frac{\int d^3R f(P/2, R + r/2, t_>) f(P/2, R - r/2, t_>)}{\mid \int d^3r' f(P/2, r', t_>) \mid^2} \tag{3.11}$$

The Wigner transform $f(p,x,t)$ in Equation 3.11 describes the phase-space distribution of particles of momentum p and position x at some time, $t_>$, after the emission

process. It can be obtained from the probability distribution, g(p,r,t), for emitting a particle of momentum p at location r and time t by

$$f(p,r,t_>) = \int_{-\infty}^{t_>} dt\, g[p, r - p(t_> - t)/m, t] \tag{3.12}$$

With this formula, we can calculate the correlation function for any arbitrary source density distribution. For example, a Gaussian source of radius $r_0$ and lifetime $\tau$ is widely used to calculate correlation functions. In this case,

$$g(p,r,t) = \rho_0 e^{-r^2/r_0^2} e^{-t^2/\tau^2} \tag{3.13}$$

Surface emission from a target-like residue with a certain lifetime $\tau$, can be approximated by the following formula,

$$g(p,r,t) \propto \rho_0 \frac{d^3\sigma}{dp^3}(\hat{r}\cdot\hat{p})\Theta(\hat{r}\cdot\hat{p})\delta(R_s - r)[\frac{e^{-t/\tau}}{\tau}]\Theta(t) \tag{3.14}$$

Here, $\rho_0$ is a normalization constant, $\Theta(t)$ is the unit step function, $\tau$ is the source lifetime, $\delta$ is the Dirac delta function, $\hat{r}$ and $\hat{p}$ are the unit vectors for position and momentum, and $d^3\sigma/dp^3$ may be determined by moving source fits to the single particle inclusive spectrum.

By assuming a source distribution function, and fitting a correlation function to the experimental data, one can extract information about the space time evolution of the emitting source. The correlation function can also be used to test any dynamical theory which makes predictions for Wigner transform in equation 3.11. One widely used reaction dynamics model is the Boltzmann-Uehling-Uhlenbeck (BUU) transport equation [Bert 84, Bert 88],

$$\begin{aligned}\partial_t f(p,r,t) + \frac{p}{m}\nabla_r f(p,r,t) - \nabla_r U(r)\,\nabla_p f(p,r,t) \\ = \frac{1}{2\pi^3 m^2}\int d^3q_2 d^3q_1' d^3q_2' \delta[\frac{1}{2m}(p^2 + q_2^2 - q_1'^2 - q_2'^2)]\end{aligned}$$

$$\delta[p_1 + q_2 - q_1^{'} - q_2^{'}]\frac{d\sigma}{d\Omega}$$
$$\{\hat{f}(q_1^{'}, r, t)\hat{f}(q_2^{'}, r, t)[1 - \hat{f}(p, r, t)][1 - \hat{f}(q_2, r, t)]$$
$$-\hat{f}(p, r, t)\hat{f}(q_2, r, t)[1 - \hat{f}(q_1^{'}, r, t)][1 - \hat{f}(q_2^{'}, r, t)]\} \tag{3.15}$$

This equation describes the motion and emission of nucleons under the influence of a self consistent mean field, nucleon-nucleon collisions and the Pauli-exclusion principle, but does not describe the emission of clusters. It has been used to calculate the correlation functions and has been successfully compared with the experimental data [Gong 90].

## 3.3 Excited state population measurements

The population of excited states of fragments emitted in a nuclear reaction can be used to extract the temperature of the fragmenting system at the time of emission. Suppose a nucleus A in an excited state with excitation energy E decays to two daughter nuclei b and c.

$$A^* \rightarrow b + c \tag{3.16}$$

We can observe this decay by measuring fragments b and c in coincidence. From their energy and angle in the laboratory frame, we can deduce the excitation energy E* of parent nucleus in its rest frame and construct a decay spectrum. The experimentally measured decay spectrum $Y_{exp}(E^*_{mea})$ consists of two parts,

$$Y_{exp}(E^*_{mea}) = Y_c(E^*_{mea}) + Y_b(E^*_{mea}) \tag{3.17}$$

$Y_c(E^*_{mea})$ is the decay spectrum for the correlated decay products from the particle unstable parent fragment A. and $Y_b(E^*_{mea})$ is the background from pairs of particles which do not originate from parent fragment A. While the detailed calculation of the

background yields from first principle requires an extremely detailed knowledge of the reaction, it can be accurately parameterized by,

$$Y_b(E^*_{mea}) = C_{12}(1 - exp^{-(E-E_b)/\Delta})Y_1 \cdot Y_2 \cdot \Theta(E - E_b) \tag{3.18}$$

Here $E_b$ is the threshold for the decay $A^* \rightarrow b+c$ and $\Delta$ is the width of the suppression of the background correlation function due to Coulomb final state interactions. $Y_1$ and $Y_2$ are the single particle yields.

The measured decay spectrum $Y_c(E^*_{mea})$ of the particle unstable nucleus A can be written as

$$Y_c(E^*_{mea}) = \int dE^* \epsilon(E^*, E^*_{mea}) \left| \frac{dn(E^*)}{dE^*} \right|_c \tag{3.19}$$

where $E^*$ is the true excitation energy of nucleus $A^*$, $dn(E^*)/dE^*$ is the decay spectrum in the rest frame of nucleus $A^*$. $E^*_{mea}$ is the measured excitation energy and $\epsilon(E^*, E^*_{mea})$ is the efficiency function of the device and will be discussed in the next section.

From equation 3.8, the excitation energy spectrum $dn(E^*)/dE^*$ depends on the phase shift caused by the interaction of the coincident fragments.

$$\begin{aligned} \frac{dn(E^*)}{dE^*} &= N \cdot e^{-E^*/T} \cdot \Delta\rho(q) \\ &= N \sum_i e^{-E^*/T} \cdot \frac{1}{\pi} \cdot (2J_i + 1) \cdot \frac{\partial \delta_{i,res}}{\partial E^*} \end{aligned} \tag{3.20}$$

Here $\delta_{i,res}$ and $J_i$ are phase shifts and spins of the resonances. N is a normalization constant. If the phase shifts are dominated by a set of isolated resonances, one can write

$$\frac{dn(E^*)}{dE^*} = \sum_\lambda \frac{dn_\lambda(E^*)}{dE^*} \tag{3.21}$$

If the individual levels are described by a R-Matrix parameterization [Naya 92], the individual terms in Equation 3.21 become

$$\frac{dn_\lambda(E^*)}{dE^*} = N_\lambda \cdot e^{-E^*/T} \cdot \frac{2J_\lambda + 1}{\pi} \frac{\Gamma_\lambda/2}{(E_\lambda + \Delta_\lambda - E^*)^2 + \Gamma_\lambda^2/4}$$
$$\times \left[1 - \frac{d\Delta_\lambda}{dE^*} + \frac{E_\lambda + \Delta_\lambda - E^*}{\Gamma_\lambda} \cdot \frac{d\Gamma_\lambda}{dE^*}\right] \tag{3.22}$$

Multiplying Equation 3.22 by the branching ratio $\Gamma_{\lambda c}/\Gamma_\lambda$ for channel c, and summing over $\lambda$ when more than one level is involved, one obtains,

$$\left|\frac{dn(E^*)}{dE^*}\right| = \sum_\lambda \frac{dn_\lambda(E^*)}{dE^*} \cdot \frac{\Gamma_{\lambda c}}{\Gamma_\lambda} \tag{3.23}$$

Here, $\Gamma_\lambda = 2P_c\gamma_{\lambda c}^2$ is the partial width of the level $\lambda$ decaying to channel c, $\Gamma_\lambda = \sum_c \Gamma_{\lambda c}$ is the total width of the level, and $\Gamma_{\lambda c}/\Gamma_\lambda$ is the branching ratio of decaying from level $\lambda$ to channel c. The shift parameter is $\Delta_\lambda = \sum_c (S_c - B_c)\gamma_{\lambda c}^2$. The penetration factor, $P_c$ and $S_c$ can be expressed in terms of the regular (F) and irregular (G) radial Coulomb wave functions and their derivatives, all evaluated at channel radius $a_c$.

$$\begin{aligned} P_c &= \rho_c A_c^{-2}|_{r=a_c} \\ S_c &= \rho_c A_c^{-1} \cdot \frac{\partial A_c}{\partial \rho_c}|_{r=a_c} \end{aligned} \tag{3.24}$$

where $A_c^2 = F_c^2 + G_c^2$, and $\rho_c = k_c r$. The boundary conditions $B_c$, along with the other resonance parameters, will be defined for each level when we fit the data.

For narrow levels, $\Gamma_\lambda$ and $\Delta_\lambda$ can be treated as energy independent, and the R-matrix decay spectra can be further simplified to the Breit-Wigner formula,

$$\left|\frac{dn_\lambda(E^*)}{dE^*}\right|_c = N_\lambda \cdot e^{-E^*/T} \cdot \frac{2J_\lambda + 1}{\pi} \frac{\Gamma_\lambda/2}{(E_{res} - E^*)^2 + \Gamma_\lambda^2/4} \frac{\Gamma_{\lambda c}}{\Gamma_\lambda} \tag{3.25}$$

For a more complicated case involving two overlapping states with the same spin and parity, the appropriate R-matrix formula can be found in ref. [Naya 92].

The excitation energy spectrum, when folded with the efficiency function using equation 3.19, provide a theoretical expression for the coincidence yields. Combining this with the background parameterization of equation 3.18, one can fit the experimentally measured decay spectrum to obtain the population probability $n_\lambda$ for each level. Following [Naya 92], we define the population probability for a particular excited state by integrating the excitation energy spectrum for level $\lambda$ over excitation energy,

$$n_\lambda = \frac{1}{2J_\lambda + 1} \int dE^* \frac{dn_{\lambda,tot}(E^*)}{dE^*} \tag{3.26}$$

For most of the excited states considered, the excited states are sufficiently narrow that the Boltzman factor, $e^{-E^*/T}$, varies little over the resonance and can be approximated at the resonance energy $e^{-E_{res}/T}$, and taken out of the integral. The population probability is defined as,

$$n_\lambda = N_\lambda e^{-E_{res}/T} \tag{3.27}$$

In this case, the Breit-Wigner formula for a group of levels can be written as,

$$\left|\frac{dn(E^*)}{dE^*}\right|_c = \sum_\lambda n_\lambda \frac{2J_\lambda + 1}{\pi} \frac{\Gamma_\lambda/2}{(E_{res} - E^*)^2 + \Gamma_\lambda^2/4} \frac{\Gamma_{\lambda c}}{\Gamma_\lambda} \tag{3.28}$$

## 3.4 Hodoscope response function simulation

In this section, some details of hodoscope response function calculation for the decay of an excited nucleus $A^*$ decaying to two daughter nuclei b and c, $A^* \rightarrow b + c$ are provided.

In the experiment, we detect the decay fragments b and c in coincidence. From their energy and angles in the laboratory frame, we can deduce the excitation $E^*_{mea}$

of the parent nucleus A*. Since we have finite energy and position resolution for our detection devices, $E^*_{mea}$ could be different from the original excitation energy E*. This difference must be calculated.

Several conditions are assumed in our calculations of efficiency function $\epsilon(E, E^*)$. The kinetic energy spectrum of the parent nucleus A with excitation energy E is assumed to be the same as the measured energy spectrum for stable nuclei of the same isotope. The decay of parent nucleus A to its daughter nuclei b + c is assumed to be isotropic in the rest frame of parent nucleus A. Assuming these conditions, the coincidence cross section of detecting two daughter nuclei b and c in the laboratory frame is

$$\frac{d\sigma(E_1,\Omega_1,E_2,\Omega_2)}{dE_1 d\Omega_1 dE_2 d\Omega_2}$$

$$= \frac{\partial(E_{rel},\Omega_{cm},E_{tot},\Omega_{tot})}{\partial(E_1,\Omega_1,E_2,\Omega_2)} \cdot \frac{d\sigma(E_{tot},\Omega_{tot})}{dE_{tot}d\Omega_{tot}} \cdot \frac{1}{4\pi} \cdot \frac{dn(E^*)}{dE^*} \tag{3.29}$$

where $\partial(E_{rel},\Omega_{cm},E_{tot},\Omega_{tot})/\partial(E_1,\Omega_1,E_2,\Omega_2)$ is the Jacobian for the transformation of total and relative quantities $E_{rel},\Omega_{cm},E_{tot},\Omega_{tot}$ to the individual quantities $E_1,\Omega_1,E_2,\Omega_2$; $1/4\pi \cdot dn(E^*)/dE^*$ is the decay spectrum of $A^* \rightarrow b + c$ in the center of mass frame; and $d\sigma(E_{tot},\Omega_{tot})/dE_{tot}d\Omega_{tot}$ is the energy spectrum for stable nucleus of the same mass in the laboratory frame. The cross section in Equation 3.29 is then integrated over the detection array to get the experimental yield $Y_c(E^*)$ for the detection of daughter nuclei b and c.

In order to reproduce the measured excitation energy spectrum, the coincident cross section in equation 3.29 must be folded with the energy and angular resolution of the experimental array. These effects include corrections for angular straggling in the target and detectors. Since the energy spectrum of stable nuclei of the same isotope are used here as input for the yield calculations, the yields of individual excited states is defined with respect to the yields of stable nuclei of same isotope. In this

respect, many uncertainties due to the target thickness or beam current cancel out.

Figure 3.1 shows the efficiency function (arbitrarily normalized) and the excitation energy resolution of the 13 element hodoscope for the decay of $^{10}$B nuclei emitted in the $^{36}$Ar + $^{197}$Au reaction at E/A = 35 MeV. The total efficiency function $\epsilon$(E) is defined by,

$$\epsilon(E^*) = \int dE^*_{mea} \epsilon(E^*, E^*_{mea}) \tag{3.30}$$

The energy resolution $\delta$E shown in Figure 3.1 is defined by a root mean square difference between $E^*_{mea}$ and $E^*$,

$$\delta E^* = \{ \int dE^*_{mea} \epsilon(E^*, E^*_{mea})(E^*_{mea} - E^*)^2 \}^{1/2} \tag{3.31}$$

To check this efficiency program, it was compared to an event generating Monte Carlo simulation program which use a completely different algorithm to calculate the efficiency function [Poch 87]. Both codes were used to calculate the efficiency of an 18 element hodoscope for the decay: $^5Li \rightarrow p + \alpha$ for $^{16}$O + $^{197}$Au reactions at E/A = 94 MeV [Chen 87a, Chen 87b]. The comparison of the two calculations is shown in the top panel of Figure 3.2. The line is the direct integration technique used in this dissertation [Mura 89] and the solid points are the Monte Carlo calculations of reference [Poch 87]. The two methods agrees very well over a wide range of excitation energies. The bottom panel shows the ratio of the two calculations (calculation from Monte Carlo method is divided by calculation from integration method). Considering the differences in the techniques used in the two calculations, the agreement between these two methods is very reasonable.

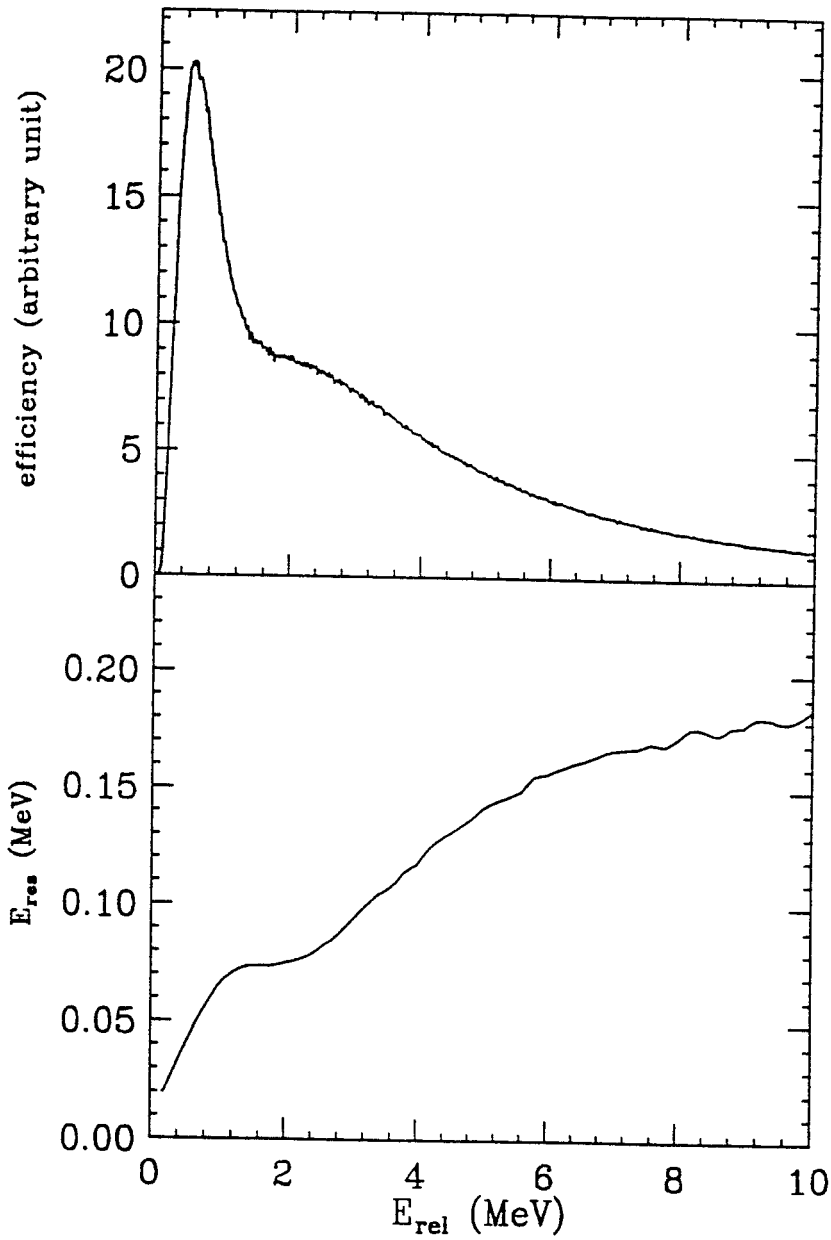


Figure 3.1: The efficiency function and energy resolution calculations of detecting $^{10}$B nuclei excited states in the $^{36}$Ar + $^{197}$Au reaction at E/A = 35 MeV.

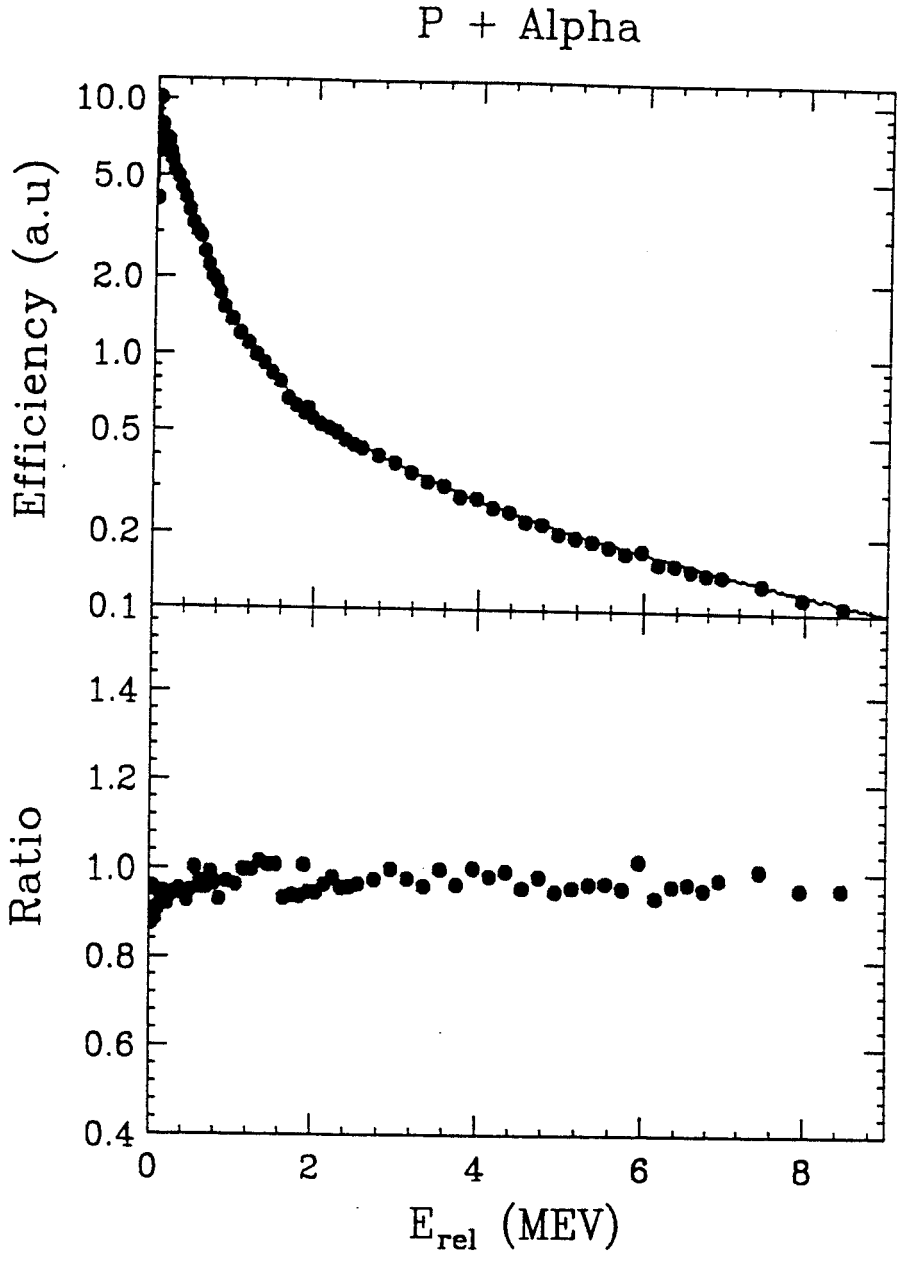


Figure 3.2: The comparison of two efficiency function calculation programs of detecting $^{5}$Li nuclei excited states in the $^{16}$O + $^{197}$Au reaction at E/A = 94 MeV. The solid lines are the integration method used in this thesis and the solid points are the Monte Carlo simulations. The bottom panel shows the ratio of the two calculations.

## 3.5 The sequential decay calculations

While temperatures deduced from excited state populations are not affected by the collective motion of the colliding system, they are sensitive to sequential feeding from higher lying heavier particle unstable nuclei. For example, $^{10}$B particle unstable excited states can particle decay to $^{6}$Li and $\alpha$, ie, $^{10}B^{*} \rightarrow^{6} Li + \alpha$ . Both $^{6}$Li and $\alpha$ can be in a ground state or in an excited state. In this case, these daughter fragments, $^{6}$Li and $\alpha$, will increase the total populations of the respective $^{6}$Li and $\alpha$ states, thus altering these populations from their initial values. Experimental measurements will include these additional contributions from sequential feeding. The experimentally measured temperature, derived from the population ratio of excited states yields to their ground state yields, is therefore affected by the sequential feeding from such higher lying states . In this section, I will address this issue and discuss calculations to take this sequential feeding into account and to make the corresponding corrections when extracting the temperature.

### 3.5.1 The initial fragment yield population

Of course the exact fragment yield distribution depends on the exact many body evolution of the nuclear reaction. As this information is not available, statistical model calculations can be useful for describing the population and decay of the particle unstable fragments. In this approach, the nuclear reaction system is assumed to be fully equilibrated at the **freezeout** time after which all the fragments cease to interact with each other. Statistically, the yields of fragments and their excited state populations are dictated by the temperature as well as spins, parities, the binding energies, excitation energies and densities of excited states of the emitted fragments. Taking these effects into consideration, one may predict the **primary populations** of

excited states of emitted fragments. These will be altered later on by any subsequent sequential decay of the intial fragments. Since we are primarily interested in the intial temperature of the emitted fragments, we must perform calculations to correct for the influence of sequential feeding to the excited state populations.

We assume that the initial population of a particular excited state at excitation energy E* and spin J of a nucleus with mass number A and charge number Z can be written as

$$P_i(A, Z, E^*) \propto P_0(A, Z)\rho(E^*, J)exp(-E^*/T_{em}) \tag{3.32}$$

where $P_0(A, Z)$ is the probability of populating the nucleus with mass number A and charge number Z at its ground state. $\rho(E^*, J)$ is the density of levels of that nucleus with the same excitation energy E* and spin J.

The population probability of ground state nuclei with charge number Z and mass number A can be parameterized by

$$P_0(A, Z) \propto exp(-fV_c/T_{em} + Q/T_{em}) \tag{3.33}$$

the Coulomb barrier is parameterized by

$$V_c = \frac{Z(Z_p - Z)e^2}{r_0[A^{1/3} + (A_p - A)^{1/3}]} \tag{3.34}$$

where $A_p, Z_p$ are the total mass and charge number of the fragmenting system and $r_0 = 1.2$fm. The constant $f$ is adjusted to provide an optimal agreement between the calculated final charge distribution and the measured charge distribution [Naya 92]. Clearly, Equation 3.33 represents a simplification of the emission mechanism. For example, in a real statistical model calculation, one has to consider the free energy besides the Coulomb energy and binding energy [Frid 83]. The adjustment of $f$ could

partially be regarded as a compensation for the neglect of this effect and other effects. The Q value of the ground state is calculated from the expression,

$$Q = B(A_p - A, Z_p - Z) + B(A, Z) - B(A_p, Z_p). \tag{3.35}$$

The binding energy B(A,Z) was calculated from the empirical Weizsacher formula [Marm 69],

$$B(A, Z) = C_0 A - C_1 A^{2/3} - C_2 \frac{Z^2}{A^{1/3}} - C_3 \frac{(A - 2Z)^2}{A} \tag{3.36}$$

Here, $C_0$ = 14.1 MeV is the volume term, $C_1$ = 13.0 MeV is the surface term, $C_2$ = 0.595 MeV is the Coulomb term, and $C_3$ = 19.0 MeV is the pairing term.

Here the temperature $T_{em}$ is assumed to be a constant. By doing this, we neglect time evolution of the temperature due to expansion and particle emission. Cooling and expansion of the excited system will give rise to a distribution of a temperatures instead of a single temperature [Frid 88, Frid 90].

### Density of states

The definition of density of levels with excitation energy $E^*$ and spin J is

$$\rho(E^*, J) = \sum_i \delta(E_i - E^*)\delta_{J_i,J} \tag{3.37}$$

where the sum runs over all possible states of the particle unstable fragment. For discrete states at low energy, $E^* \leq \varepsilon_0$ we can just count all the states from a compilation of all the experimentally known states [Ajze 87]. For higher excitation energies, $\varepsilon_0 < E^* < E^*_{max}$, where the density of states is not well known experimentally, the continuous approximation is used

$$\rho(E^*, J) = \frac{(2J+1)exp[\sqrt{a(E^* - E_0)}]}{24\sqrt{2}a^{1/4}\sigma^3(E^* - E_0)^{5/4}} \cdot exp[\frac{-(J+1/2)^2}{2\sigma^2}] \tag{3.38}$$

where the spin cut off parameter $\sigma$ is parameterized by [Gilb 65a, Gilb 65b],

$$\sigma^2 = 0.0888[a(E^* - E_0)]^{1/2}A^{2/3} \tag{3.39}$$

where $a = A/8$ is the level density parameter. The energy $E_0$ is chosen so that the number of levels at $E < \varepsilon_0$ is the same for both expressions.

$$\int_{E_0}^{\varepsilon_0} dE^* \int dJ\{\frac{(2J+1)exp[\sqrt{a(E^* - E_0)}]}{24\sqrt{2}a^{1/4}\sigma^3(E^* - E_0)^{5/4}} \cdot exp[\frac{-(J+1/2)^2}{2\sigma^2}]\}$$

$$= \int_0^{\varepsilon_0} \{\sum_i \delta(E_i - E^*)\} \tag{3.40}$$

To illustrate this matching procedure, the level density of $^{20}$Ne nuclei is plotted in Figure 3.3 as a function of its excitation energy [Chen 88]. The histogram indicates the experimentally known states. At $\epsilon_0 \geq 13$ MeV, the level density decrease with $E^*$, because of incomplete experimental information for states at higher excitation energies. The curve is the level density from the calculation of Equation 3.38. For nuclei of $12 \leq Z \leq 20$, a continuous approximation is used for all the excitation energies. At high excitation energies, $E^* > \epsilon_0$, Equation 3.38 is used to describe the level density. At low excitation energies, $E^* \leq \epsilon_0$, the empirical expression of Reference [Gilb 65b] was modified to take the spin dependence of the level density into account [Chen 88],

$$\rho(E^*, J) = \frac{1}{T}exp[\frac{(E^* - E_1)}{T}\frac{(2J+1)exp[-(J+1/2)^2/2\sigma^2]}{\sum(2J+1)exp[-(J+1/2)^2/2\sigma^2]} \tag{3.41}$$

Here, the parameters $E_1$, T, and $\epsilon_0$ were taken from [Gilb 65b]; $\sigma$ is calculated using Equation 3.39 at $E^* = \epsilon_0$ and is assumed to be the same constant for $E^* \leq \epsilon_0$. For $E^* > \epsilon_0$ the continuum level density of Equation 3.38 was used. It was matched to low energy Equation 3.41 at $E^* = \epsilon_0$ according to the matching conditions described in Equation 3.40.

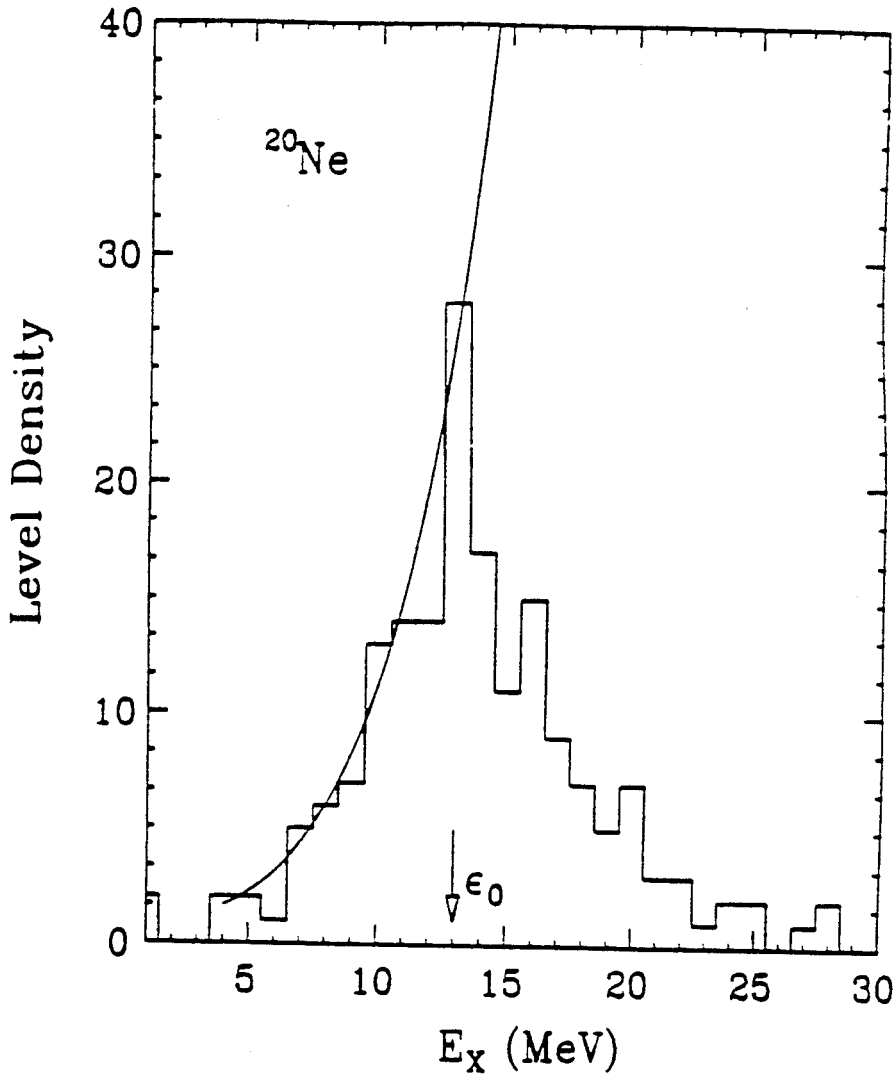


Figure 3.3: The level density of $^{20}$Ne plotted as a function of its excitation energy. The histogram is the level density from the experimentally known levels. The curve is the level density calculation with Equation 3.38.

Since the spins, isospins, and parities of low-lying particle states are known experimentally, a lookup table containing excitation energies, spins, isospins, parities, and branching ratios for approximately 2600 known levels was constructed, and used in the sequential decay calculations [Ajze 87]. In the real computer program, the continuum states were treated as discrete states of interval 1 MeV for $E^* \leq 15$ MeV, 2 MeV for $15 < E^* < 30$ MeV, 3 MeV for $E^* \geq 30$ MeV. Parities of continuum states were chosen to be positive or negative randomly with equal probability, the isospins were taken to be equal to the isospin of the ground state of the same nucleus.

### 3.5.2 The sequential decay from initial population

After the initial population, the excited states of the emitted nuclei will either particle decay to different daughter nuclei or $\gamma$ decay towards the ground state. Particle decay channels for n, 2n, p, 2p, d, t, $^3He$ and $\alpha$ emission were included in the calculation. Tabulated branching ratios were used when available for the decay of particle unstable excited states. Where such information is not available, the branching ratios were calculated from the Hauser-Feshbach formula [Haus 52], taking into account constraints imposed by isospin and parity conservation. The branching ratio for a channel c was taken to be

$$\frac{\Gamma_c}{\Gamma} = \frac{G_c}{\sum_i G_i} \tag{3.42}$$

where

$$\begin{aligned} G_c =& < T_{I,D} T_{I,F} T(3)_{I,D} T(3)_{I,F} \mid T_{I,P} T(3)_{I,P} >^2 \\ & \times \sum_{Z=|S-l|}^{|S+l|} \sum_{l=|J-Z|}^{|J+Z|} \{[1 + \pi_P \pi_D \pi_F (-1)^l]/2\} T_l(E) \end{aligned} \tag{3.43}$$

Here, J and I are the spins of the parent and daughter nuclei, Z is the channel spin, S and $l$ are the intrinsic spin and orbital angular momentum of the emitted

particle, and $T_l$ is the transmission coefficient for the $l$th partial wave. The factor $[1 + \pi_P \pi_D \pi_F (-1)^l]$ enforces parity conservation, and the Clebsch-Gordon coefficient takes isospin conservation into account.

For decays from states when the kinetic energy of the emitted particle is less than 20 MeV and $l \leq 20$, the transmission coefficients were interpolated from a set of calculated optical model transmission coefficients. For decays from continuum states when the kinetic energy of the emitted particles exceeds 20 MeV, the transmission coefficients were approximated by the sharp cut off approximation.

$$T_l(E) = \begin{cases} 1, & if \ \ l \leq l_0 \\ 0, & if \ \ l > l_0 \end{cases} \tag{3.44}$$

the cut off angular momentum is

$$l_0 = \frac{2\pi}{h} r_0 [A^{1/3} + (A_p - A)^{1/3}] \sqrt{2\mu(E - V_C)} \tag{3.45}$$

where $\mu$ is the reduced mass and h is Plank's constant.

### 3.5.3 The final fragment yield population

As an important prerequisite for calculating the final population ratios for the excited states of emitted fragments, we must ensure that we can reproduce the observed elemental distributions for the fragments. In order to reproduce the measured elemental distribution, the ground state populations are adjusted by varying the constant $f$ in Equation 3.33 which multiplies the Coulomb potential.

Figure 3.4 provides a a comparison of measured and calculated charge distributions for the $^3He$+$Ag$ reaction at $E_{beam}$ = 200 MeV for a range of initial temperatures. Since a wide range of intermediate mass fragments were not detected in our experiment, we use the charged particle distributions from ref. [Kwia 86] for the same reaction.

The solid points are these experimental data and the histograms are the sequential decay calculations for various initial temperatures. The corresponding adjustment constants $f$ are shown in the figure as well. Figure 3.5 provides the corresponding charge distributions measured for the $^{36}Ar+^{197}Au$ reaction at E/A=35 MeV. In order to reduce the effect of the detector threshold, a common threshold of E/A $>$ 5 MeV is used for all particles in this plot.

These are the elemental distributions which result from the calculations used to predict the effects of sequential decay upon the population probabilities. The population probabilities will be compared with experimental measurements in chapters 4 and 5.

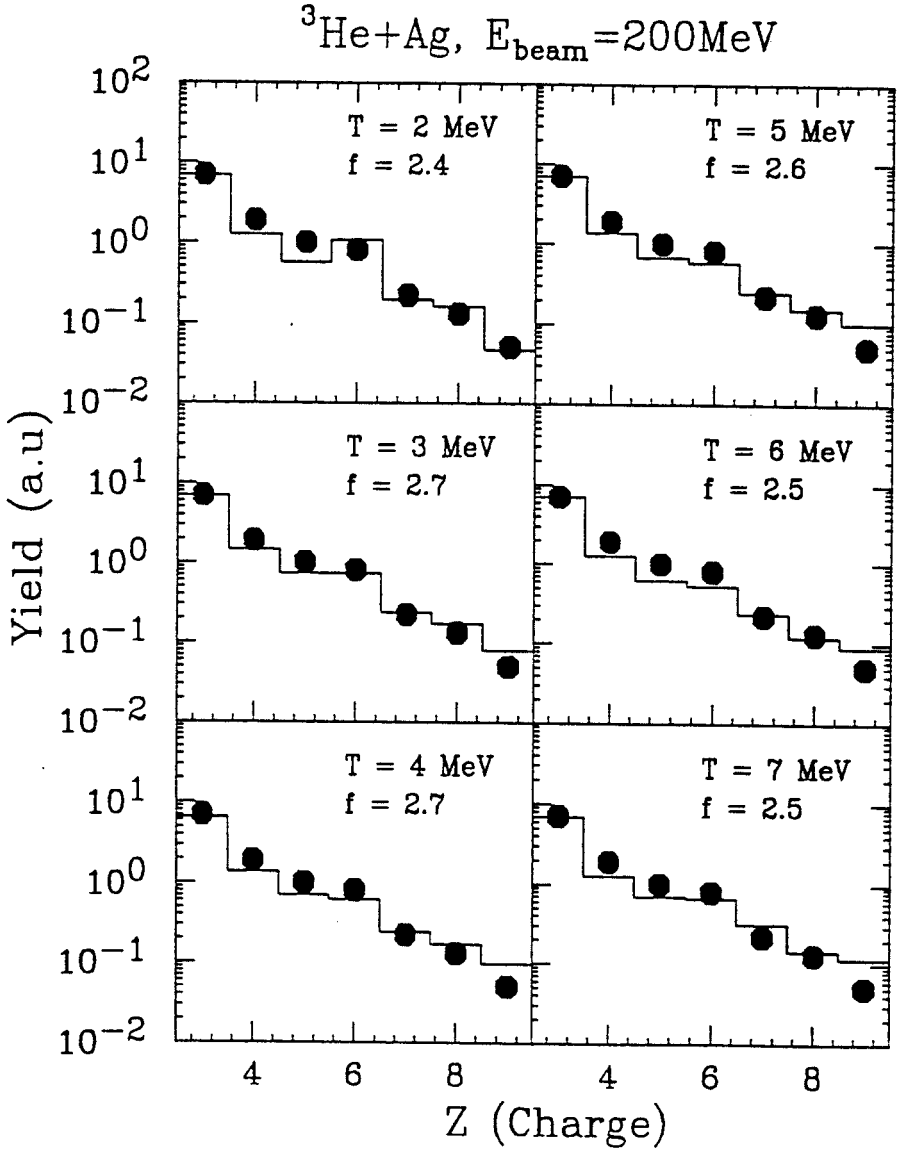


Figure 3.4: The charged particle yield distribution compared with the sequential decay calculations for $^3He + Ag$ reactions at $E_{beam}$ = 200 MeV.

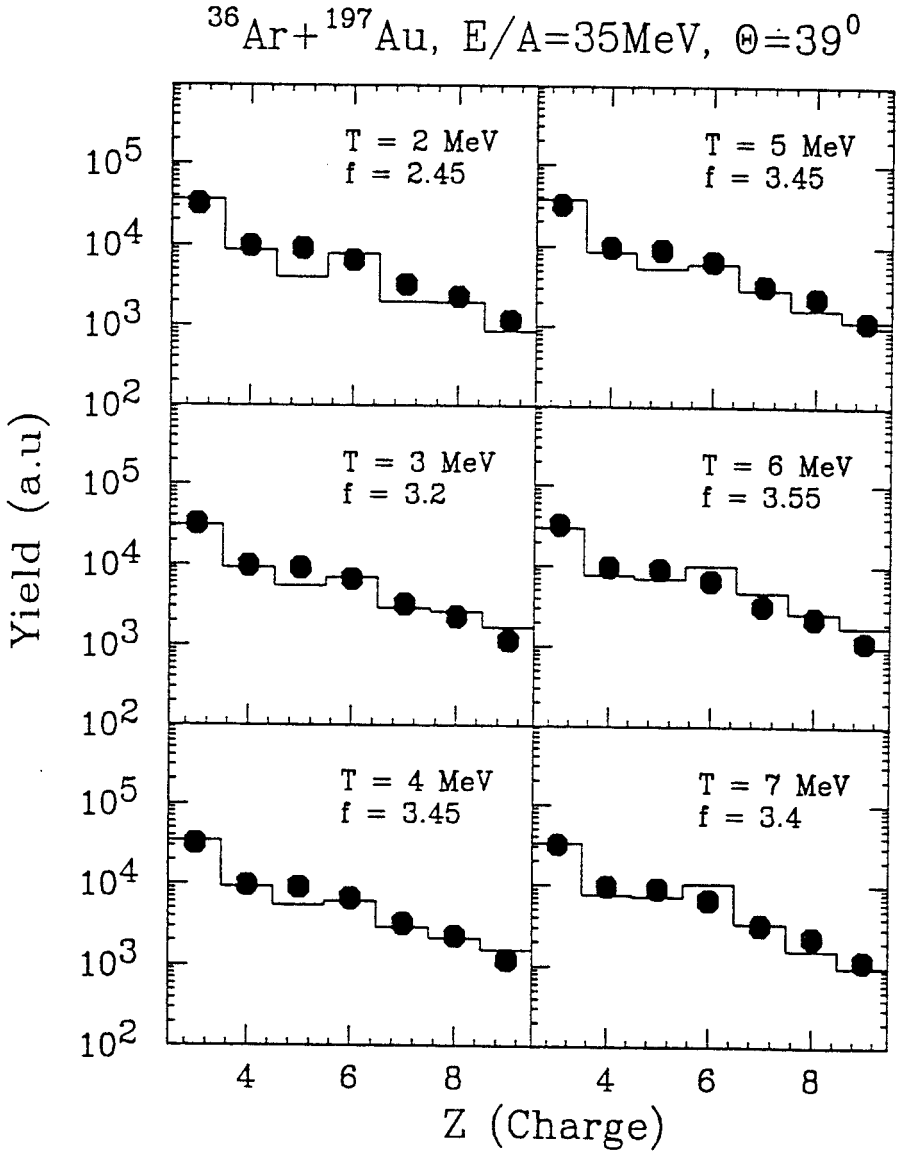


Figure 3.5: The charged particle yield distribution compared with the sequential decay calculations for $^{36}Ar + ^{197}Au$ reactions at E/A=35 MeV.

# Chapter 4

# $^3$He + Ag reaction at $E_{beam}$ = 200 MeV

This measurement of $^3$He + Ag reactions at $E_{beam}$ = 200 MeV was performed at the Indiana University Cyclotron Facility. A natural 1.05 mg/cm2 Ag target was bombarded by 200 MeV $^3$He ions. In this experiment, the hodoscope was used as a stand alone device to detect the decay of particle unstable states of emitted fragments. Since the $^3$He projectile deposits very little excitation energy, the yield of intermediate mass fragments (IMF) is small. Thus the experiment focused on the decays of lighter IMF's, for which the cross sections were larger.

Single particle inclusive energy spectra can shed some light on particle production mechanisms in general. Such spectra are also required to construct the correlation background yields and to calculate the efficiency functions needed to describe the particle unstable excited states measurements. In this chapter, such data will be discussed first, and followed by a discussion of two particle coincidence data and analyzed in terms of two particle correlation functions and particle unstable excited state populations.

## 4.1 Single particle cross section

There are many possible sources of particle emission, the evaporation of fully equilibrium compound nuclei [Frid 83], pre-equilibrium particle emission, the complete multifragmentation of the nuclear system [Kim 89, Bowm 91], to name a few. The energy spectrum of the emitted particles can provide information about the possible sources of particle emission. In reactions leading to the production of a target like residue, the residue will decay according to statistical evaporation models [Haus 52, Frid 83, Sobo 83]. Such is the case for both $^{3}$He + Ag and $^{36}$Ar + $^{197}$Au reactions investigated in this dissertation. The energy spectrum of particles which were evaporated from such residues could be approximated by a single Maxewell distribution as discussed by Eq. 1.13. This approximation can also be used for particles emitted from a projectile like residue should one exist. Experimentally, it has been shown that one can approximately describe pre-equilibrium emission by a thermal source source at about 1/2 the beam velocity [Chit 86a, Awes 81]. Thus we have modified Equation 1.13 to obtain

$$\frac{d^2\sigma}{dEd\Omega} = \sum_{i}^{3} N_i \sqrt{E - V_c} e^{-E_s/T} \tag{4.1}$$

with $E_s = E - V_c + E_0 - 2\sqrt{E_0 - V_C}\cos\theta$

In our investigation of the $^{3}$He + Ag reaction at $E_{beam}$ = 200MeV, we put the hodoscope at forward angle of $\Theta_{av} = 42^0$, and later at a backward angle of $\Theta_{av} = 109^0$, so that we could see the evolution of particle production from forward angles where non-statistical emission is dominant to backward angles where the emission from the target residue is dominant. This evolution can be seen in the measured proton inclusive cross sections shown in Figure 4.1. At low energies, E < 16 MeV, the spectra are dominated by evaporation from equilibrated or nearly equilibrated target residues.

At higher energies, non-equilibrium emission processes dominate, with some contributions from projectile breakup. These non-equilibrium higher energy contributions become less important with increasing angle. The energy gap at 25Me $< E_p <$ 32MeV is due to the dead layers at the end of the 5mm Si(Li) and at the entrance of the NaI(Tl) detector. Particle which stop in the dead layer can not be properly identified by their mass and charge. The dashed lines in the figure are moving source fits to the experimental data using Equation 4.1. The fitting parameters are listed in table 4.1. The solid histograms are the results of BUU calculations using Equation 3.15. A comparison of the energy spectra for different hydrogen isotopes are shown in Figure 4.2. A comparison of the energy spectra for $^3$He, $^4$He, and $^6$Li particles is shown in Figure 4.3. Moving source fits using Equation 4.1 are shown as the solid lines in the figure, and the extracted source parameters are listed in table 4.1. Compared to the spectra for protons and $\alpha$ particles, the contribution to the spectra from slow moving target like residues are less dominant for d, t, and $^3$He particles.

## 4.2 Proton-proton correlation functions

As discussed in the introduction, two particle correlation functions are sensitive to the space time development of a nuclear reaction as the colliding system evolves from initial contact to an equilibrated target like residue. The most dramatic effects should be manifested in light ion induced reactions on a heavy target, due to the small size of the initial system. Details of the analysis of the proton-proton correlation functions for the $^3$He + Ag reaction at $E_{beam}$ = 200 MeV are provided in this section.

We define the experimental correlation function R(q) in terms of the measured coincidence yield $Y_{12}(p_1, p_2)$ and the background yield which is constructed, assuming a mixed singles technique, from the product of an uncorrelated singles yield $Y_1(p_1)$

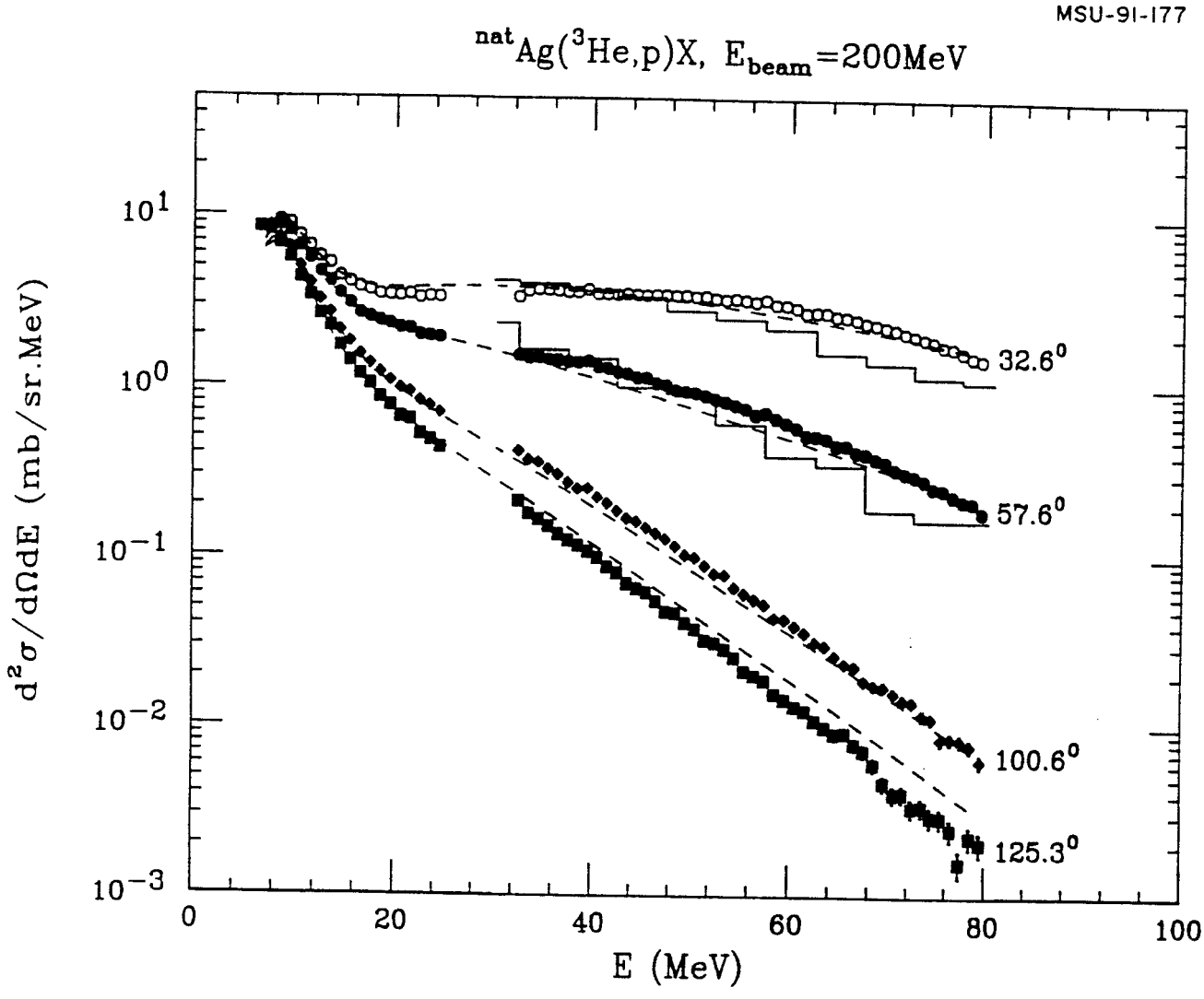


Figure 4.1: Single proton inclusive cross sections for the $^3$He + Ag reaction at 200 MeV. The laboratory angles are indicated in the figure. The curves are the corresponding moving source fits using Equation 4.1 with fitting parameters listed in table 4.1.

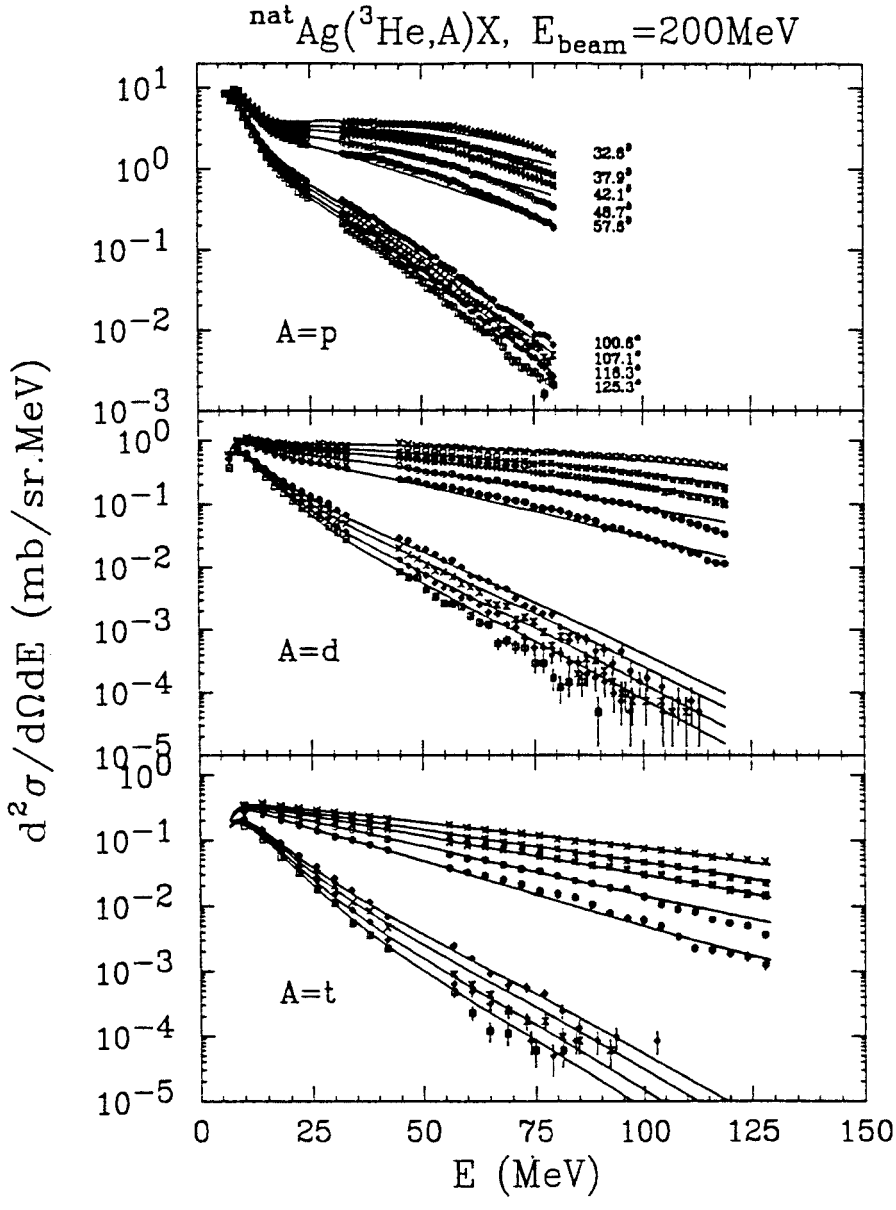


Figure 4.2: Single particle inclusive cross sections of p, d. t for the $^3$He + Ag reaction at 200 MeV are shown at the indicated laboratory angles. The solid lines are the corresponding moving source fits using Equation 4.1 with fitting parameters shown in Table 4.1.

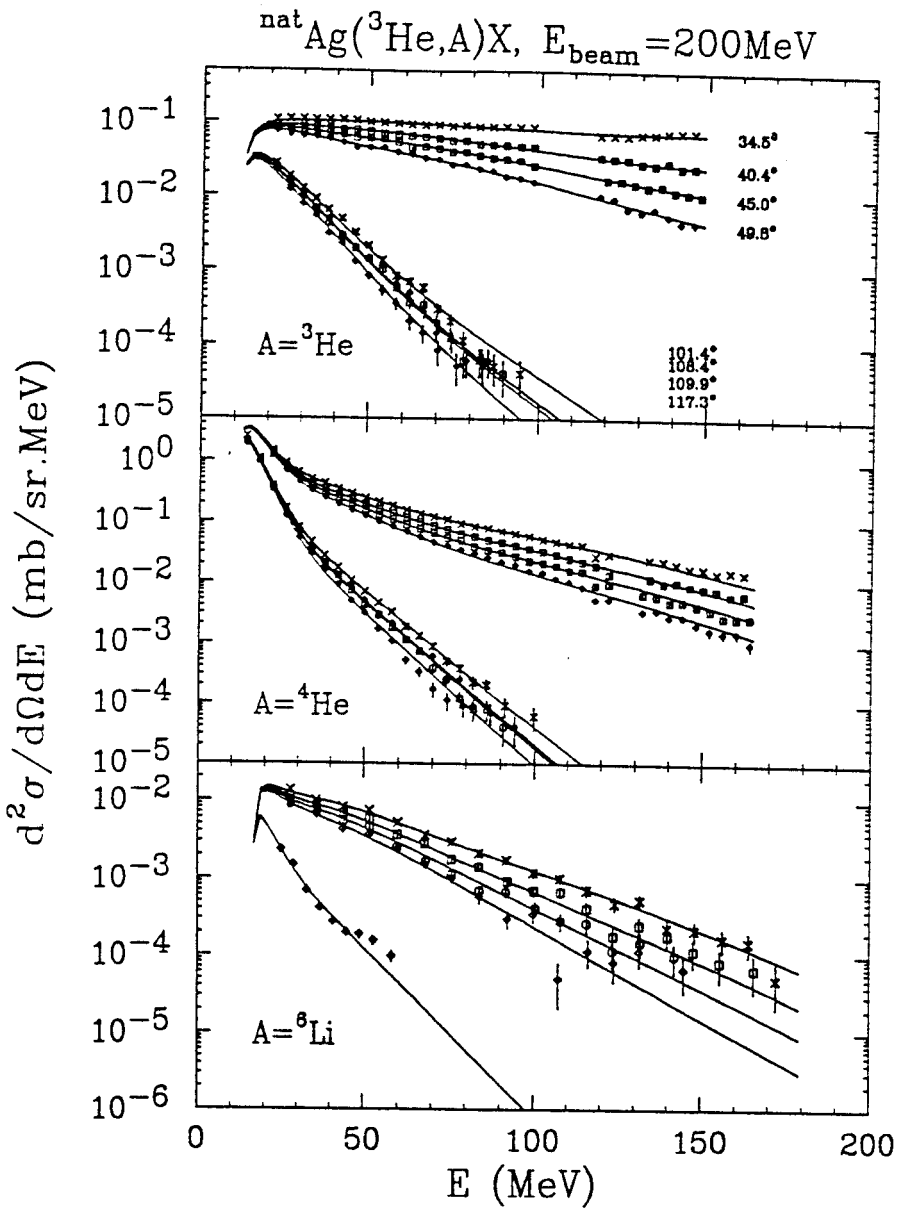


Figure 4.3: Single particle inclusive cross sections of $^3$He, $^4$He, $^6$Li for the $^3$He + Ag reaction at 200 MeV are shown at the indicated laboratory angles. The solid lines are the corresponding moving source fits using Equation 4.1 with fitting parameters shown in Table 4.1.

Table 4.1: The moving source fitting parameters of the energy spectrum for particles produced in $^3$He + Ag reaction at $E_{beam}$ = 200 MeV. The unit for $N_i$ is mb/MeV/sr, the unit for $T_i$ is MeV.

| Part | $N_1$ | $\beta_1$ | $T_1$ | $N_2$ | $\beta_2$ | $T_2$ | $N_3$ | $\beta_3$ | $T_3$ |
|---|---|---|---|---|---|---|---|---|---|
| p | 11.93 | 0.0080 | 2.22 | 0.9173 | 0.0408 | 10.42 | 1.158 | 0.2450 | 13.31 |
| d | 0.6711 | 0.0087 | 4.01 | 0.2351 | 0.0898 | 12.81 | 0.2556 | 0.2688 | 16.03 |
| t | 0.1843 | 0.0085 | 4.71 | 0.0886 | 0.0761 | 11.49 | 0.03997 | 0.2126 | 15.65 |
| $^3$He | 0.03607 | 0.0324 | 7.90 | 0.03273 | 0.1611 | 16.09 | 0.2075 | 0.3801 | 17.69 |
| $^4$He | 3.292 | 0.0112 | 3.14 | 0.2474 | 0.0534 | 9.01 | 0.03557 | 0.1578 | 15.58 |
| $^6$Li | 0.008834 | 0.0139 | 3.28 | 0.003927 | 0.0569 | 10.24 | 0.001068 | 0.1455 | 11.13 |

and $Y_2(p_2)$ (shown in Figure 4.1).

$$1 + R(q) = C_{12} \frac{\Sigma Y_{12}(p_1, p_2)}{\Sigma Y_1(p_1) Y_2(p_2)} \tag{4.2}$$

Here, $p_1$ and $p_2$ are the momenta of the two particles in the laboratory and $q = \mid \mu(v_1 - v_2) \mid$ is the relative momentum between the two particles. For each experimental gating condition, the sums on Equation 4.2 are extended over all energy, position and detector combinations corresponding to specific relative momentum bins. The normalization constant $C_{12}$ in Equation 4.2 is chosen so that R(q) vanishes at large relative momenta where final state interactions between the two particles become negligible.

As illustrated by proton inclusive cross sections (see Figure 4.1), many different mechanisms contribute to proton emission. The low energy protons (E < 16 MeV) are due to the evaporation from equilibrated or nearly equilibrated target residues. At high energies (E > 30 MeV), the proton spectrum shows more energetic contributions from pre-equilibrium emission and projectile break up. These non-equilibrium processes become less important with increasing angle. In terms of the space and time evolution of the system, pre-equilibrium proton emission should correspond to a short lived spatially localized region which corresponds initially to the overlap of the two colliding nuclei. The proton emission from the equilibrated target like residue should correspond to a larger and/or longer lived source. The complete space-time should display an evolution between these two extremes, with pre-equilibrium emission mechanism most important for higher energy protons and equilibrium mechanism most important for low energy protons.

The energy gated proton-proton correlation function is shown in Figure 4.4; the different energy gates contain different portions of equilibrium and non-equilibrium emission. Consistent with previous measurements [Boal 90b, Lync 83, Chen 87b], the

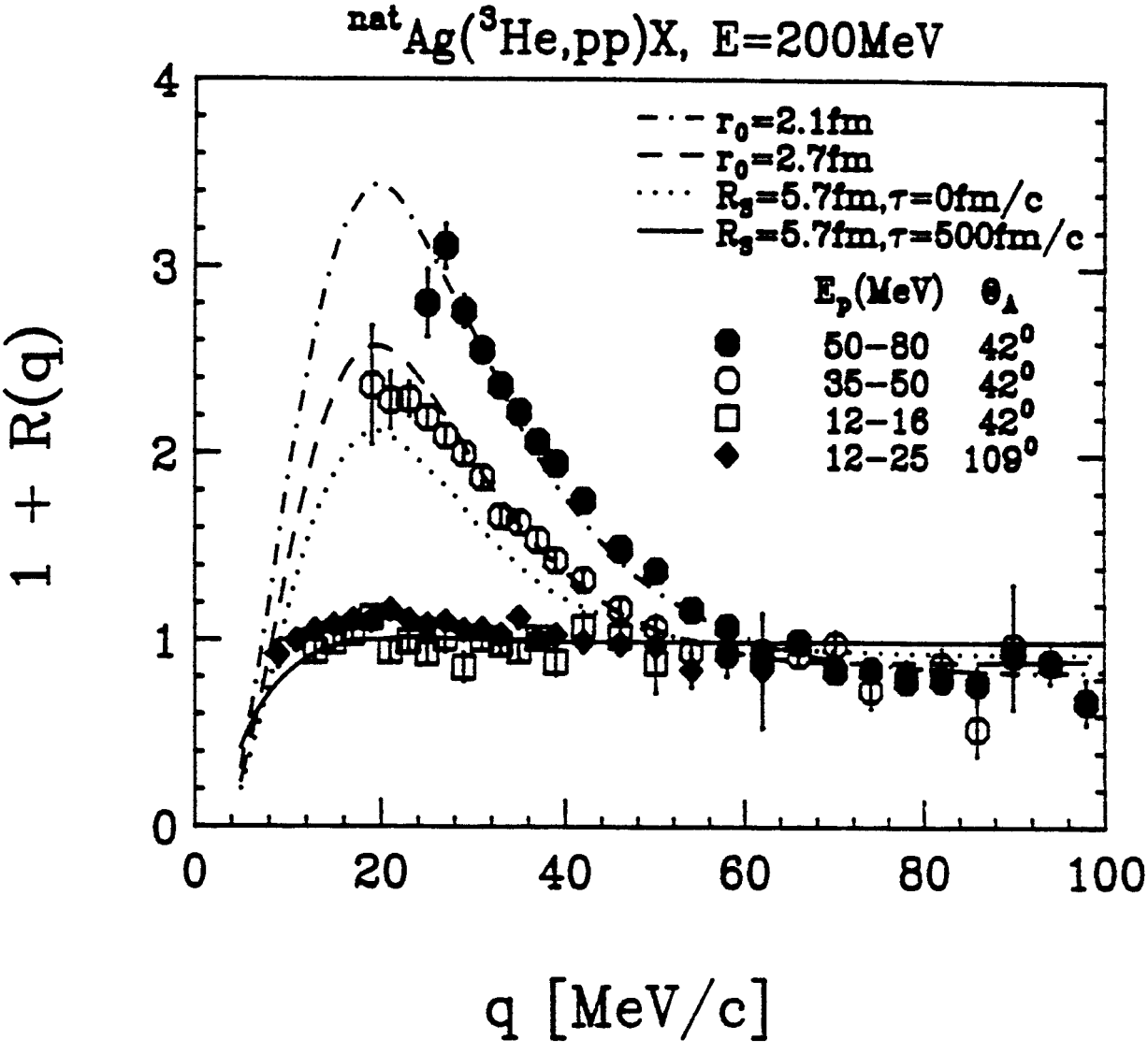


Figure 4.4: p-p correlation functions measured for the $^3$He+Ag reactions at 200 MeV. The energy gates and the angular locations of the center of the hodoscope are indicated in the figure. The curves are discussed in the text.

correlation functions exhibit maxima at q=20 MeV/c, which is due to the attractive singlet S-wave final state interaction. For low energy protons (E = 12-16 MeV at $\Theta_A = 42^0$ and E = 12-25 MeV at $\Theta_A = 109^0$) the maxima are strongly attenuated, qualitatively consistent with an evaporative emission mechanism as suggested by the inclusive energy spectra. The maxima increase with the kinetic energy of the emitted particles, reaching values for E = 50-80 MeV which are the largest so far observed in medium energy experiments, indicating rapid emission by a small source.

With the formula developed in Chapter 3, eq. 3.10, 3.11, and 3.12, we can calculate the correlation function with any source density distribution, not only the simple Gaussian source. For illustration, the solid and dotted curves in Figure 4.4 show correlation functions calculated assuming surface emission from a Ag target-like residue ($R_s$ = 5.7 fm), with an exponential time dependence given by

$$g(p,r,t) \propto \rho_0 \frac{d^3\sigma}{dp^3}(r.p)\Theta(r.p)\delta(R_s - r)[\frac{e^{-t/\tau}}{\tau}]\Theta(t) \tag{4.3}$$

Here, $\rho_0$ is a normalization constant, R(t) is the unit step function, $\tau$ is the source lifetime, $\delta$ is the Dirac delta function, r and p are the unit vectors for position and momentum, and $d^3\sigma/dp^3$ is extrapolated from moving source fits to the single proton inclusive spectrum, shown as the dashed lines in Figure 4.1. The correlation functions for low energy protons can be reproduced with lifetimes of $\tau$ = 300 - 3000 fm/c; the solid curve shows a calculation for $\tau$ = 500 fm/c. While larger maxima at q = 20 MeV/c are predicted for smaller $\tau$, even the assumption of a vanishing source lifetime (dotted curve) underpredicts the correlation functions measured for the two highest energy gates where non-equilibrium emission dominates.

For the higher energy gated correlation functions, the non-equilibrium emission dominates, and the volume emission is more appropriate for the fitting. The dashed

and dot-dashed curves show calculations for Gaussian sources of negligible lifetime,

$$g(p,r,t) \propto \rho_0 e^{-r^2/r_0^2}\delta(t) \tag{4.4}$$

with the specific source radii $r_0$ given in the figure. The calculations illustrate that the correlation functions for the most energetic protons are consistent with instantaneous emission by a system significantly smaller than the target nucleus.

Further insight can be obtained from the comparison, in Figure 4.5 , of the gaussian source radii extracted from this experiment to radii extracted from measurements for $^{14}$N, $^{16}$O, and $^{40}$Ar projectiles incident on heavy targets at different incident energies. $^{14}$N + $^{197}$Au at E/A = 35 MeV [Chen 87b], $^{14}$N + $^{197}$Au at E/A = 75 MeV [Gong 90], $^{16}$O + $^{197}$Au at E/A = 25 MeV [Lync 83], $^{16}$O + $^{197}$Au at E/A = 94 MeV [Chen 87b], $^{40}$Ar + $^{197}$Au at E/A = 60 MeV [Poch 86]. To compare the correlations of protons emitted at comparable stages of equilibration, these radii have been plotted as functions of $V_p/V_{beam}$, the ratio of the mean velocity, $V_p$, of the detected protons to the velocity of the beam, $V_{beam}$.

For $V_p/V_{beam} > .7$, the extracted source radii for $^{14}$N projectiles (open points) decrease systematically with $V_p/V_{beam}$ ; the trend, interpolated by the solid line, is remarkably independent of the incident energy of the projectile. While the source radii for $^{16}$O projectiles closely parallels those for $^{14}$N projectiles, corresponding source radii extracted for $^{40}$Ar (solid diamonds) and $^{3}$He (solid circles) projectiles are much larger and much smaller, respectively. The dashed-dotted and dashed lines, in Figure 4.5, are obtained from the solid line by multiplying the source radii by the ratios R($^{40}$Ar)/R($^{14}$N) and R($^{3}$He)/R($^{14}$N), respectively, where R($^{40}$Ar), R($^{14}$N), and R($^{3}$He) are the radii of the $^{40}$Ar, $^{14}$N, and $^{3}$He projectiles, respectively. This agreement of extrapolated and measured source radii for $^{3}$He and $^{40}$Ar projectiles suggests that the spatial extent of the emitting region is governed initially by the overlap of these

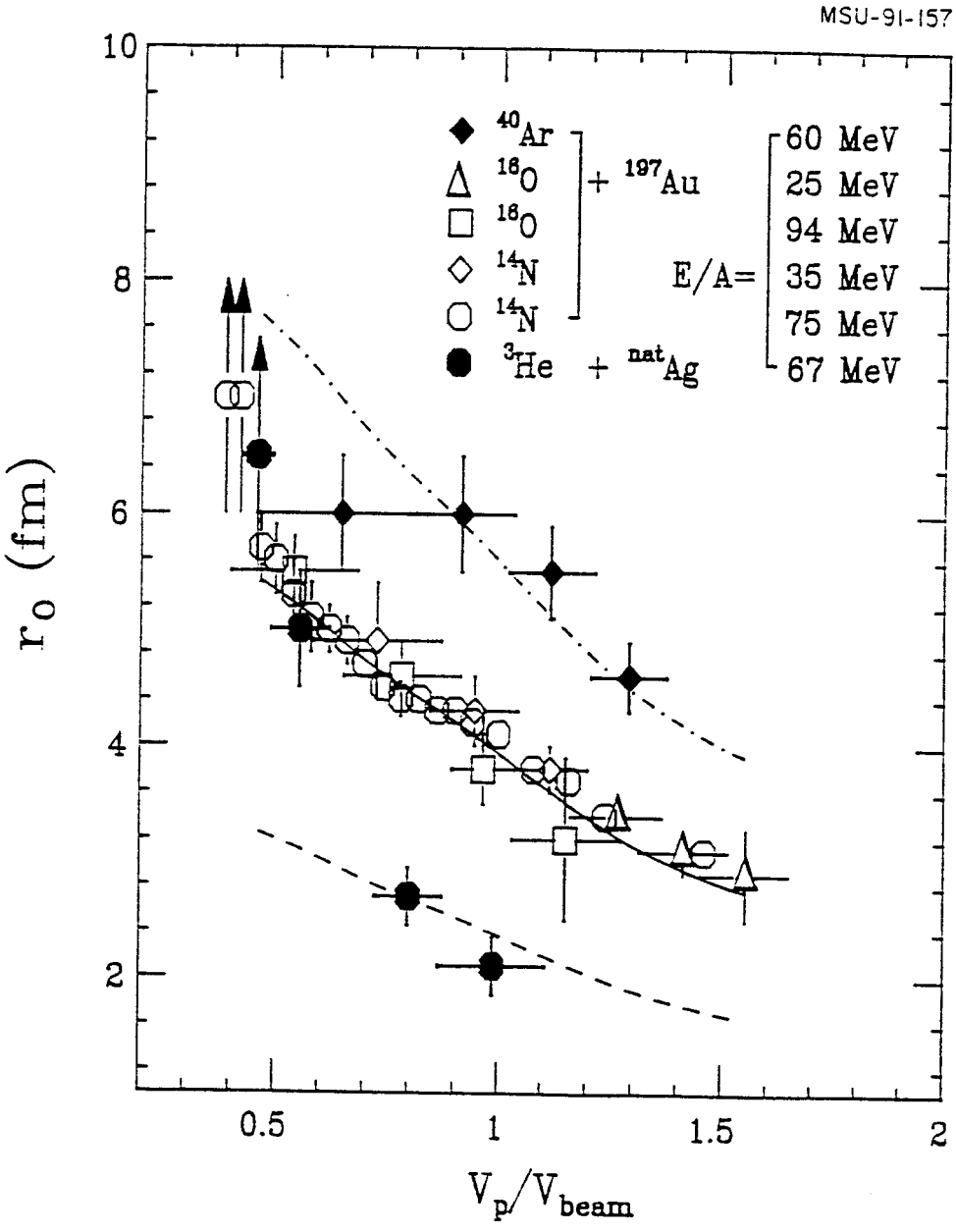


Figure 4.5: Systematics of gaussian source radii extracted for a variety of reactions. The solid and open points depict experimentally extracted source radii. The solid line is an interpolation of the source radii extracted for $^{14}$N projectiles. The dashed and dotted-dashed lines are extrapolated from the solid line via the ratio of the projectile radius to the radius of $^{14}$N.

relatively small projectiles with the heavy target. It is important to note that these simple trends, observed for $V_p/V_{beam} > .7$, would not be observed in energy averaged correlation functions, because such data primarily reflect the correlations of the more abundant low energy protons where the lifetime plays an important role and these trends are not manifest.

The correlation function measurement can be used very effectively to extract information about the space time evolution of the reaction. It also can be used to test any nuclear reaction model which makes prediction for a phase space distribution, like the Wigner function in equation 3.11. In order to determine whether the strong correlations observed in the present experiment can be reproduced by microscopic dynamical calculations, we have calculated correlation functions using Wigner transforms which satisfy the Boltzmann-Uehling-Uhlenbeck (BUU) transport equation 3.15 [Bert 84, Bert 88].

In our calculations we assumed a free nucleon-nucleon cross section and an equation of state with a compressibility coefficient K=240 MeV. Following refs. [Gong 90], nucleon emission was calculated during a time interval of $\Delta$ t =140 fm/c after the initial contact of the colliding nuclei. Further details of the numerical procedure are given in refs. [Gong 91, Baue 88].

The nucleon differential cross section, predicted by the BUU simulation is shown by the solid histogram in Figure 4.1. The calculation provides a reasonable accounting for the proton energy spectrum at high energies and forward angles, but underpredicts the data at low energies where evaporative contributions are dominant. The dashed, dot-dashed and solid curves in Figure 4.6 show correlation functions predicted by the BUU calculations. For non-equilibrium emission at low (E = 16-25 MeV) and intermediate (E =35-50 MeV) energies, the calculations are in reasonable agreement with the data. They also reproduce the trend of the correlation function,

that is, the correlation functions are bigger for more energetic particles. For the most energetic protons (E =50-80 MeV), however, the calculations underpredict the observed correlations, a discrepancy not observed in previous comparisons of heavy ion induced reactions [Gong 90]. For this energy gate, the extracted source radius was also smaller than the systematic extrapolation presented in Figure 4.5, further suggesting an enhancement in the correlation function.

As we mentioned previously, the peak at $q \approx 20$ MeV/c is from the spin singlet state of the proton-proton wavefunction. Since the relative wavefunction of the two protons in the $^3He$ nucleus are in a spin singlet state ($^1S$), there is a possibility that this large peak may arise from breakup residues. To explore whether this discrepancy may be a remnant of the spin correlation in the $^3$He ground state, we varied the relative weighting of the singlet and triplet states in the p-p relative wave function in Equation 3.10 according to

$$\mid \phi(q,r) \mid^2 = \alpha \mid \phi_s(q,r) \mid^2 + (1-\alpha) \mid \phi_t(q,r) \mid^2 \tag{4.5}$$

where $\alpha$ is a weighting factor and $\phi_s$(q,r) and $\phi_t$(q,r) are the singlet and triplet spatial wavefunctions. Setting $\alpha = 1/4$ selects the standard statistical weighting adopted for all calculations but those depicted by the dotted lines in Figure 4.6. Choosing $\alpha =$ 0.45 raises the correlation function to values depicted by the dotted line in Figure 4.6, comparable to the measured one. This value of $\alpha$ is consistent with the assumption that about 27% of the proton pairs in the highest energy gate originated in the $^3$He projectile break up and propagated to the detectors with their initial spin correlations undisturbed. Since the peak of the correlation function is caused only by the spin singlet wavefunction, it gives rise to a larger correlation function.

To summarize this section, two-proton correlation functions measured for $^3$He induced reactions on Ag at $E_{beam}$ = 200 MeV increase dramatically with the energy

of the detected protons. Combined with other correlation function data, these measurements suggest that the spatial extent of the emitting region is governed initially by the overlap of the projectile with the target. For proton energies less than 50 MeV, the measured trends are consistent with those predicted by the Boltzmann-Uehling-Uhlenbeck equation. This suggests that the localization in spacetime of the emission of protons with these energies is reasonably well described by the model. The correlation functions of more energetic protons are underpredicted by the model, an effect which may reflect remnant spin correlations from the ground state of the $^3$He projectile.

## 4.3 The non-identical particle correlation functions

The proton-proton correlation function technique is based on its sensitivity to spatial localization through final state interactions between the two emitted protons. This method can be extended to pairs of particles which have a strong attractive final state interaction which causes the correlation function to deviate significantly from zero. Deuteron-alpha particle correlation functions have likewise been shown to be sensitive to the space-time localization of the emitting source by Boal et al. [Boal 86]. While the interaction between $d-\alpha$ pairs is more complicated than for p-p pairs, It can be parameterized as a sum of Woods-Saxon potentials acting on each partial wave, with the parameters listed in Table 4.2.

The measured deuteron-alpha correlation function at forward angles ($\Theta_A = 42^0$) is shown in figure 4.7. The sharp peak at $q \approx 40$ MeV/c in the correlation function is from the 2.186 MeV resonance of $^6Li^*$ ($\Gamma = 24$ KeV, $J^\pi = 3^+$, $\Gamma_\alpha/\Gamma = 1.0$). The broad peak at $q \approx 80$ MeV/c is from the overlap of resonances at 4.31 MeV ($\Gamma = 1.7$ MeV, $J^\pi = 2^+$, $\Gamma_\alpha/\Gamma = 0.97$), and 5.65 MeV ($\Gamma = 1.5$ MeV, $J^\pi = 1^+$, $\Gamma_\alpha/\Gamma = 0.74$).

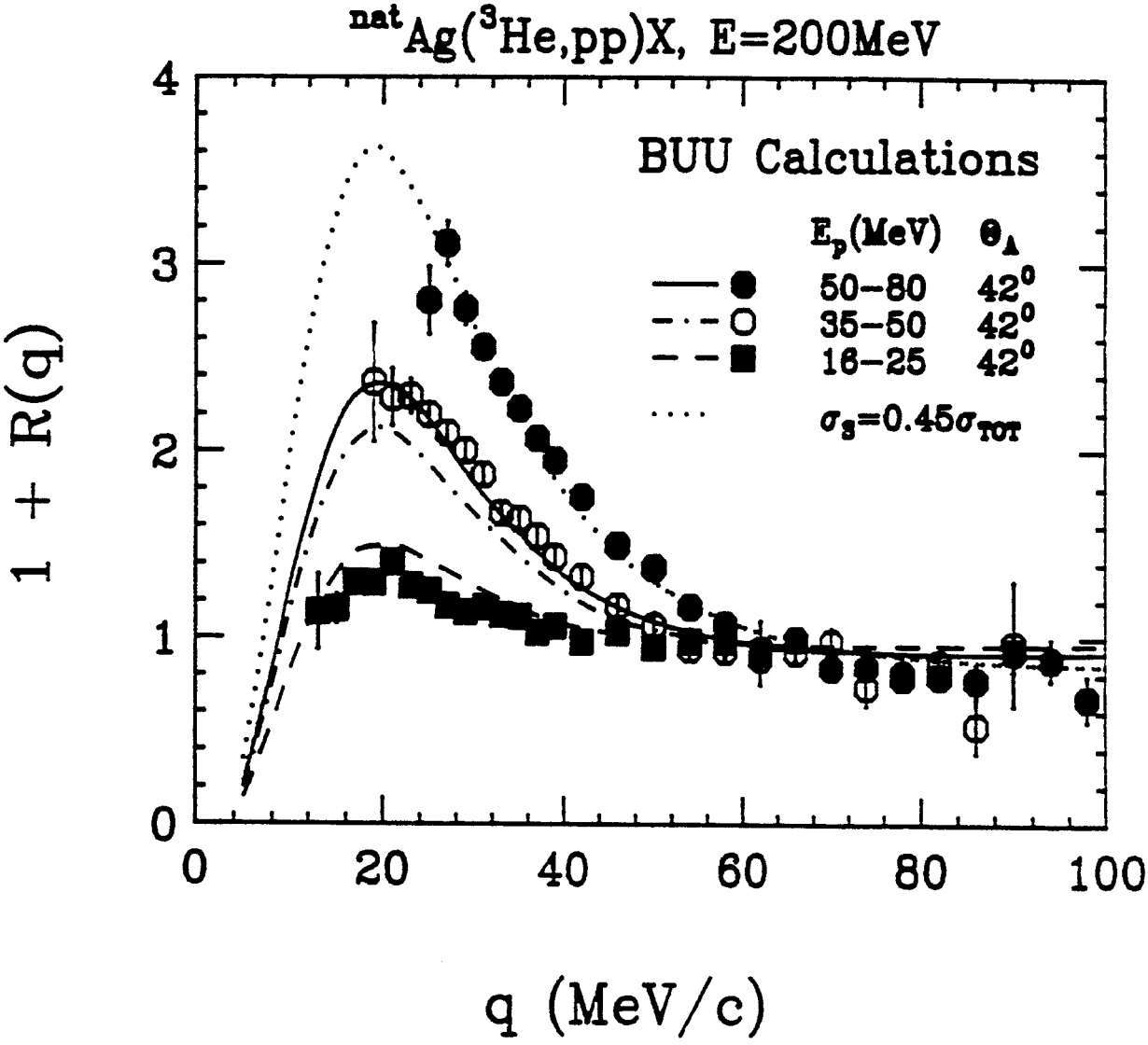


Figure 4.6: Comparison of experimental p-p correlation functions with predictions of the BUU theory for the $^3$He+Ag reaction at 200 MeV. The dotted curve is discussed in the text.

Table 4.2: The Woods-Saxon potential parameters used in the calculation of d + $\alpha$ correlation functions. They are obtained from the analysis of the d + $\alpha$ phase shift data. A negative sign indicates an attractive potential [Boal 86].

| i | j | $V_0$ (MeV) | R (fm) | a (fm) |
|---|---|---|---|---|
| 0 | 0 | -5.82 | 3.8767 | 0.1963 |
| 1 | 0 | 0.3586 | 5.57 | 0.55 |
| 1 | 1 | 0.749 | 4.14 | 0.566 |
| 1 | 2 | 1.147 | 3.848 | 0.551 |
| 2 | 1 | -11.3646 | 4.1823 | 0.4712 |
| 2 | 2 | -31.0 | 2.916 | 0.6386 |
| 2 | 3 | -42.045 | 2.7648 | 0.70 |

Because the width of the resonance peak at $q \approx 40$ MeV/c is too narrow for the resolution of our hodoscope, the theoretical calculation of the correlation function is folded with the resolution of the hodoscope to fit the peak of the correlation function, under the condition that $R_{eff} = \int dq R(q)$ is conserved [Chen 87b]. The integration includes the peak region at 30 MeV/c < q < 60 MeV/c. This latter procedure is less sensitive to the uncertainty of the exact experimental line shape. For a Gaussian source of negligible lifetime, the extracted source size is 2.5fm. To contrast $d-\alpha$ correlation function at forward angles with that observed at backward angles, the correlation function at backward angles ($\Theta_A = 109^0$) is shown in figure 4.8. The magnitude of the peak is smaller than that of the forward angles, corresponding to a larger size and/or longer lifetime of the source. This trend is qualitatively consistent with the proton-proton correlation function measurement. The extracted source radii from $d-\alpha$ correlation functions, however, are consistently smaller than that from p-p correlation functions [Chen 87b].

It is interesting to try to construct a systematics for the extracted source sizes from d-$\alpha$ correlation functions to see if it also has a scaling relationship like the one for p-p correlation functions shown in Figure 4.5. Figure 4.9 shows the gaussian source radii extracted from d-$\alpha$ correlation functions as a function of $V_p/V_{beam}$ for this experiment and the following experiments, $^{14}$N + $^{197}$Au at E/A = 35 MeV [Chen 87b], $^{16}$O + $^{197}$Au at E/A = 94 MeV [Chen 87b], and $^{40}$Ar + $^{197}$Au at E/A = 60 MeV [Poch 86]. The experimental data follow a systematic trend similar to that shown in Figure 4.5. The solid and dashed lines are, in fact, directly taken from Figure 4.5 and multiplied by a factor of 0.7. This scaling factor may reflect the fact that the mean free paths for deuterons and alpha particles in the nuclear medium are somewhat shorter than the mean free path for protons. So the effective source volume is somewhat smaller. The data points follow the scaling line quite nicely, even at small $V_p/V_{beam}$, in contrast to

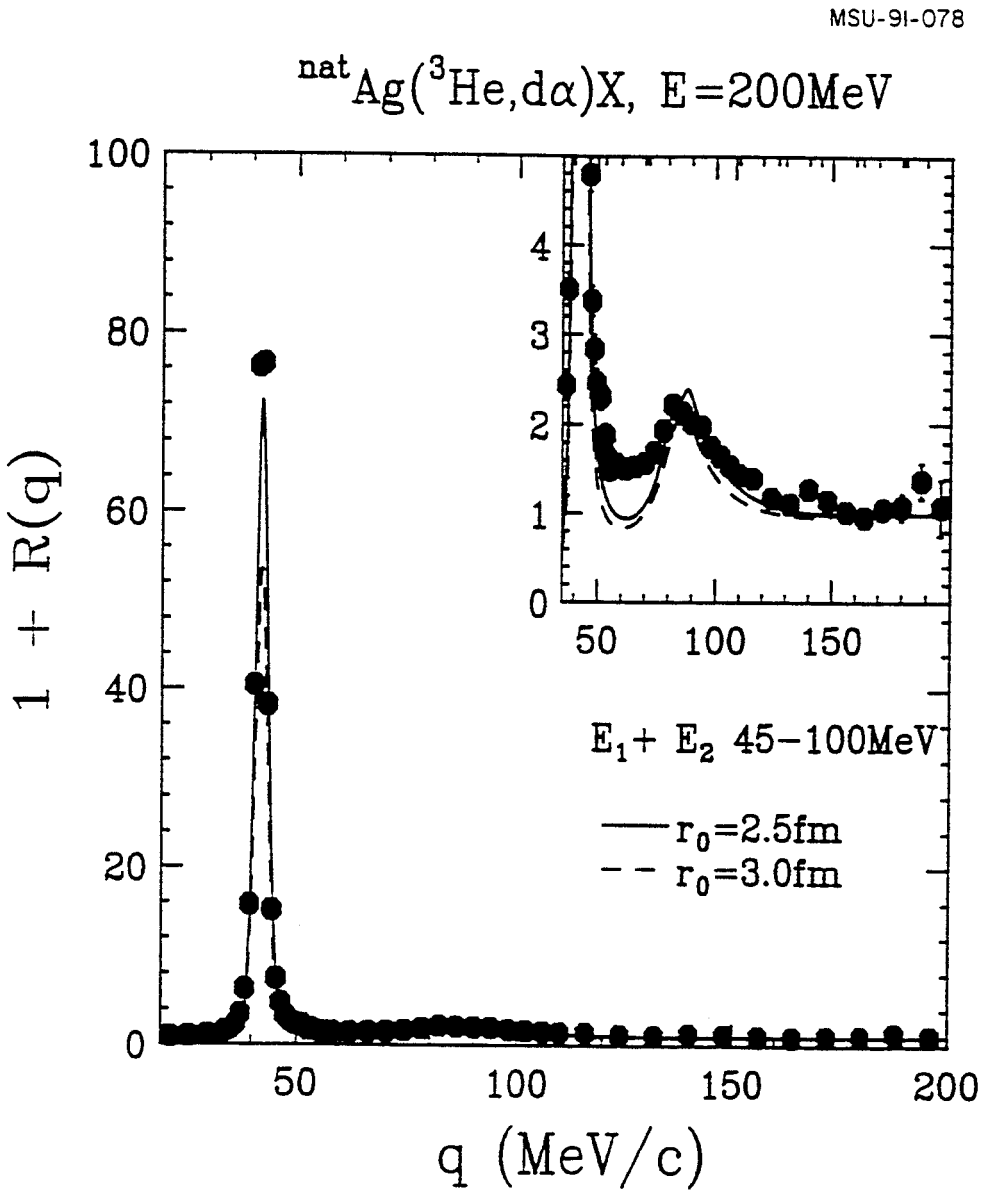


Figure 4.7: The d-$\alpha$ correlation functions with the Gaussian source fitting parameter for the $^3$He+Ag reaction at 200 MeV. The hodoscope centered at $\Theta_A = 42^0$

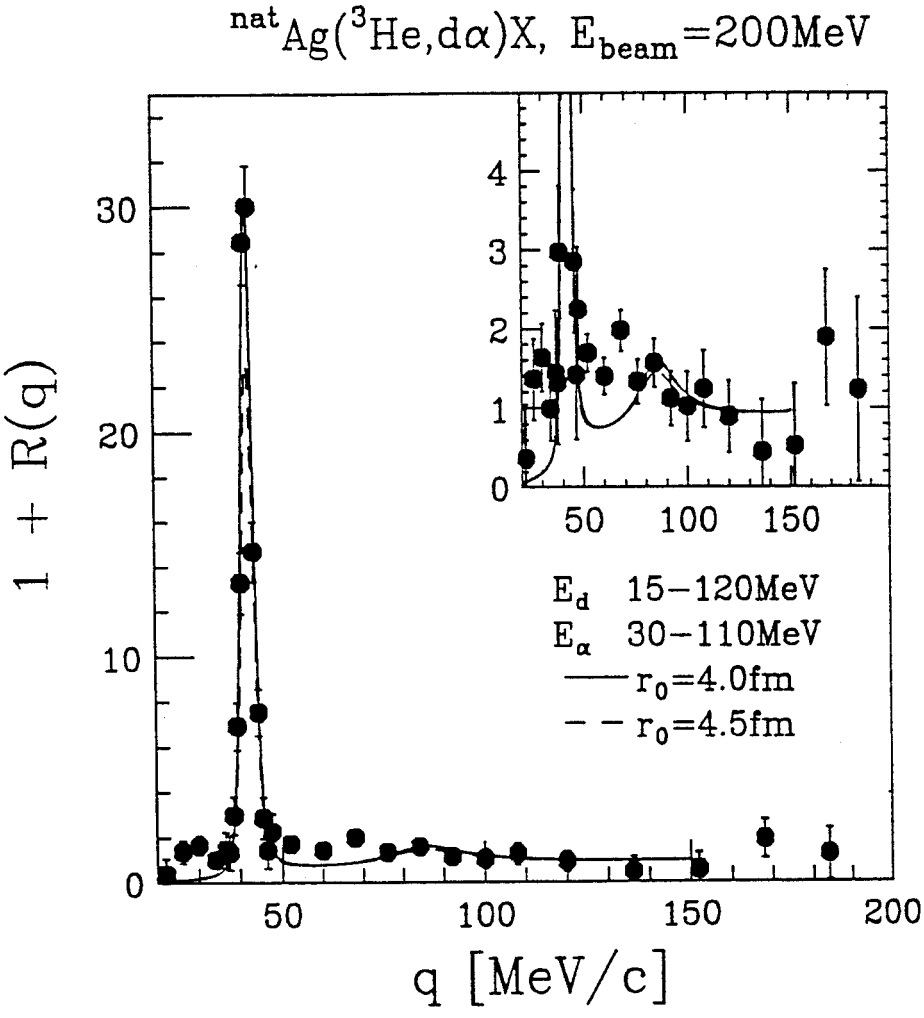


Figure 4.8: The d-$\alpha$ correlation functions with the Gaussian source fitting parameter for the $^3$He+Ag reaction at 200 MeV. The hodoscope centered at $\Theta_A = 109^0$

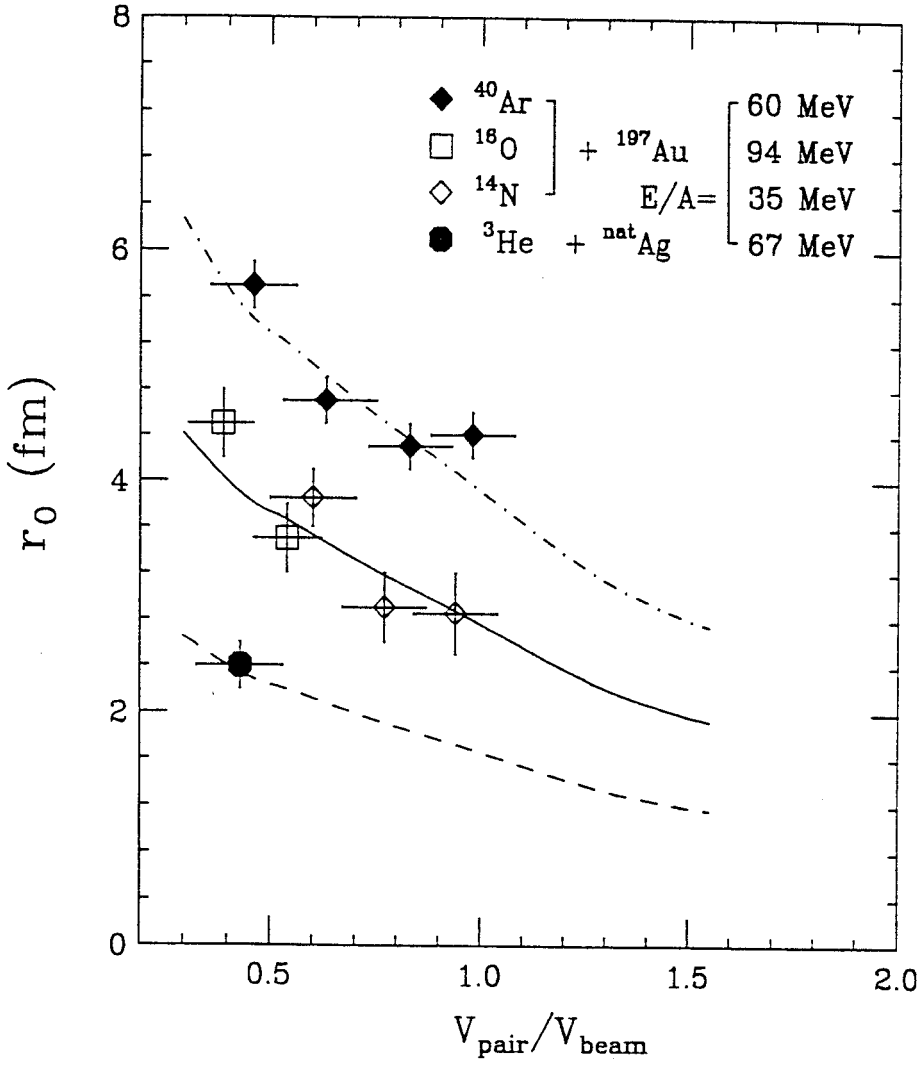


Figure 4.9: Systematics of gaussian source radii extracted from d-$\alpha$ correlation functions for a variety of reactions. The solid and open points depict experimentally extracted source radii. The solid and dashed lines are from the corresponding lines in Figure 4.5 with a scaling factor 0.7.

the p-p correlation systematics, where some of the data at small $V_p/V_{beam}$ deviates significantly from the scaling trend. This may reflect the fact that the contributions to the deuteron spectra from target like compound nuclear evaporation are smaller than for protons.

## 4.4 The excited state population measurement

The $^5$Li and $^6$Li unbound excited state populations were measured in this experiment, and used to deduce the emission temperature of the fragmenting system at breakup.

$$^5Li \rightarrow p + \alpha$$

The ground state of $^5$Li is unstable with respect to decay into a proton and an alpha particle, $^5Li \rightarrow p + \alpha$. Protons and $\alpha$ particles were measured in coincidence during the experiment and the resultant $p - \alpha$ correlation function is shown in Figure 4.10. We have chosen to present the data for these lighter system in the form of correlation functions because it is easier to view the background in such plots. The broad peak at $E_{rel} \approx 2$ MeV in the correlation function is from the decay of the $^5Li$ ground state with spectroscopic parameters $J^\pi = \frac{3}{2}^-, \Gamma = 1.5$ MeV, $\Gamma_p/\Gamma = 1.0$. At even lower relative energies, there is a small rise in the correlation function, which may be due to the decays from $^9B$ in their ground states. $^9B_{g.s} \rightarrow p +^8 Be_{g.s} \rightarrow p + \alpha + \alpha$ [Naya 92]. To accommodate this process, we included an extra Breit-Wigner resonance term with decay width $\Gamma = 0.055$ MeV at $E_{rel} \approx 0.19$ MeV in the overall fitting. Because the state at $E_{rel} \approx 2$ MeV is very broad, one must consider the modification of the resonance line shape due to the Boltzman factor $exp(-E/T)$ with T = 4 MeV. This, however, does not influence significantly the extraction of the emission temperature. The best fit to the spectra is shown as the solid line in the figure. The major source of uncertainty comes from the systematic uncertainty in the background estimation. The

two dashed lines shows the upper and lower extremes of the estimated background, the background for the best fit lies in between these two dashed lines. Since there is no stable $^5Li$ ground state, the measured energy spectrum for stable $^6Li$ nuclei was used for the efficiency calculation [Chen 88]. The extracted population probability is thus relative to the $^6Li$ ground state and has no meaning by itself. It becomes meaningful when it compared with the population probability for $^5Li$ excited state at $E^* = 16.66$ MeV. The comparison allows one to extract temperature for $^5Li$ nuclei, removing most of the uncertainty in the efficiency calculation due to the lack of a measured energy spectrum for $^5Li$ nuclei.

$$^5Li \rightarrow d + {}^3He$$

The excited state of $^5$Li nuclei at 16.66 MeV decays to a deuteron and a $^3$He nucleus. The correlation function of $d+^3He$ is shown in Figure 4.11 for data taken at $\Theta_{av} = 42^0$. The peak near the threshold is from the decay of 16.66 MeV excited state of $^5Li$ with spectroscopic parameters $J^\pi = \frac{3}{2}^+, \Gamma = 0.20$ MeV, $\Gamma_d/\Gamma = 1.0$. The R-matrix formula was used to fit the excited state and extract the population probability. The resonance parameters are, $E_\lambda = 129$ KeV, $\gamma^2(d) = 780$ KeV, $l_d = 0, a_d = 7$ fm, $\gamma^2(p) = 12$ KeV, $l_p = 2, a_p = 7$ fm, with boundary condition parameters $B_d = B_\alpha = 0$. Another wide excited state at $E^* = 20$ MeV were also included in the fit, but not analyzed further. Because the $d$ and $^3He$ have different charge to mass ratios, they experience different Coulomb accelerations from the residue. The relative energy spectrum is thus distorted [Poch 86]. The resonance energy shift of 100 KeV is applied to fit the data. The $^6Li$ ground state is used for the efficiency calculation, and extracted population must be compared with the population of the ground state of $^5$Li to extract the temperature. An apparent temperature of T = 4.03 $\pm$ 0.17 MeV, from $^5$Li excited states is obtained by comparison to Equation 3.27 without corrections for sequential

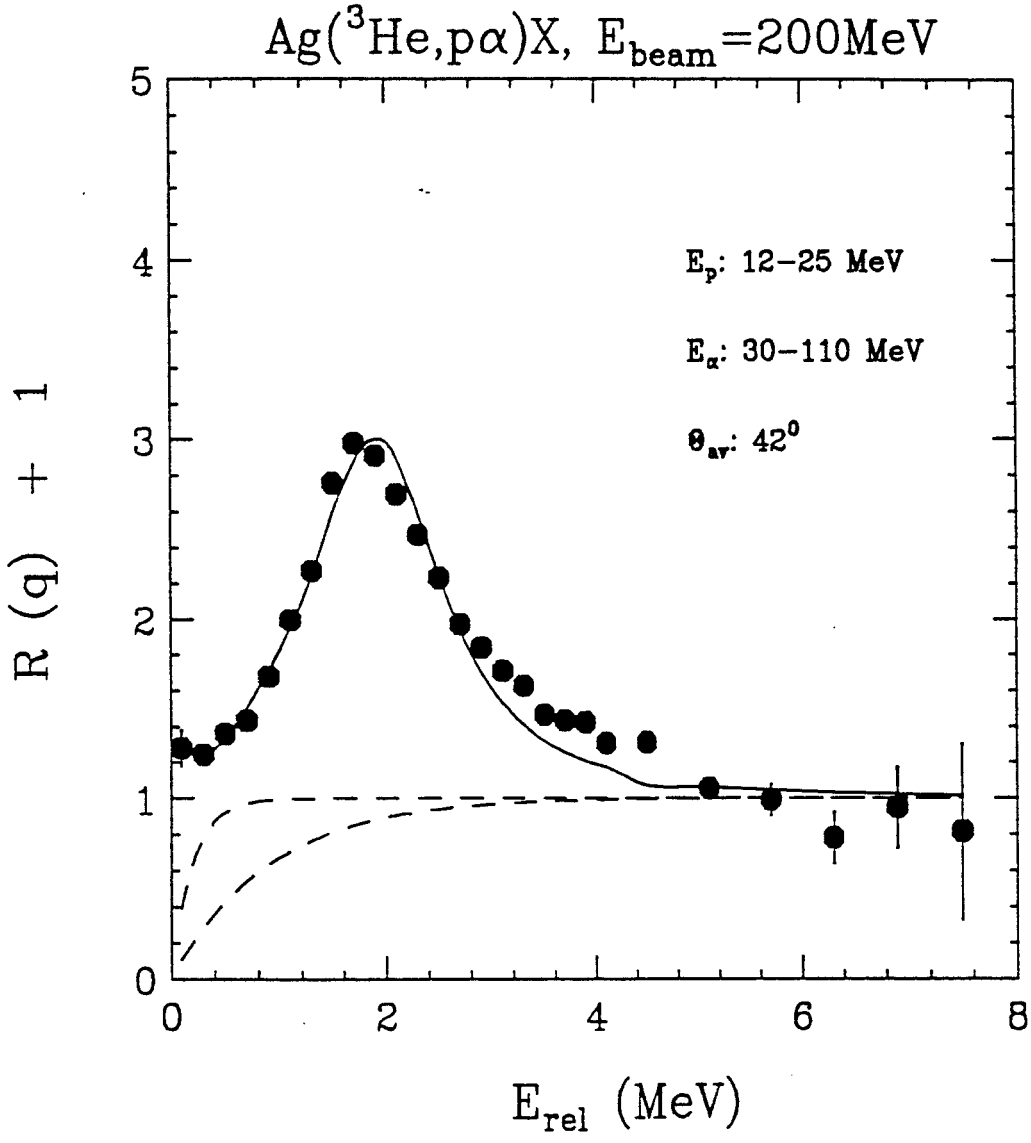


Figure 4.10: The $p-\alpha$ correlation function measured in the $^3$He + Ag reaction at $E_{beam}$ = 200 MeV at $\Theta_{av} = 42^0$. The solid lines depict the best fit to the data, and the dashed lines depict extreme assumptions about the background used to estimate the systematic uncertainties due to background subtraction.

feeding. Comparison with sequential decay calculations are discussed in the later part of this chapter.

### $^6Li \rightarrow d + \alpha$

The $d - \alpha$ correlation function was measured in the experiment and is shown in Figure 4.12 for data taken at $\Theta_{ac} = 42^0$. The narrow peak at $E_{rel} \approx 0.71$ MeV is from the decay of the $^6Li$ excited state at $E^* = 2.186$ MeV with spectroscopic parameters $J^\pi = 3^+, \Gamma = 0.024$ MeV, $\Gamma_c/\Gamma = 1.0$. Also included in the fit is the broad peak at $E \approx 3$ MeV, which is from the overlap of two resonances at 4.31 MeV ($\Gamma = 1.7$ MeV, $J^\pi = 2^+$, $\Gamma_\alpha/\Gamma = 0.97$), and 5.65 MeV ($\Gamma = 1.5$ MeV, $J^\pi = 1^+$, $\Gamma_\alpha/\Gamma = 0.74$). The solid line depicts the best fit to the data using the Breit-Wigner formalism. The two dashed lines indicate two extreme assumptions for the background which are used to estimate the systematic uncertainty in the fit. The energy spectrum for stable $^6Li$ nuclei are used as input to the efficiency calculation and the population probability is given with respect to the observed particle stable yield and was used to extract an apparent temperature. Apparent temperatures of T = 2.86 ± 0.37 MeV, T = 3.94 ± 0.55 MeV, and T = 5.86 ± 1.83 MeV, were obtained by comparing Equation 3.27 to the ratios of populations of the $^+3$ excited state over the ground state, the $^+2$ plus $^+1$ excited states over the ground state, and the $^+2$ plus $^+1$ excited states over the $^+3$ excited state respectively, without corrections for sequential feeding. Comparison with sequential decay calculations are discussed by the end of this chapter.

### $^6Li \rightarrow d + \alpha$ at backward angles

The $d - \alpha$ correlation function is shown in Figure 4.13 for data taken at the backward angle setting at $\Theta_{av} = 109^0$. The solid line is the best fit to the data assuming a Breit-Wigner line shape. The two dashed lines indicated two extremes

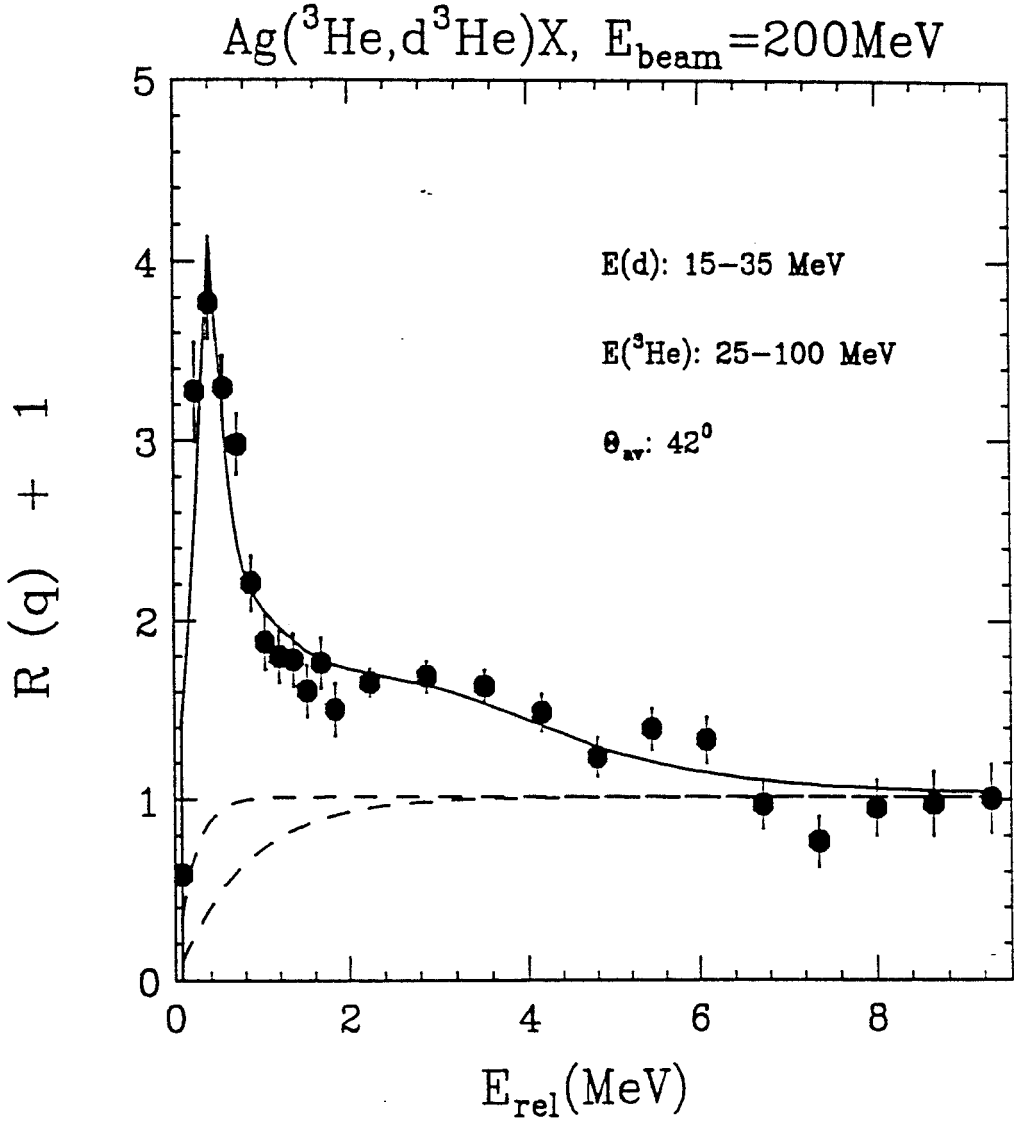


Figure 4.11: The $d-^3He$ correlation function measured in the $^3$He + Ag reaction at $E_{beam}$ = 200 MeV at $\Theta_{av} = 42^0$. The solid lines depict the best fit to the data, and the dashed lines depict extreme assumptions about the background used to estimate the systematic uncertainties due to background subtraction.

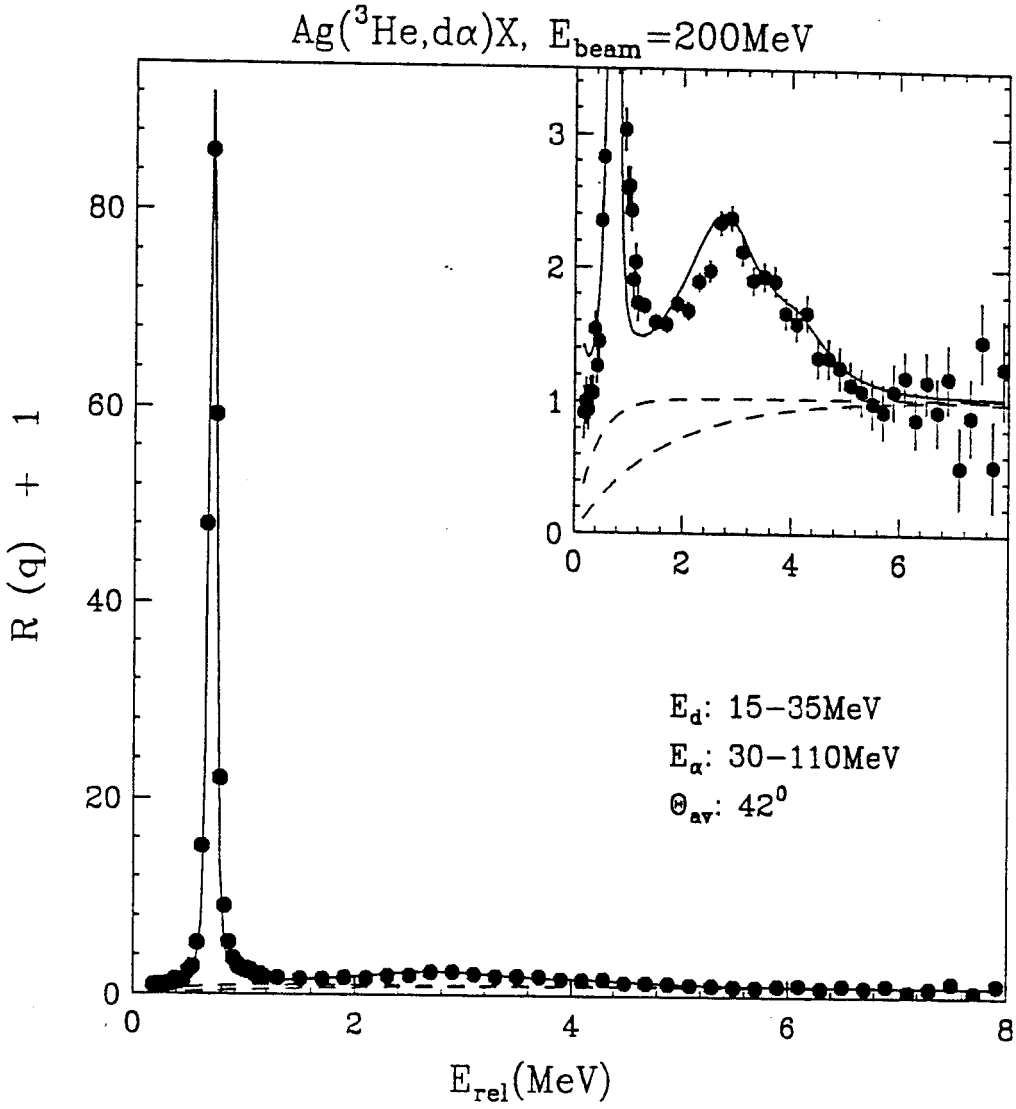


Figure 4.12: The $d-\alpha$ correlation function measured in the $^3$He + Ag reaction at $E_{beam}$ = 200 MeV at $\Theta_{av} = 42^0$. The solid lines depict the best fit to the data, and the dashed lines depict extreme assumptions about the background used to estimate the systematic uncertainties due to background subtraction.

in the background used to assess the systematic uncertainties due to the background subtraction. The best fit background lies in between these two extremes. A quite low apparent temperature of T = 0.93 ± 0.042 MeV is obtained by comparison to Equation 3.27 without corrections for sequential feeding. Comparison with sequential decay calculations are discussed by the end of this chapter. It is not possible to analyze the populations of the higher lying excited states at $E^*$ = 4.31 and 5.65 MeV due to limited statistics.

Apparent temperatures extracted from $^5Li$ and $^6Li$ excited state population probabilities without correction for sequential decay are indicated by the solid points in Figure 4.14. Some modifications of population probabilities and apparent temperatures are expected due to the sequential feeding of states by heavier particle unstable fragments. In the upper part of Figure 4.14, we plot the prediction of the sequential decay calculations of the apparent temperature for an initial temperature of T = 4 MeV as the open points. The error bars here corresponds to a range of calculated values due to uncertainties in the unknown spins, parities of excited states included in the calculation. The solid points are experimental measurements with the hodoscope at forward angle setting ($\Theta_{av} = 42^0$). The difference between the data and calculation is small for $^5$Li excited states because of the large energy gap between the two excited states, where it is less influenced by sequential decay from higher lying states [Poch 86]. On the other hand, the influence of the sequential feeding effect is big for $^6$Li nuclei, where the energy gaps are smaller. In the bottom part of Figure 4.14, the solid point is experimental measurement with the hodoscope at backward angle setting ($\Theta_{av} = 109^0$). The extracted apparent temperature is very low. The open point represents the sequential decay calculation with an initial temperature of T = 1 MeV. At this low temperature, the sequential feeding effect is small because the higher lying states have small probabilities to be populated.

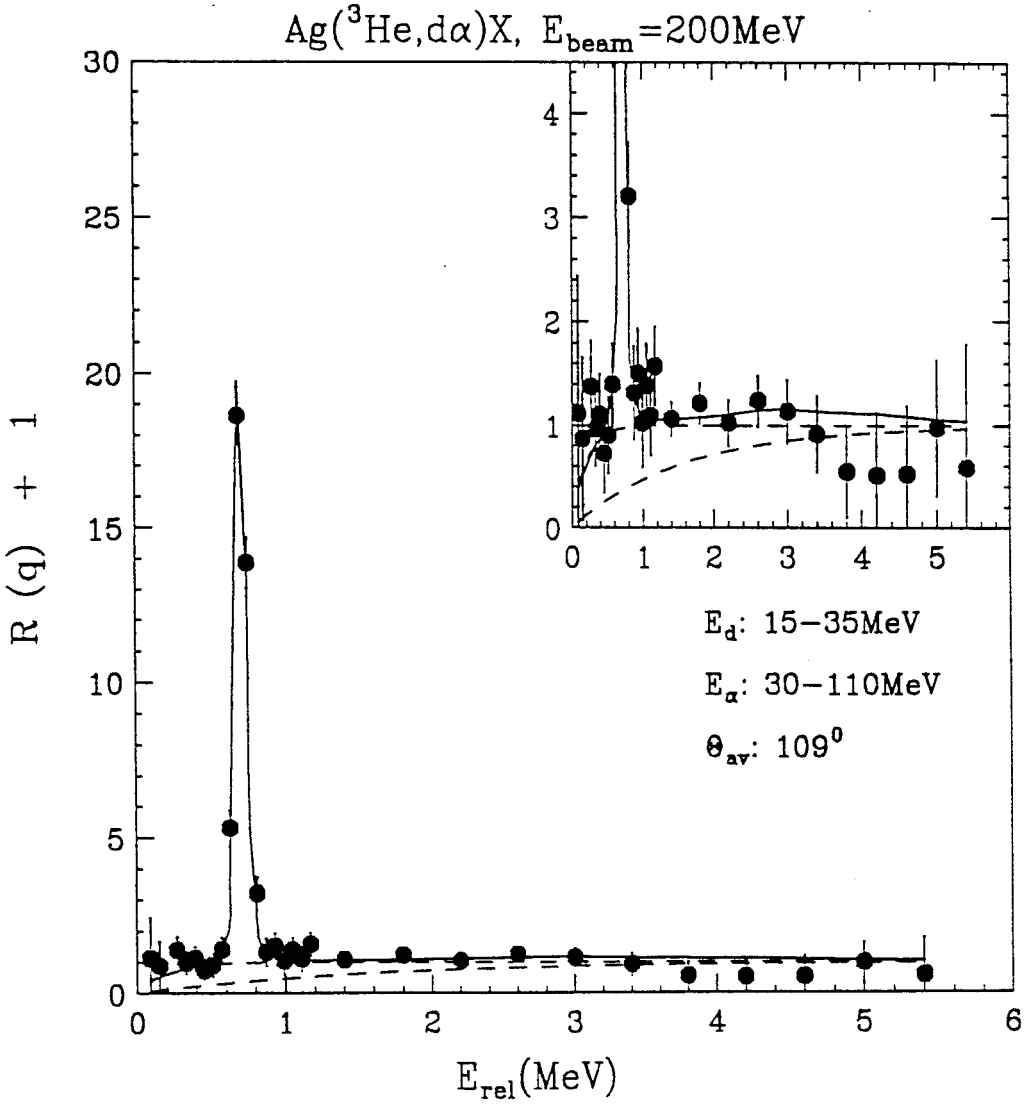


Figure 4.13: The $d-\alpha$ correlation function measured in the $^3$He + Ag reaction at $E_{beam}$ = 200 MeV at $\Theta_{av} = 109^0$. The solid lines depict the best fit to the data, and the dashed lines depict extreme assumptions about the background used to estimate the systematic uncertainties due to background subtraction.

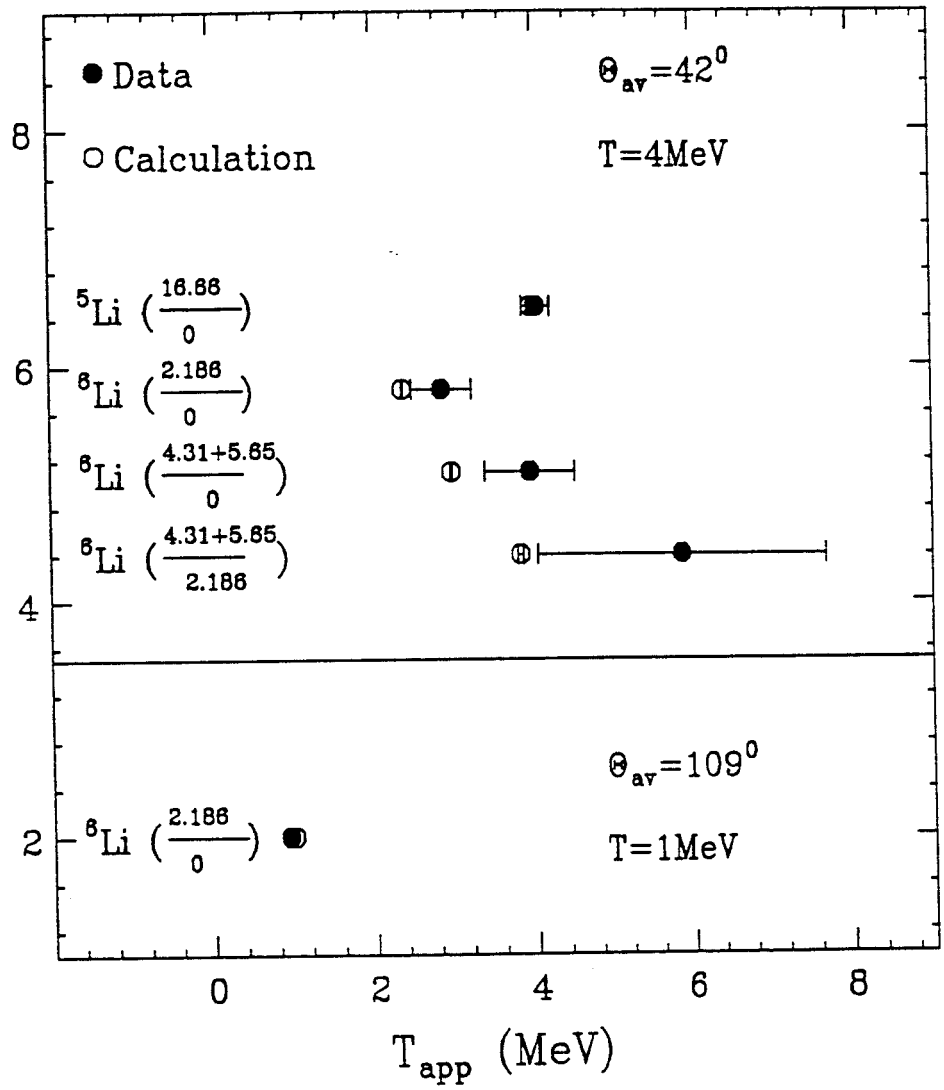


Figure 4.14: The compilation of extracted apparent temperatures of $^6$Li and $^5$Li nuclei in the $^3$He + Ag reaction at $E_{beam}$ = 200 MeV. The solid points are experimental measurements and the open points are the results of sequential decay calculations. The top panel shows the forward angle ($\Theta_{av} = 42^0$) measurements along with sequential decay calculations for an initial temperature of T = 4 MeV. The bottom panel shows the backward angle ($\Theta_{av} = 109^0$) measurements along with sequential decay calculations for an initial temperature of T = 1 MeV.

To try to understand this very low temperature at backward angles, in Figure 4.15, we compare the extracted temperature for backward angles (shaded area) with a quasiparticle dynamics (QPD) calculations (solid points) [Boal 88a]. In QPD simulation model, the Hamiltonian includes both Coulomb and isospin-dependent terms, and incorporates the Pauli antisymmetrization effects through a momentum-dependent potential. Gaussian wave packets with a fixed width parameter are used for single particle states, and the evolution of the system of nucleons are represented by a collection of quasiparticles obeying classical equation of motion. Most important for our concerns, the nuclei produced from this simulation have stable and well defined ground states, the binding energies per nucleon are close to the measured values over a wide mass range. The excitation energies of nuclei produced in a simulation are thus well defined.

In our calculation for $^3He$ + Ag reaction at $E_{beam}$=200MeV using the QPD simulation model, we calculate the most probable residue with a mass of A=108 and a charge of Z=47. We evaluate the excitation energy of this residue after an elapsed time of t=90fm/c, when the potential energy of the system has a minimum. From BUU calculations, this corresponds to a maximum in the thermal excitation energy [Xu 92]. At this time, the angular momentum of the residue is calculated and the rotational energy of the residue is subtracted from the excitation energy. This reduces the mean residue excitation at $b \approx 1$ from $E^*/A \approx 0.783 MeV$ to $E^*/A \approx 0.778 MeV$. After the emission of $^6Li$ fragment, the excitation energy of the residue with A=102 and Z=43 fragment is reduced by the kinetic energy release and $^6Li$ separation energy. This reduces the excitation energy from $E^*/A \approx 0.778 MeV$ to $E^*/A \approx 0.111 MeV$. The temperature of the final residue can be calculated from

$$T = \sqrt{E^*/a} \tag{4.6}$$

with $a = A/8$.

In Figure 4.15, the solid points represent the extracted residue temperatures calculated from the QPD simulations as a function of impact parameter. In central collisions, the projectile deposits enough excitation energy into the residue which has a temperature in agreement with the measurement. At large impact parameters, the temperatures decrease because the projectile deposit less excitation energy into the residue. Clearly, the low temperature observed experimentally is not inconsistent with the predictions of quasiparticle dynamics model.

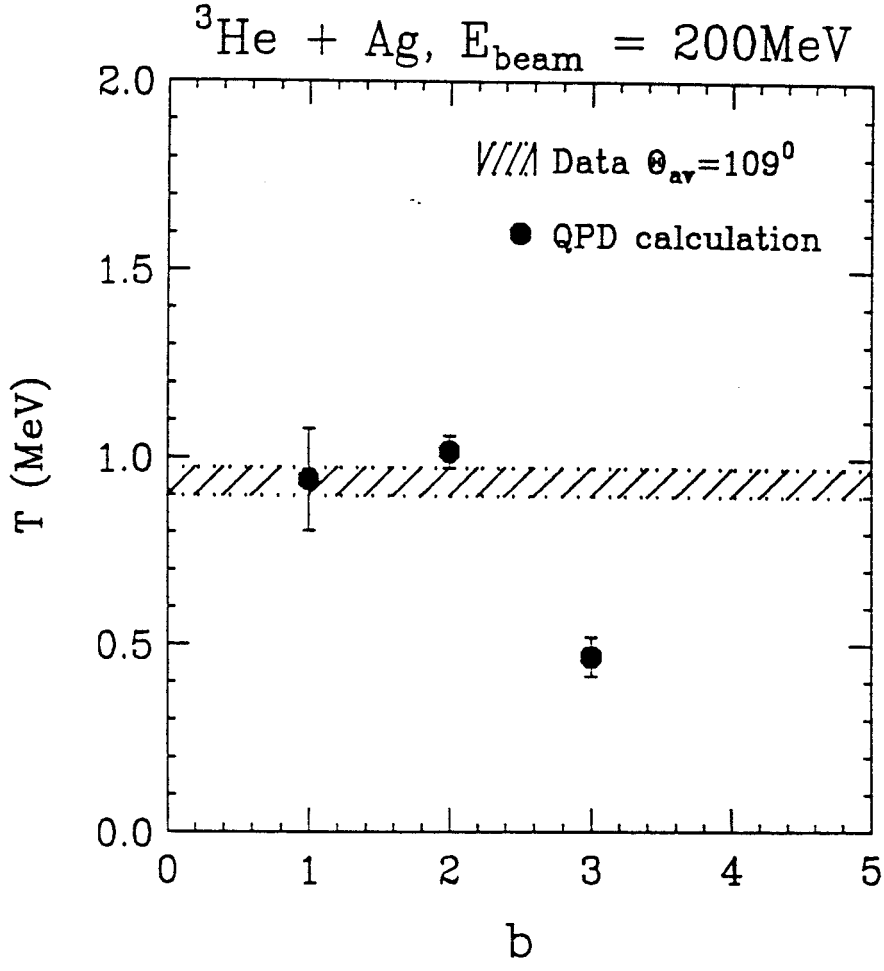


Figure 4.15: The comparison of extracted apparent temperatures of $^6$Li nuclei in the $^3$He + Ag reaction at backward angles ($\Theta_{av}$ = 109$^0$) with the QPD calculations. Solid points are the QPD calculations with different impact parameters. Shaded area represent the temperature with its uncertainty extracted from $^6$Li excited state population.

# Chapter 5

# $^{36}$Ar + $^{197}$Au reaction at E/A = 35 MeV

In energetic nucleus-nucleus collisions, very hot and dilute nuclear systems can be created which decay on time scales commensurate with nuclear relaxation times, see [Gelb 87, Sura 89, Guer 89, Cser 86, Lync 87]. These transient excitations offer singular opportunities for determining the statistical properties of hot nuclei [Sura 89, Guer 89] and hot nuclear matter [Cser 86, Lync 87, Souz 91, Bowm 91, Ogil 91]. Such investigation are often based upon the assumption that the hot nuclear system attains local thermal equilibrium [Cser 86, Lync 87]. As mentioned in the introduction, a recent test of this assumption for $^{14}N + ^{nat}Ag$ reaction at E/A = 35 MeV, revealed strong non-thermal inversions in the excited state populations of emitted $^{10}$B fragments [Naya 89, Naya 92]. Since this measurement was performed without impact parameter selection, there are some questions whether such effects may be related to the dominance of large impact parameter collisions by non-equilibrium transport phenomena [Awes 84, Vand 84, Rand 78, Doss 85]. To explore this issue, we measured $^{10}$B and other particle unbound excited state populations for $36Ar + ^{197}Au$ reaction at E/A = 35 MeV, in conjunction with a charged particle multiplicity filter. Using the charge particle multiplicity as an impact parameter filter, one may try to measure the impact parameter dependence of the emission temperature in a less ambiguous

manner.

In the experiment, a 1.0 mg/cm$^2$ $^{197}$Au target was bombarded with a 1260 MeV $^{36}$Ar beam produced by the K500 cyclotron of the National Superconducting Cyclotron Laboratory of Michigan State University. The Miniball $4\pi$ array was used as an impact parameter filter, while the 13 element hodoscope was used to measure the excited states population for $^{10}$B and other particle unstable intermediate mass fragments (IMF's : Z=3-20) [Mura 89]. Some of the modifications of the hodoscope and the Miniball were described in chapter 2. The 200 $\mu$m non-planar surface barrier silicon detectors in the hodoscope were replaced with 150 $\mu$m planar detector to improve particle identification for the light particle telescopes and simplify the data analysis.

## 5.1 Charge particle multiplicity distribution and impact parameter selection

The impact parameter of a violent nuclear collision can not be directly measured, but can be inferred in many ways [Tsan 89, Phai 92]. The most direct and most widely used impact parameter filter is the charged particle multiplicity [Tsan 89]. It relies on the fact that, when the projectile and target have a head on collision, energy will be more equally shared among all nucleons and therefore more particles will be produced than in peripheral collisions. The particle multiplicity is assumed to have a monotonic dependence upon the impact parameter in this approach. The linear momentum transfer to a target like residue can also serve as impact parameter filter [Faty 87, Chen 87a], because the fraction of linear momentum of the projectile which is transferred to the target nucleus is larger in central collisions than in peripheral reactions. A cross calibration of charged particle multiplicity and the linear momentum transfer filter was performed for $^{36}Ar + ^{238}U$ reactions at 35 MeV/A [Tsan 89]

and the two methods were found to be in qualitative agreement; providing further support for impact parameter filters based on charged particle multiplicity.

For $^{36}Ar + ^{197}Au$ collisions at E/A = 35 MeV, an impact parameter filter has been constructed using the total charged particle multiplicity detected in the Miniball [Kim 92]. The top panel of Figure 5.1 shows the detected total charged particle multiplicity distribution for this experiment. A monotonic relationship has been assumed between the multiplicity and the impact parameter in order to assign the impact parameter using the multiplicity. This can be easily expressed as an integral relationship,

$$(b/b_{max})^2 = \int_{N_c}^{\infty} dP_{N_c} \tag{5.1}$$

Where $b_{max}$ corresponds to the impact parameter at which the mean multiplicity is equal to 2. The bottom panel of Figure 5.1 shows the relationship between the total charged particle multiplicity and the impact parameter obtained from Equation 5.1.

We would like to construct an impact parameter filter for the Miniball-Hodoscope experiment which is equivalent to the impact parameter filter shown in Figure 5.1. To complicate this connection, however, the trigger conditions of the experiments are different. The multiplicity distribution in Figure 5.1 was obtained with a trigger which requires two or more charged particles in the Miniball, while the Miniball-Hodoscope experiment also require at least one more particle in the Hodoscope as well. This additional requirement reduces the contribution from peripheral collisions greatly, as we will see later. Nevertheless, it is straight forward to cross calibrate the multiplicity filters of the two experiments. The details are explained in the following.

We performed this cross calibration using data from the Miniball standalone experiment. It was important to select events in this latter experiment which are equivalent

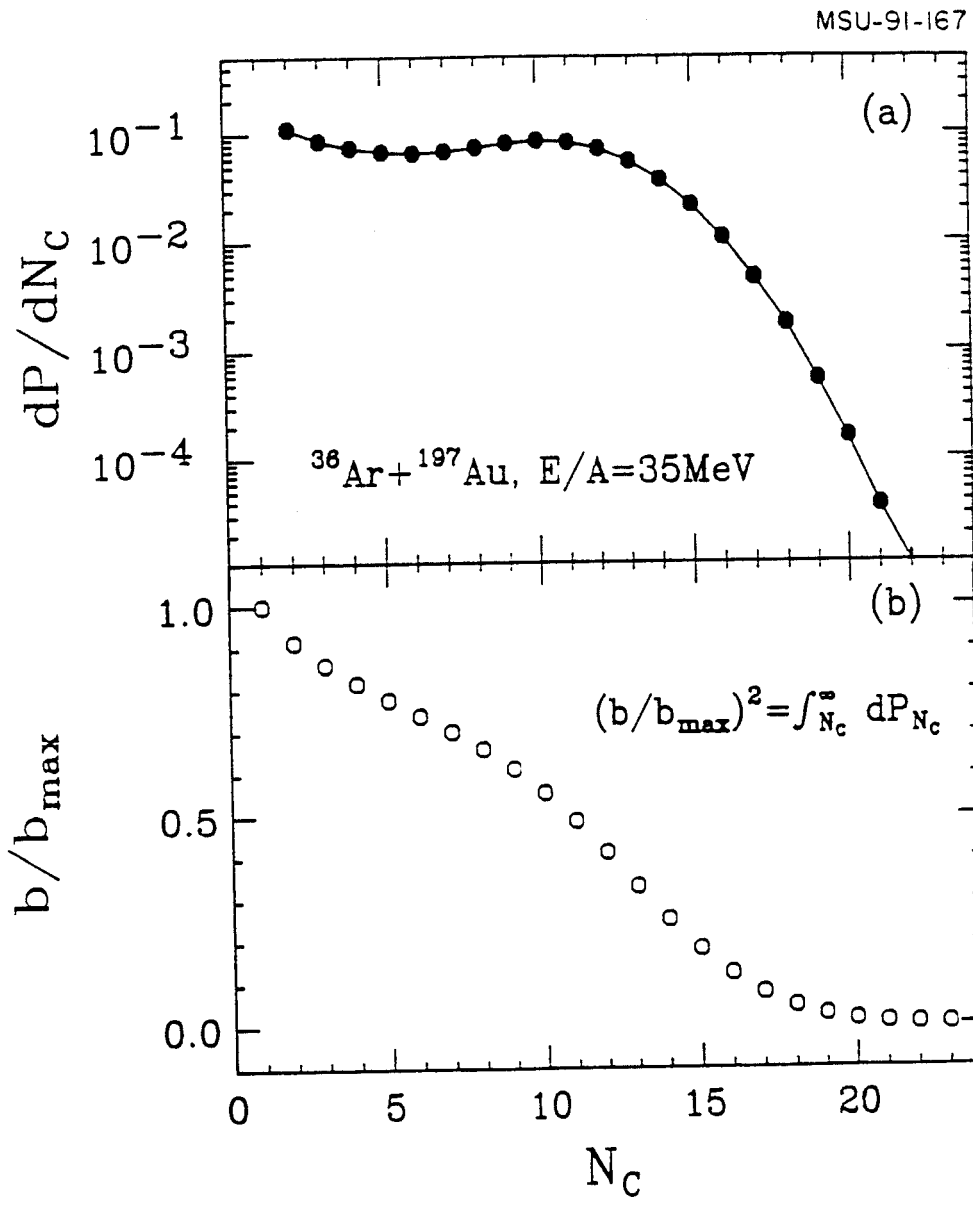


Figure 5.1: The plot shows total charged particle multiplicity (upper panel) and the extracted impact parameter (lower panel) and their relationship, from $^{36}Ar + ^{197}Au$ reaction at E/A = 35 MeV with Miniball as a standalone device [Kim 92].

to those measured in the Miniball-Hodoscope experiment. Several steps were taken to make this correspondence.

1. Some of these detectors which were at the appropriate angles were chosen to mimic the hodoscope telescopes.

2. We require the detection of one intermediate mass fragment (IMF, Z=3-20) in these pseudo-hodoscope telescopes.

3. We removed from the analysis of the Miniball standalone experiment those detectors which were removed in the Miniball-Hodoscope experiment.

4. The resulting associated multiplicity could then be plotted as a function of the total charged particle multiplicity in the total array to obtain the correspondence between the two quantities. In this fashion one could calibrate the impact parameter filter based upon the associated charged particle multiplicity.

In the Figure 5.2, we show the correlation between the mean total ($< N_c >$) and associated ($N_a$) charged particle particle multiplicities for events in which a $^{10}B$ nucleus is detected in the pseudo-hodoscope detectors. In general, $< N_c > \approx N_a + 2$ over the range of events considered. On the right hand side, we show the impact parameter assignment deduced from the relationship between $N_c$ and b in Figure 5.1.

The associated charged particle multiplicity distribution of the Mini-Ball in coincidence with $^{10}$B nuclei detected in the hodoscope is shown in Figure 5.3. The solid squares indicate the probability of observing a charged particle multiplicity $N_A$ in the Miniball in coincidence with the detection of a $^{10}$B nucleus in the hodoscope. The dashed line indicates the corresponding inclusive multiplicity distribution, arbitrarily normalized, which was obtained with the part of Miniball which was used as a filter, but without the requirement of the detection of a $^{10}$B nucleus in the hodoscope. In

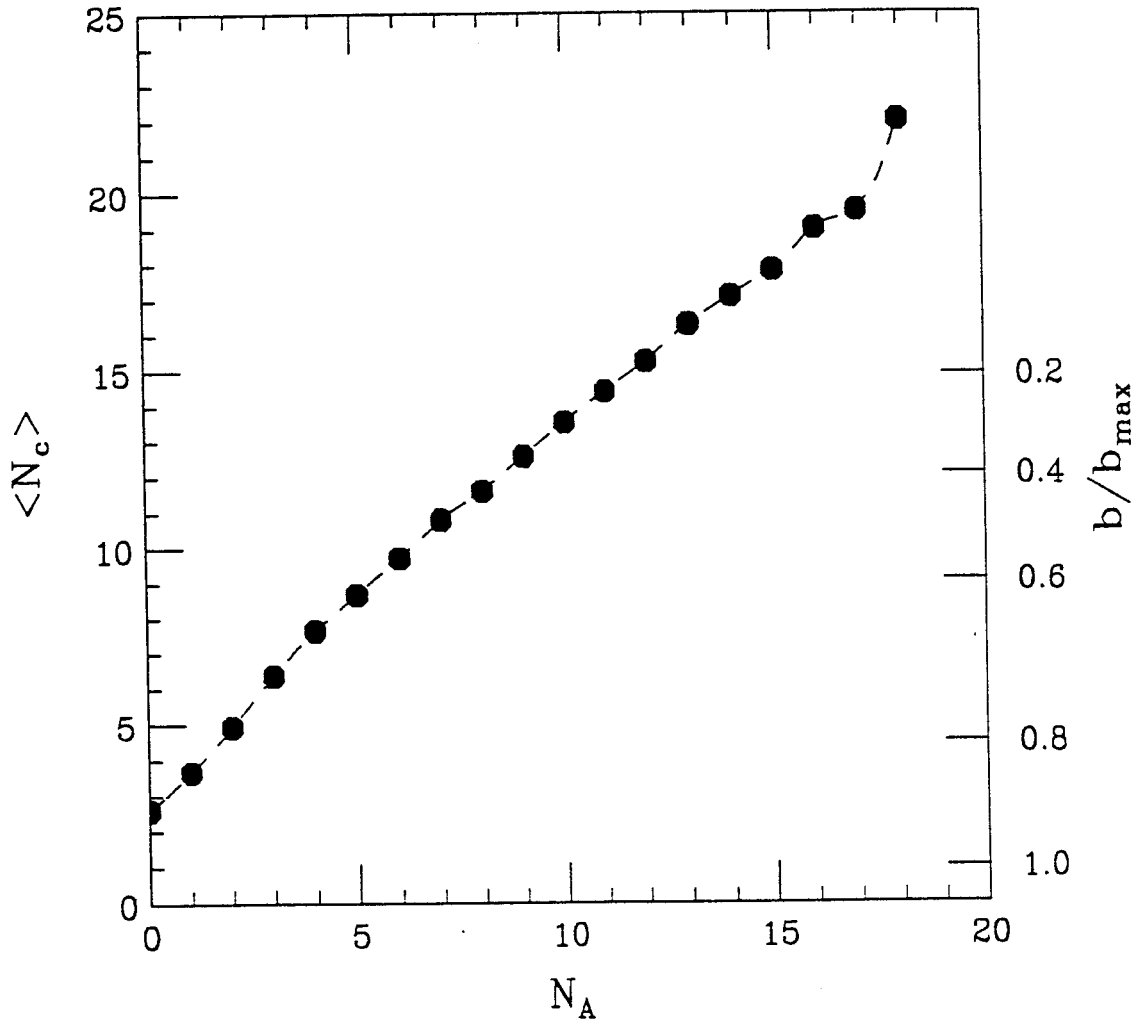


Figure 5.2: The cross calibration of associated multiplicity and total multiplicity and the extracted impact parameter for the $^{36}Ar + ^{197}Au$ reaction at E/A = 35MeV.

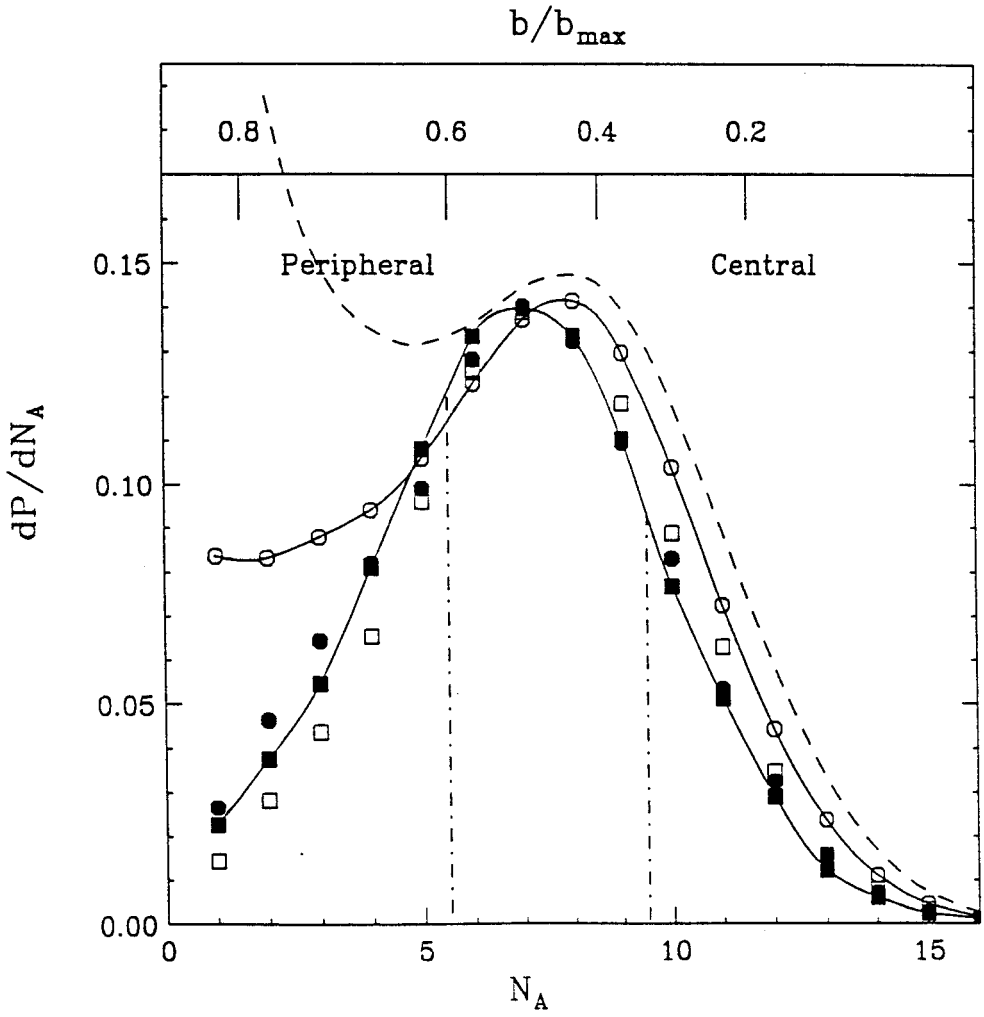


Figure 5.3: The inclusive associated multiplicity distribution, arbitrarily normalized,the of Miniball array is shown as a dashed line for the $^{36}Ar + ^{197}Au$ reaction at E/A = 35MeV. When requiring a $^{10}B$ nucleus or proton detected in the hodoscope, the distribution becomes the solid squares and open circles respectively. The solid circles represents the distribution by requiring $\alpha$ and $^{6}Li$ detected in coincidence in the hodoscope, while open squares represents the corresponding pseudo-hodoscope simulation.

the case of events triggered with a $^{10}$B nucleus, the probability of having very high multiplicity events is reduced, possibly reflecting the fact that $^{10}B$ takes away a great amount of energy, leaving less excitation energy for particle emission. This interpretation is supported by the associated multiplicity distribution corresponding to the detection of one proton in the hodoscope, shown by the open circles. Protons carry away less energy and have an associated multiplicity distribution which deviates less from the inclusive multiplicity distribution (dashed line). For both protons and $^{10}$B fragments, the detection of one charged particle in the Hodoscope suppresses the peripheral reactions greatly. This effect is stronger for the $^{10}$B distribution than for the protons, consistent with previous observations [Souz 90, Kim 92].

The solid squares in Figure 5.3 show the corresponding multiplicity distribution for correlated $^6$Li and $\alpha$ particles detected in the hodoscope. Both the $^{10}B$ (solid squares) and $\alpha - ^6 Li$ (solid circles) trigger conditions appear to select equivalent impact parameters. The open squares show the associated multiplicity distribution for $\alpha - ^6 Li$ events obtained with the pseudo-hodoscope trigger condition imposed on the Miniball for the experiment which was performed in the standalone mode. Clearly this simulated data is nearly indistinguishable from the $\alpha - ^6 Li$ data taken in the Miniball-Hodoscope experiment.

The impact parameter selection gates, indicated by the dashed-dotted lines, were used later on to distinguish **peripheral** ($N_A \leq 5$) and **central** collisions ($N_A \geq 10$) collisions. Also shown at the top of the figure is the impact parameter scale which was obtained from Figure 5.2 using Equation 5.1.

## 5.2 The impact parameter selected particle singles cross section

Figure 5.4 shows the energy spectra for protons, deuterons, and tritons for the peripheral ($5 \leq N_A$) and central ($N_A \geq 10$) collision gates. The spectra for peripheral collisions (left panels) are considerably more forward peaked and more energetic than the spectra for central collisions(right panels). The energy range of the spectra is rather limited because protons with energies larger than 30 MeV penetrate through the 5 mm silicon(Li) detectors and can not be separated isotopically. The spectra have been fitted with Equation 4.1 and the fitting parameters are listed in Table 5.1.

The multiplicity gated singles energy spectrum for other particle types are shown in Figure 5.5. As before, the left panels are gated on peripheral reactions and those in the right panels are gated on central reactions. In general, the spectra for peripheral collisions are more forward peaked and are flatter at forward angles than the spectra for central collisions. This is consistent with a greater dissipation of the incident energy into other degrees of freedom for central collisions. The solid lines depict the moving source fits to the energy spectra. These will be used later on for efficiency function calculations. The corresponding moving source fitting parameters are listed in Table 5.1. It is important to note that, due to the limited angular range of the data in Figure 5.4 and Figure 5.5, the moving source parameters in Table 5.1 are not reliable for extrapolation to scattering angles which lie outside the angular range covered by the Hodoscope. Thus the parameters are useful only as input to the efficiency calculations to extract the population probabilities in section 5.4.

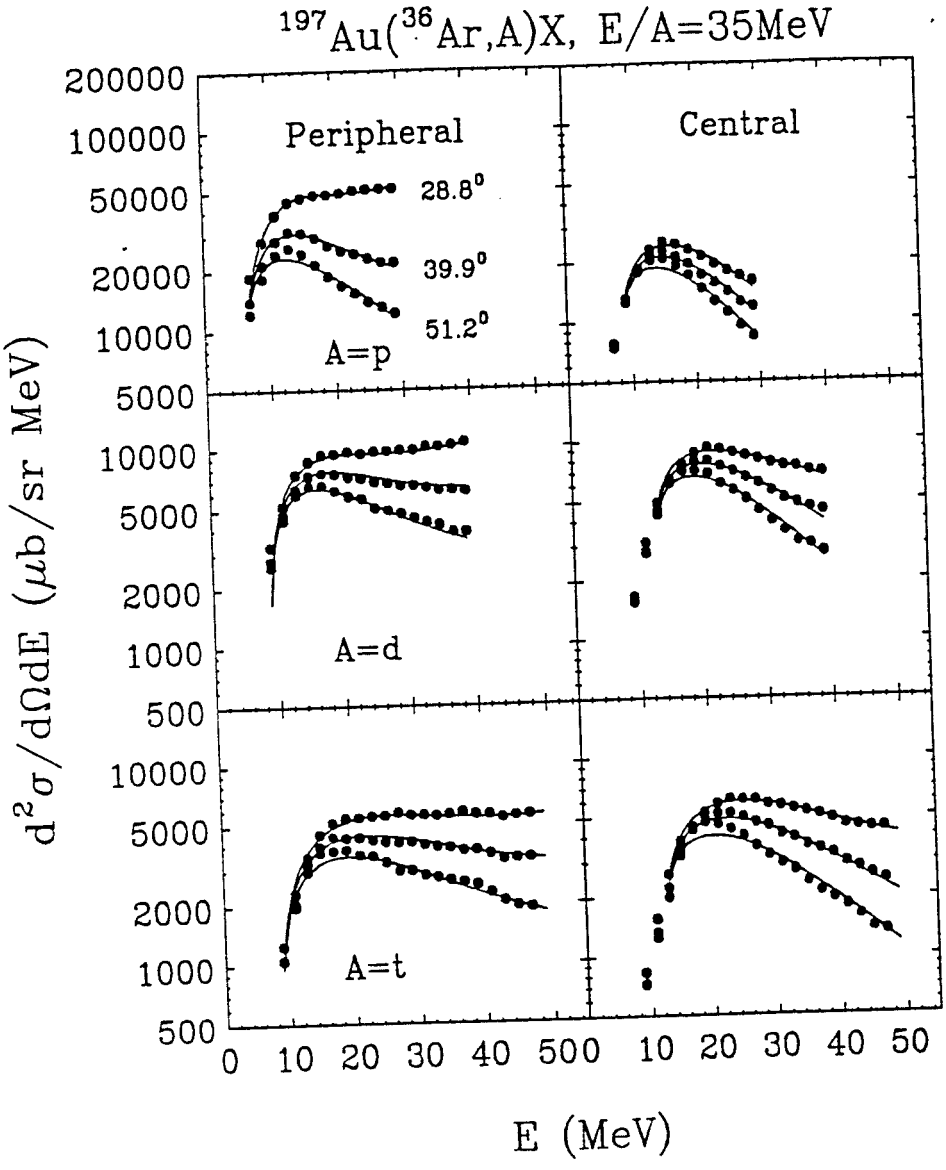


Figure 5.4: Single particle cross sections for p, d, t emitted in the $^{36}$Ar + $^{197}$Au reaction at E/A=35 MeV. The left panels correspond to the peripheral collision gate ( $N_A \leq 5$), and the right panels correspond to the central collision gate ( $N_A \geq 10$). The curves are the corresponding moving source fits using Equation 4.1 with fitting parameters shown in Table 5.1.

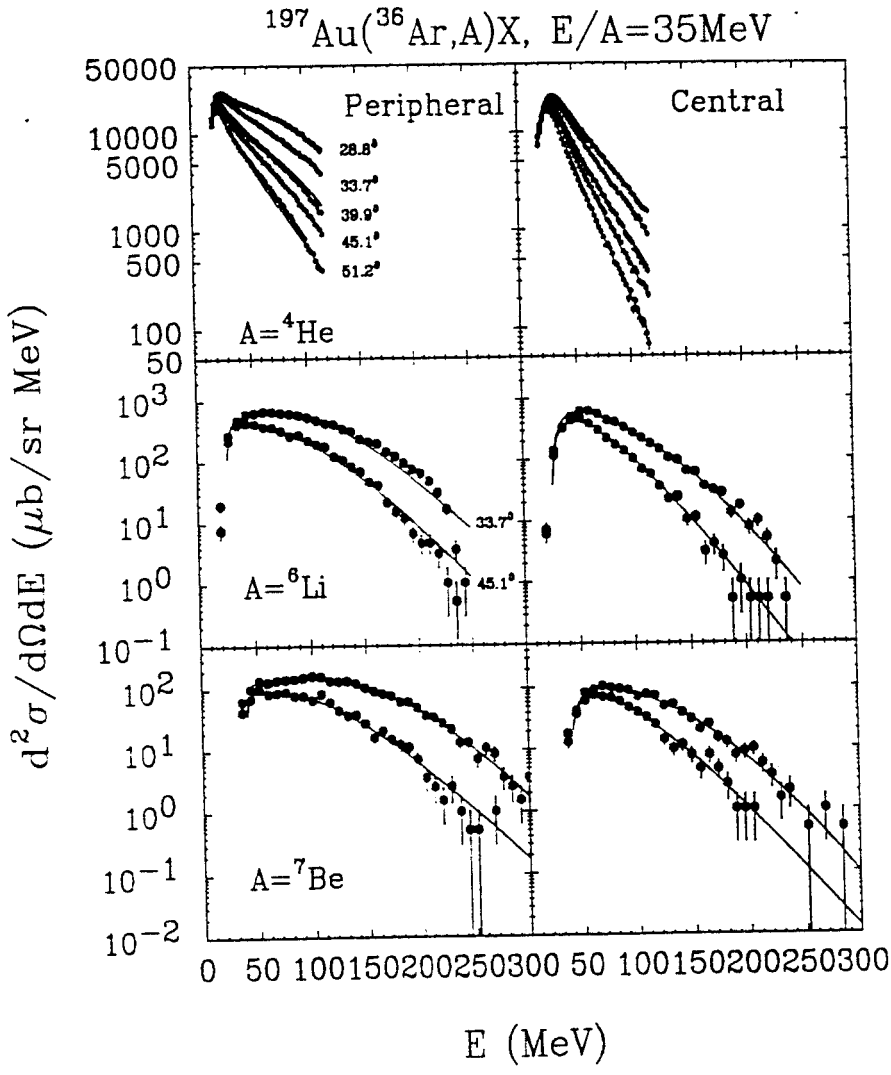


Figure 5.5: Single particle cross sections for $^4He$, $^6Li$ and $^7Be$ particles emitted in the $^{36}$Ar + $^{197}$Au reaction at E/A=35 MeV. The left panels correspond to the peripheral collisions gate ( $N_A \leq 5$) and the right panels correspond to the central collision gate ( $N_A \geq 10$). The curves are the corresponding moving source fits using Equation 4.1 with fitting parameters shown in table 5.1.

Table 5.1: The moving source fitting parameters of the energy spectrum of peripheral collision gate (top panel) and central collision gate (bottom panel) for particles produced in $^{36}Ar + ^{197}Au$ reaction at E/A=35MeV. The cross section unit for $N_i$ is $\mu$b/MeV/sr, the temperature unit for $T_i$ is MeV.

| Part | $N_1$ | $\beta_1$ | $T_1$ | $N_2$ | $\beta_2$ | $T_2$ | $N_3$ | $\beta_3$ | $T_3$ |
|---|---|---|---|---|---|---|---|---|---|
| p | 4404 | 0.1368 | 2.22 | 2861 | 0.0395 | 10.93 | 16305 | 0.288 | 4.44 |
| d | 197.0 | 0.0 | 10.58 | 749.0 | 0.0621 | 7.55 | 1591 | 0.3122 | 19.92 |
| t | 129.9 | 0.0 | 16.81 | 367.6 | 0.0750 | 9.36 | 924.7 | 0.3207 | 27.47 |
| $^4$He | 2942 | 0.0155 | 2.81 | 1875 | 0.0575 | 7.43 | 1248 | 0.1588 | 12.34 |
| $^6$Li | 417.5 | 0.0001 | 13.52 | 622.7 | 0.1393 | 15.12 | | | |
| $^7$Be | 111.8 | 0.0435 | 3.42 | 1534 | 0.2085 | 9.27 | 90.22 | 0.1056 | 19.20 |
| $^{10}$B | 41.99 | 0.0543 | 14.74 | 89.25 | 0.1346 | 17.98 | | | |

| | | | | | | | | | |
|---|---|---|---|---|---|---|---|---|---|
| p | 165.9 | 0.0787 | 7.53 | 2282 | 0.0232 | 10.01 | 1047 | 0.1432 | 5.35 |
| d | 1674 | 0.0 | 0.35 | 952.1 | 0.0497 | 9.26 | 609.8 | 0.2070 | 6.38 |
| t | 311.6 | 0.0001 | 13.74 | 309.9 | 0.0841 | 8.24 | 626.5 | 0.2323 | 8.98 |
| $^4$He | 1920 | 0.0001 | 10.72 | 1351 | 0.0814 | 6.14 | 471.8 | 0.1478 | 10.68 |
| $^6$Li | 403.1 | 0.0790 | 14.00 | 931.2 | 0.1870 | 8.34 | | | |
| $^7$Be | 14.19 | 0.0001 | 26.21 | 170.8 | 0.1759 | 9.52 | 53.05 | 0.0826 | 15.88 |
| $^{10}$B | 78.28 | 0.086 | 13.67 | 46.77 | 0.1595 | 11.40 | | | |

## 5.3 The impact parameter selected two particle correlation functions

As we demonstrated in the last chapter, two particle correlation functions are sensitive to the space time extent of the region emitting these particles. In the participant spectator model [Goss 77], pre-equilibrium particles are emitted from the region of geometrical overlap between projectile and target nucleus. This overlap region is small in peripheral collisions, and involves most of the projectile and target nucleus for central collisions. BUU calculations also predict that the source size deduced from proton-proton correlation functions will follow the general trends predicted by the participant spectator model for protons with $V_{proton} < V_{beam}$ [Gong 91]. The dependence of the source radii on impact parameter for protons with $V_{proton} > V_{beam}$ is considerably more complicated [Gong 91]. Impact parameter selected two proton correlation functions has been explored for collisions at $E/A = 400$ MeV [Gust 84]. These measurements were consistent with small sources for peripheral collisions and large sources for central collisions, consistent with the participant spectator model. By using the source sizes extracted from p-p correlation function and the proton multiplicity, Gustafsson *et al.* deduced a freeze out density of the collision (ie. the density where interactions between protons cease) which was about 25% of normal nuclear matter density.

The multiplicity selected two proton correlation functions is shown in Figure 5.6. Since the NaI(Tl) detectors were taken away in order to fit the hodoscope into the Miniball array, the maximum energy of stopped protons is less than 30 MeV and the mean value of $V_p/V_{beam} \approx 0.74$. Over this range of proton energies, the proton spectra have large evaporation contributions and the proton correlation functions should therefore correspond to a large and/or long lived source. As shown in Figure 5.6, the

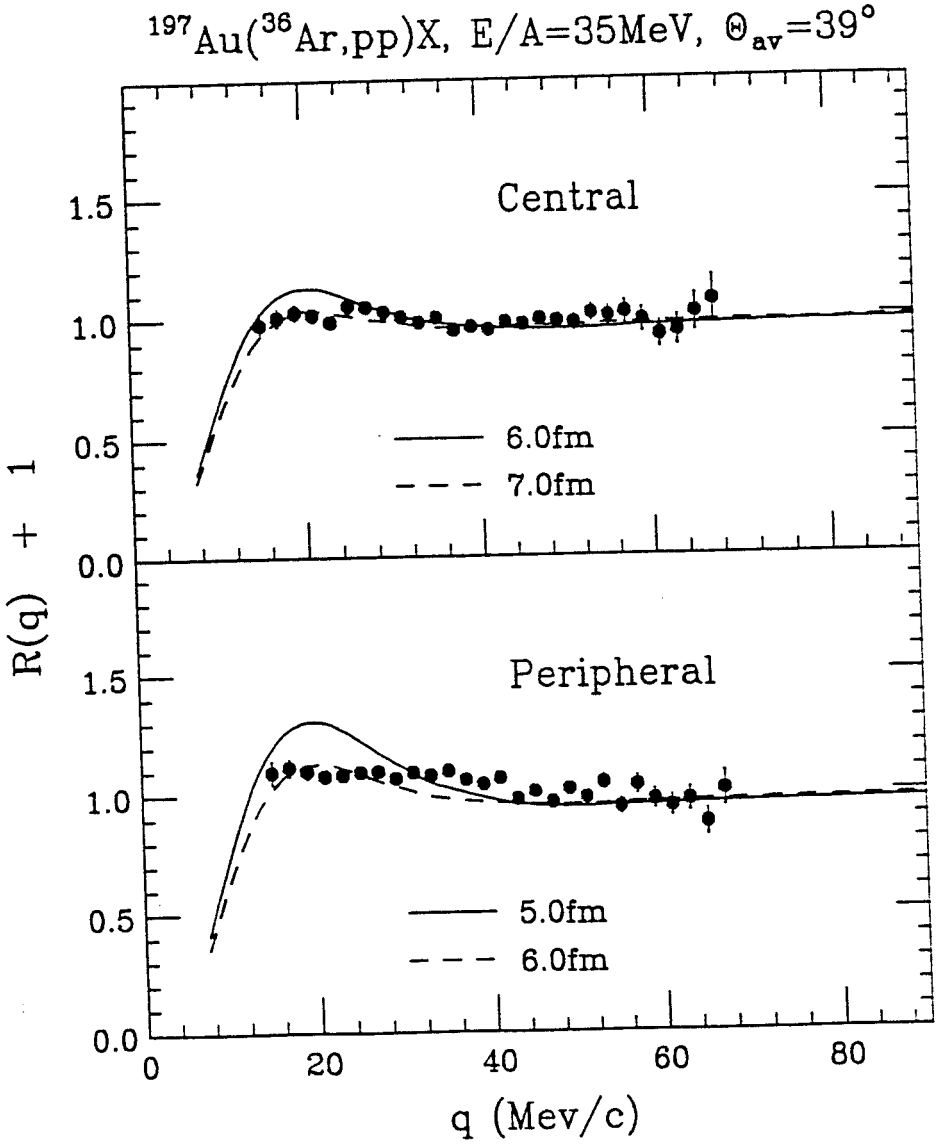


Figure 5.6: proton-proton correlation functions selected by the impact parameter in the $^{36}Ar + ^{197}Au$ reaction at E/A=35 MeV.

correlation functions are small. For illustration, a gaussian source with a zero lifetime is used to fit the correlation function. The corresponding source radii are shown in the figure as well.

Deuteron-alpha correlation functions can be explored over a larger energy range in this experiment. Deuteron-alpha correlation functions gated on multiplicity are shown in Figure 5.7. The top panel depicts correlation functions gated on peripheral reactions and the bottom one depicts correlation functions gated on central collisions. Central collisions display smaller correlation functions, consistent with larger source sizes than those observed for peripheral collisions. For illustration, a gaussian source with a zero lifetime is used to fit the correlation function. The corresponding source radii are shown in the figure as well.

The extracted source sizes for $d-\alpha$ correlation functions are plotted as a function of the impact parameter in Figure 5.8 as solid circles. The extracted source sizes for p-p correlation functions are plotted as solid squares for comparison. The general trends of larger source sizes for central collisions is consistent with the trends predicted by the participant spectator model. It is also consistent with trends predicted by BUU simulations for particles with velocity less than the beam velocity [Gong 91]. The extracted source sizes from $d-\alpha$ correlation functions are smaller than the source sizes from p-p correlation functions, but they do not follow the scaling factor 0.7. It should be noted that the $^{40}Ar$ correlation functions in Figure 4.5 also did not follow the scaling behavior at $V_p/V_{bean} \approx 0.7$. This may be due to the low energy range of the detected protons, where source lifetimes play a more important role than the source spatial dimensions.

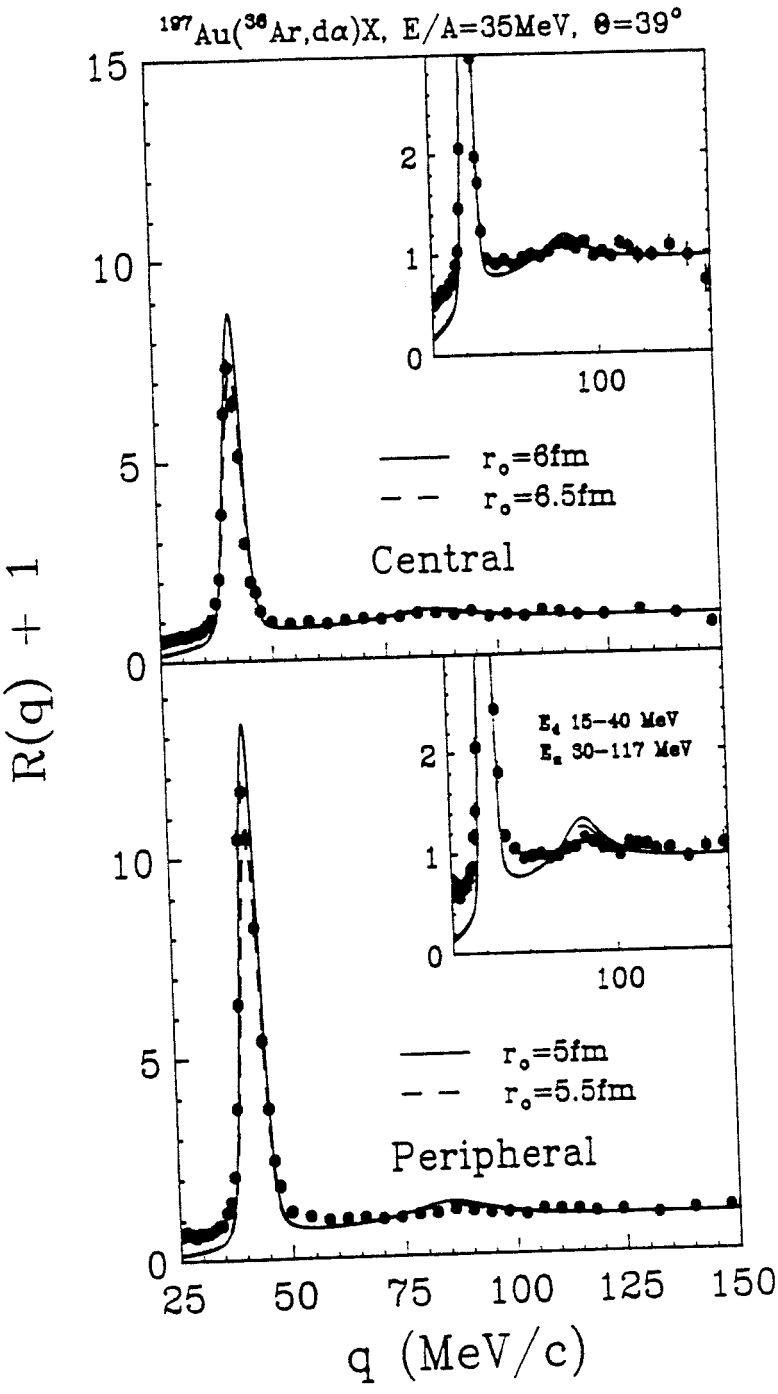


Figure 5.7: deuteron-alpha correlation functions selected by the impact parameter in the $^{36}$Ar + $^{197}$Au reaction at E/A=35 MeV.

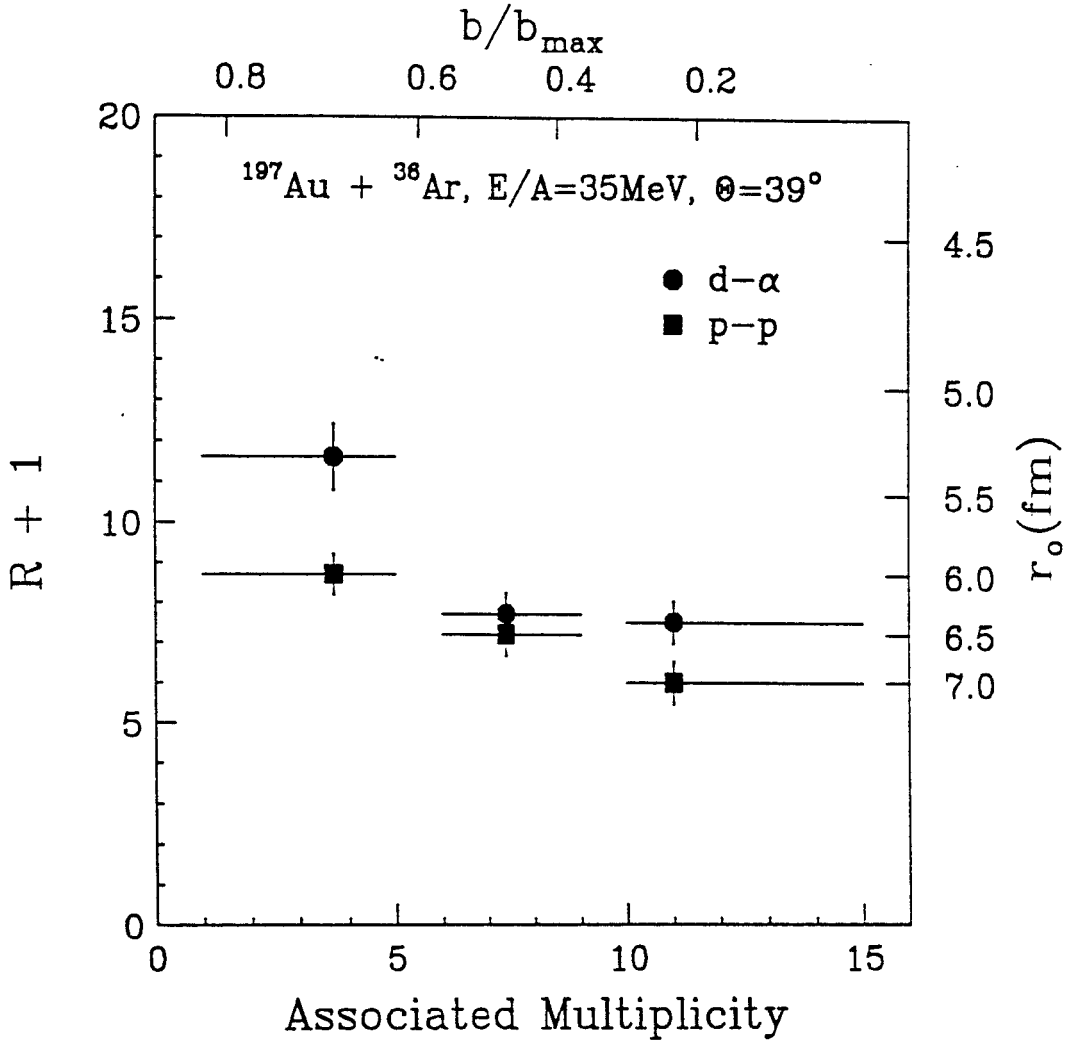


Figure 5.8: The extracted source size as a function of impact parameter, from deuteron-alpha correlations in the $^{36}Ar + ^{197}Au$ reaction at E/A=35 MeV, are ploted as solid circles. The extracted source size from p-p correlation functions are ploted as solid squares for comparison.

## 5.4 Impact parameter selected $^{10}B$ excited state populations, and thermalization in nucleus-nucleus collisions.

Light nuclei only have one or two excited states which may be used to extract temperature from population probabilities of excited states [Chen 88]. Testing the internal consistency of such a temperature extraction, however, requires the exploration of many excited states to see if they are consistent with a common temperature. For such purposes, we examined $^{10}$B nuclei for which many excited states of known spins and parities can be measured [Naya 89]. We examined five excited states which decay by the $^{10}B \rightarrow {}^{6}Li + \alpha$ and $^{10}B \rightarrow {}^{9}Be + p$ channels. Previous inclusive measurements of $^{10}B$ excited states have revealed non-statistical population inversions [Naya 89]. By allowing an impact parameter selection, we examine whether these non-statistical population inversions are coming from peripheral collisions [Zhu 92].

Figure 5.9 shows the energy spectra for $^{10}$B nuclei detected at $45^0$ in the high resolution hodoscope, for low multiplicity (solid points) and high multiplicity (solid squares) gates on the Miniball. The solid lines denote moving source fits, which were used in the efficiency calculations. The energy spectra for peripheral collisions extends to higher energies than the energy spectra for central collisions. This suggest a greater degree of thermalization for central collisions.

The population probabilities of particle unstable states in $^{10}$B nuclei were measured by detecting their coincident decay products. These yields are shown as a function of excitation energy for the $^{10}B \rightarrow {}^{6}Li + \alpha$ and $^{10}B \rightarrow {}^{9}Be + p$ decay channels in the upper and lower halves of Figure 5.10 respectively. Spectra obtained for peripheral and central collisions are shown in the left and right sides of the figure, respectively. The separation energy $E_b$ for each decay channel and the locations and

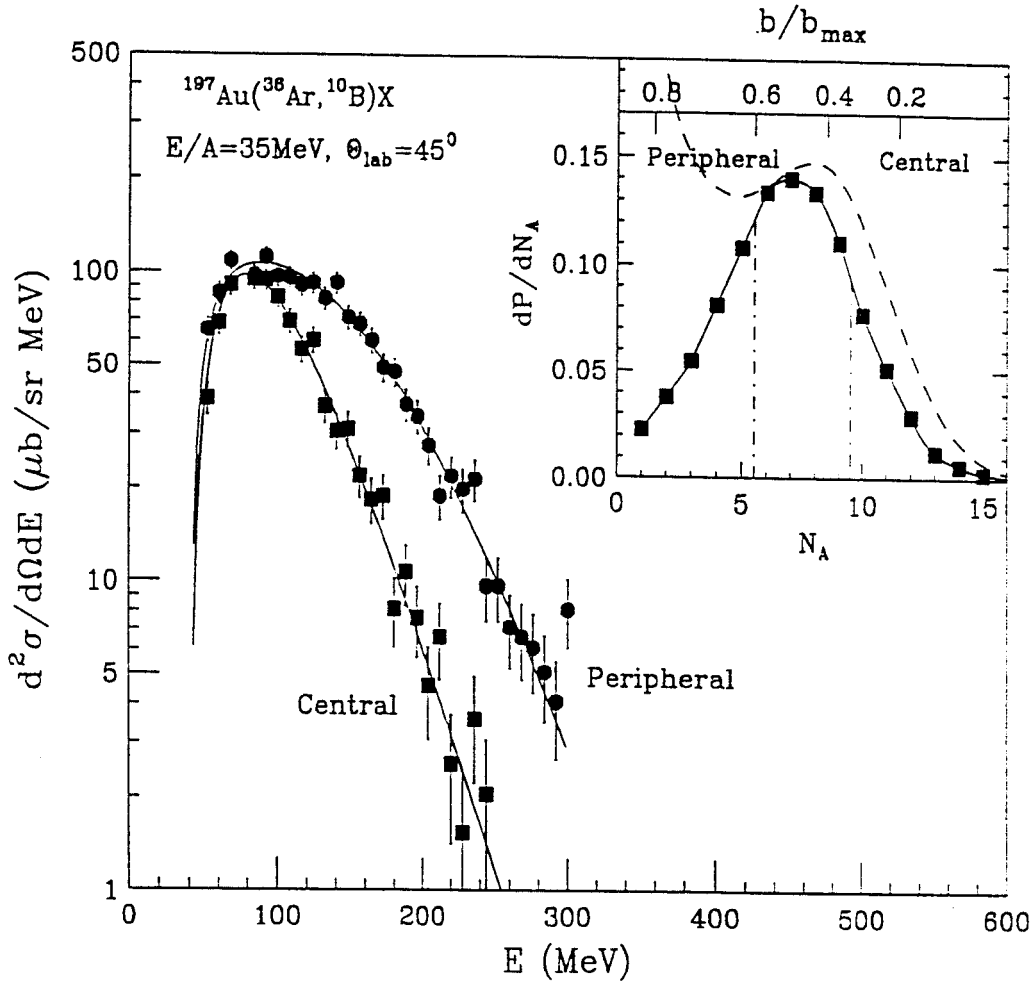


Figure 5.9: Energy spectra for $^{10}$B nuclei detected at 45$^0$ in the high resolution hodoscope, for low multiplicity (solid points) and high multiplicity (solid squares) gates on the Miniball. The solid lines denote moving source fits, used in the efficiency calculations.

spins of the relevant particle unstable excited states of $^{10}$B nuclei are indicated in the left hand panels of the figure.

We analyzed four peaks in the $^{10}B \rightarrow {}^{6}Li + \alpha$ decay channel (upper panels). The first peak is the $^{10}B$ excited state at E* = 4.774 MeV with spectroscopic parameters $J^{\pi} = 3^{+}, \Gamma = 0.0084$ KeV, $\Gamma_{\alpha}/\Gamma = 1.0$. The second peak consists of threes excited states at E* = 5.1103 MeV ($J^{\pi} = 2^{-}, \Gamma = 0.98$ KeV, $\Gamma_{\alpha}/\Gamma = 1.0.$ ), E* = 5.1639 MeV ($J^{\pi} = 2^{+}, \Gamma = 0.00176$ KeV, $\Gamma_{\alpha}/\Gamma = 0.13.$), and E* = 5.18 MeV ($J^{\pi} = 1^{+}, \Gamma = 110$ KeV, $\Gamma_{\alpha}/\Gamma = 1.0.$ ). The third peak also consists of three states, E* = 5.9159 MeV ($J^{\pi} = 2^{+}, \Gamma = 6$ KeV, $\Gamma_{\alpha}/\Gamma = 1.0.$ ), E* = 6.0250 MeV ($J^{\pi} = 4^{+}, \Gamma = 0.05$ KeV, $\Gamma_{\alpha}/\Gamma = 1.0.$ ), and E* = 6.1272 MeV ($J^{\pi} = 3^{-}, \Gamma = 2.36$ KeV, $\Gamma_{\alpha}/\Gamma = 0.97.$ ). The fourth peak is at E* = 6.56 MeV with spectroscopic parameters $J^{\pi} = 4^{-}, \Gamma = 25.1$ KeV, $\Gamma_{\alpha}/\Gamma = 1.0$. Following ref. [Naya 89], two excited states of $^{10}$B at E* = 8.889 MeV and E* = 8.895 MeV, which decay to the 3.563 MeV excited state of $^{6}$Li by $\alpha$ emission, were included in the fitting of the spectrum but had statistically insignificant yields and were not analysed further.

The decay spectra for the $^{10}B \rightarrow {}^{9}Be + p$ decay channel were shown in the lower panels. We concentrated on the group of four states at, E* = 7.43 MeV ($J^{\pi} = 2^{-}, \Gamma =$ 100 KeV, $\Gamma_{p}/\Gamma = 0.70.$ ), E* = 7.467 MeV ($J^{\pi} = 1^{+}, \Gamma = 65$ KeV, $\Gamma_{p}/\Gamma = 1.0.$ ), E* = 7.478 MeV ($J^{\pi} = 2^{+}, \Gamma = 74$ KeV, $\Gamma_{p}/\Gamma = 0.65.$ ), and E* = 7.5595 MeV ($J^{\pi} = 0^{+}, \Gamma = 2.65$ KeV, $\Gamma_{p}/\Gamma = 1.0.$ ). The peak near the threshold consists of two peaks of 6.873 and 7.002 MeV, which we included in the fit, but lacking the relevant branching ratio information, we did not extract the population ratio from them. The other group of states consists of three states, E* = 7.67 MeV ($J^{\pi} = 1^{+}, \Gamma = 250$ KeV, $\Gamma_{p}/\Gamma = 0.30.$ ), E* = 7.819 MeV ($J^{\pi} = 1^{-}, \Gamma = 260$ KeV, $\Gamma_{p}/\Gamma = 0.9.$ ), and E* = 8.07 MeV ($J^{\pi} = 2^{+}, \Gamma = 800$ KeV, $\Gamma_{p}/\Gamma = 0.1.$ ). Those states are included in the fit, but were not analyzed further because the statistics were insignificant to draw

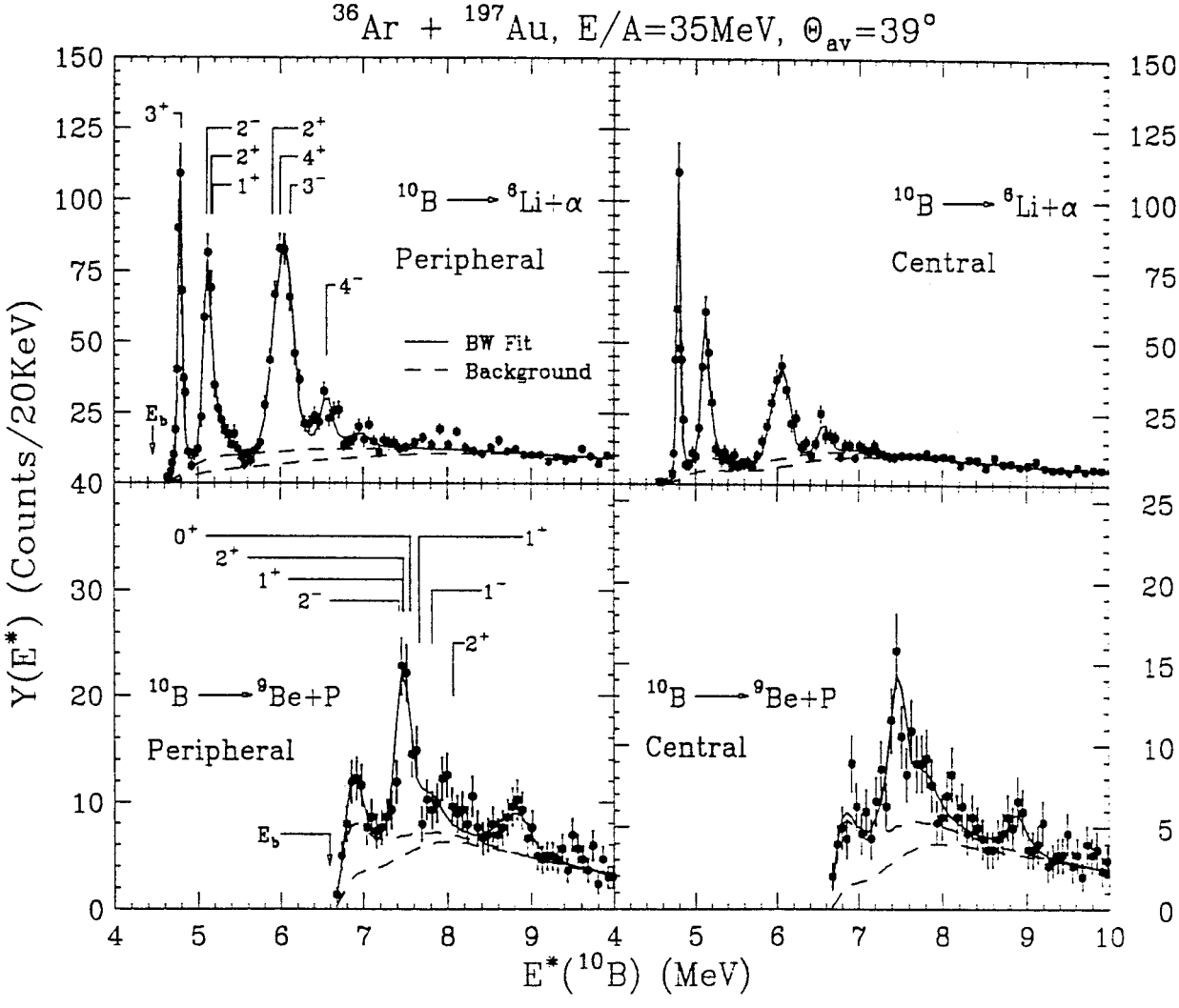


Figure 5.10: Yields for the decays: $^{10}B \rightarrow {}^{6}Li + \alpha$ (upper half) and $^{10}B \rightarrow {}^{9}Be + p$ (lower half). Spectra obtained for peripheral and central collisions are shown on the left and right hand sides, respectively. The curves are described in the text.

any conclusions. A small peak near 8.9 MeV consists of two peaks, E* = 8.889 MeV ($J^\pi = 3^-, \Gamma = 84$ KeV, $\Gamma_p/\Gamma = 0.95.$ ), and E* = 8.895 MeV ($J^\pi = 2^+, \Gamma = 40$ KeV, $\Gamma_p/\Gamma = 0.19.$ ). These two states were included in the fit also, but the statistics were also too insignificant to draw any conclusions.

The population probabilities, $n_i$, were extracted by fitting the coincidence yield, for different assumptions about the background. Reasonable fits were obtained for backgrounds lying within the values bounded by the dashed lines in Figure 5.10. The population probabilities, $n_a$, were assumed to be the same within those groups of states in Figure 5.10, which were not resolved experimentally. The best fits to the coincidence yields, are shown by the solid curves in Figure 5.10.

Figure 5.11 shows the measured population probabilities as a function of excitation energy for peripheral (left side) and central (right side) collisions. The error bars include the uncertainties in the background subtraction bounded by the two assumed background coincidence yields displayed in Figure 5.10. In thermal as well as many statistical models, the initial excited state population probabilities of intermediate mass fragments should be proportional to a Boltzmann factor, $exp(-E^*/T_{eff})$ where $T_{eff}$ is the effective temperature of the system at breakup. The dashed lines in Figure 5.11 show the exponential dependence dictated by the Boltzmann factor for $T_{eff} = 4$ MeV. For peripheral collisions, the measured relative populations deviate significantly from the expected monotonic behavior and a population inversion is observed; the group of states at E $\approx$ 6.0 MeV is populated much more strongly than the lower lying states at 5.2 and 4.8 MeV. Such effects were also observed in the inclusive measurements of ref. [Naya 89]. The inversions disappear for central collisions. The population probabilities, however, do not fall off exponentially as expected from the Boltzmann factor; instead, one observes an approximately constant population probability for the 5.2 and 6.0 MeV levels.

The initial populations of excited states will be modified by the sequential feeding from heavier particle unstable nuclei. These feeding corrections have been estimated via calculations in which it is assumed that the excited states of primary emitted fragments are populated thermally; the initial elemental yields are subject to a constraint that the final elemental distributions are consistent with the measured elemental distributions [Naya 89, Naya 92]. Details of the calculation are given in chapter 3. In these calculations, decay branching ratios were calculated from the Hauser-Feshbach theory [Haus 52] with parity and isospin conservation taken into account [Naya 92]; known branching ratios [Ajze 87] were used when available. Unknown spins or parities of low lying discrete states were assigned randomly and calculations repeated with different spin assignments until the sensitivities of the population probabilities to these uncertainties could be assessed.

In order to provide an overall comparison between the calculated and measured population probabilities, a least squares analysis was performed by computing $\chi^2_\nu(T)$ for a range of initial emission temperatures.

$$\chi^2_\nu(T) = \frac{1}{\nu}\sum_{i=1}^{\nu}\frac{(n_{exp,i} - n_{cal,i}(T))^2}{\sigma^2_{exp,i} + \sigma^2_{cal,i}}. \tag{5.2}$$

Here, $n_{exp,i}$ and $n_{cal,i}(T)$ are the measured and calculated population probabilities and $\sigma^2_{exp,i}$ and $\sigma^2_{cal,i}$ are the corresponding uncertainties. The resulting values of $\chi^2(T)$ are shown in Figure 5.12. Optimal agreement between calculated and measured population probabilities is obtained for both central and peripheral collisions at temperatures of about $T \approx 3 - 5$ MeV. Similar residue temperatures have been obtained in dynamical [Xu 92, Boal 89] and in statistical [Levi 84, Gros 88, Bond 85, Frid 88] calculations.

For T = 4 MeV, the population probabilities obtained by the sequential decay calculations are indicated by the open bars in the Figure 5.11; the vertical extent

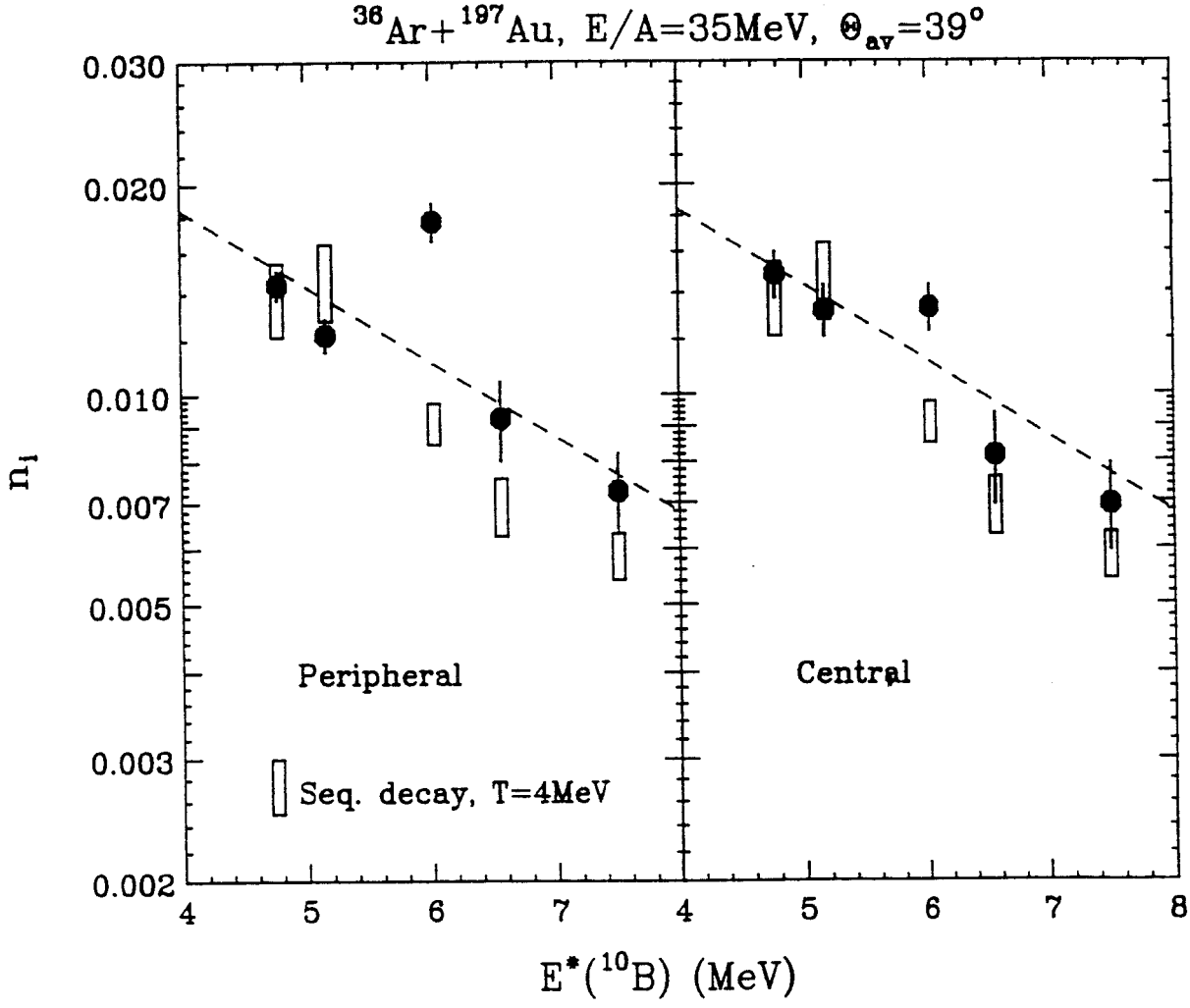


Figure 5.11: The solid points designate population probabilities for the excited states of $^{10}$B nuclei measured for peripheral (left side) and central (right side) collisions. The open bars indicate the results of the sequential decay calculations. The dashed lines denote exponential exp(-E/T) with T = 4 MeV.

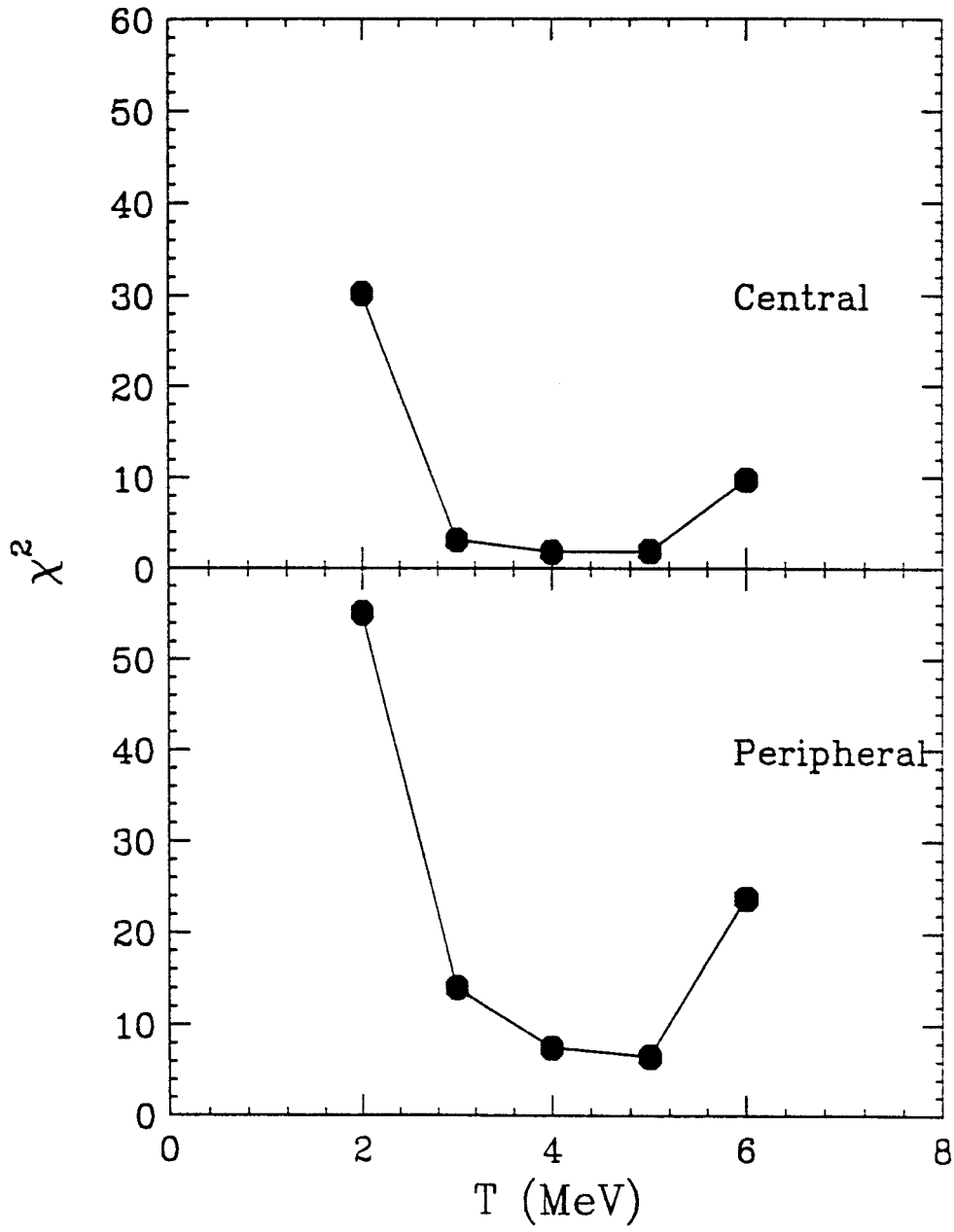


Figure 5.12: Values for $\chi^2$(T) are calculated, according to Equation 5.2, for temperatures ranging from 2 to 6 MeV.

of the bars graphically demonstrates the range of theoretical values obtained for ten randomly chosen assumptions about the unknown spins of low lying discrete states. Rotational effects may add comparable contributions to the uncertainties in the calculated population probabilities [Naya 92]. The population probabilities obtained from the sequential decay calculations cannot be reconciled with the population inversions observed for peripheral collisions. For central collisions, on the other hand, the discrepancies between calculated and measured population probabilities are much smaller, but still too large for a purely thermal interpretation.

## 5.5 Impact parameter selected excited state populations for $^5$Li, $^6$Li, and $^7$Be fragments.

In addition to $^{10}$B fragments, we can analyze several excited states of $^5$Li, $^6$Li, and $^7$Be fragments to test our preliminary conclusions that greater thermalization is achieved in central collisions. Although each of these nuclei has only one or two excited states which can be analyzed, the overall trend may provide sufficient information for a comparison.

$$^5Li \rightarrow p + \alpha$$

The ground state of $^5$Li is not particle stable, it decays to a proton and an alpha particle, $^5Li \rightarrow p+\alpha$. The $p-\alpha$ correlation function is shown in Figure 5.13. The left panel shows the results for peripheral collisions and the right panel shows the results for central collisions. The broad peak at $E_{rel} \approx 2$ MeV is from the decay of the $^5Li$ ground state with spectroscopic parameters $J^\pi = \frac{3}{2}^-, \Gamma = 1.5$ MeV, $\Gamma_p/\Gamma = 1.0$. At low relative energies, there is a narrow peak at $E_{rel} \approx 0.19$ MeV, which is attributed to the decay of ground state of $^9B$. $^9B_{g.s} \rightarrow p + {}^8Be_{g.s} \rightarrow$ p + $\alpha + \alpha$ [Naya 92]. When we fit the data using the Breit-Wigner formula, a second resonance is included

at $E_{rel} = 0.19$ MeV with a decay width of $\Gamma = 0.055$ MeV to accommodate this process. Because the state at $E_{rel} \approx 2$ MeV is very broad, we include the line shape distortions caused by the Boltzman factor $exp(-E/T)$, with $T = 4$ MeV, in the fit. The best fit is shown as the solid line in the figure. The two dashed lines shows the upper and lower extremes of the estimated background, which were used to estimate the systematic uncertainty in the background subtraction. Since there is no stable $^5Li$ ground state, the energy spectra for stable $^6Li$ were used as input to the efficiency calculation [Chen 88]. Therefore, the extracted population probability in Table 5.2 is relative to the $^6Li$ stable yield and has no meaning by itself. It obtains its meaning when it is compared to the population probability for the $^5Li$ excited state at $E^* = 16.66$ MeV. In this comparison, the uncertainty of the efficiency calculation due to lack of stable $^5Li$ energy spectra largely cancels out.

$$^5\boldsymbol{Li} \rightarrow \boldsymbol{d} + {}^3\boldsymbol{He}$$

The excited state of $^5$Li nuclei at 16.66 MeV decays to a deuteron and a $^3He$. The impact parameter selected $d - ^3He$ correlation functions are shown in Figure 5.14. The left panel shows the spectrum for peripheral collisions and the right panel shows the spectrum for central collisions. The peak near threshold is from the decay of the 16.66 MeV excited state with spectroscopic parameters $J^\pi = \frac{3}{2}^+, \Gamma = 0.20$ MeV, $\Gamma_p/\Gamma = 0.86$. The R-matrix formalism is used to fit the excited state yield and extract the population probability. The related R-matrix parameters are, $E_\lambda = 129$ KeV, $\gamma^2(d) = 780$ KeV, $l_d = 0, a_d = 7$ fm, $\gamma^2(p) = 12$ KeV, $l_p = 2, a_p = 7$ fm, with boundary condition parameters $B_d = B_p = 0$. In order to fit the excitation energy spectrum, it is necessary to shift the peak 150 KeV higher in excitation energy. This shift may reflect 3-body distortions of the line shape due to Coulomb final state interaction with the target residue. Such effects are large in the decay products

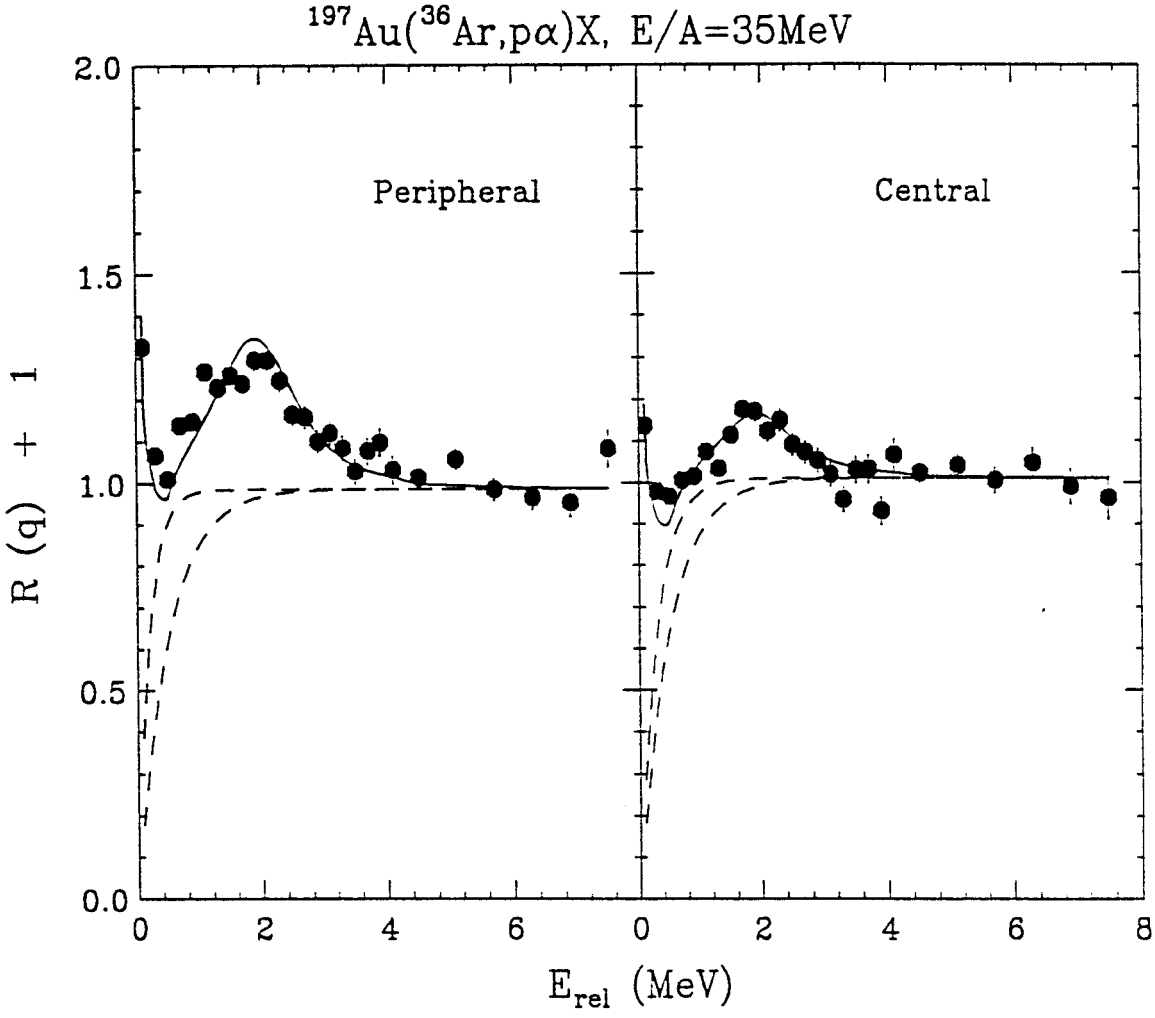


Figure 5.13: The $p-\alpha$ correlation function measured in the $^{36}$Ar + $^{197}$Au reaction at E/A=35 MeV. The spectra obtained for peripheral and central collisions are shown on the left and right hand sides, respectively. The solid lines depict the best fit to the data, and the dashed lines depict extreme assumptions about the background used to estimate the systematic uncertainties due to background subtraction.

which have different charge to mass ratios [Poch 86]. Another wide excited state at $E^* = 20$ MeV were also included in the fit, but not analyzed further. Again, since there is no stable $^5Li$ ground state, the $^6Li$ energy spectrum were used as input to the efficiency calculation [Chen 88]. The extracted population probability in Table 5.2 for the 16.66 MeV excited state can then be compared to the population probability for the ground state of $^5$Li to extract an *apparent* temperature, which are shown as solid points in Figure 5.18 for both peripheral and central collision gates. In this fashion, the uncertainty of the efficiency calculation due to the lack of an energy spectrum for $^5Li$ will be canceled out.

$$^6Li \rightarrow d + \alpha$$

The impact parameter selected correlation functions for the decay $^6Li \rightarrow d + \alpha$ is shown in Figure 5.15. The left panel is the data gated on peripheral collisions and the right panel is the data gated on the central collisions. The peak at $E_{rel} \approx 0.71$ MeV is from the decay of the $^6Li$ excited state at $E^* = 2.186$ MeV with spectroscopic parameters $J^\pi = 3^+, \Gamma = 0.024$ MeV, $\Gamma_c/\Gamma = 1.0$. Also included in the fit is the broad peak at $E \approx 3$ MeV, which is from the overlap of two resonances at 4.31 MeV ($\Gamma = 1.7$ MeV, $J^\pi = 2^+$, $\Gamma_\alpha/\Gamma = 0.97$), and 5.65 MeV ($\Gamma = 1.5$ MeV, $J^\pi = 1^+$, $\Gamma_\alpha/\Gamma = 0.74$). We include the line shape distortions caused by the Boltzman factor $exp(-E/T)$, with $T = 4$ MeV, in the fit to fit the broad peak better. The solid line depicts the best fit to the data using the Breit-Wigner formalism. The two dashed lines indicate two extreme assumptions for the background which are used to estimate the systematic uncertainty in the fit. The energy spectra for stable $^6Li$ fragments are used for the efficiency calculation. The population probability in Table 5.2 is defined relative to the yield of stable $^6Li$ nuclei. Apparent temperatures extracted from the first peak are shown in Figure 5.18 as solid points for both central and peripheral

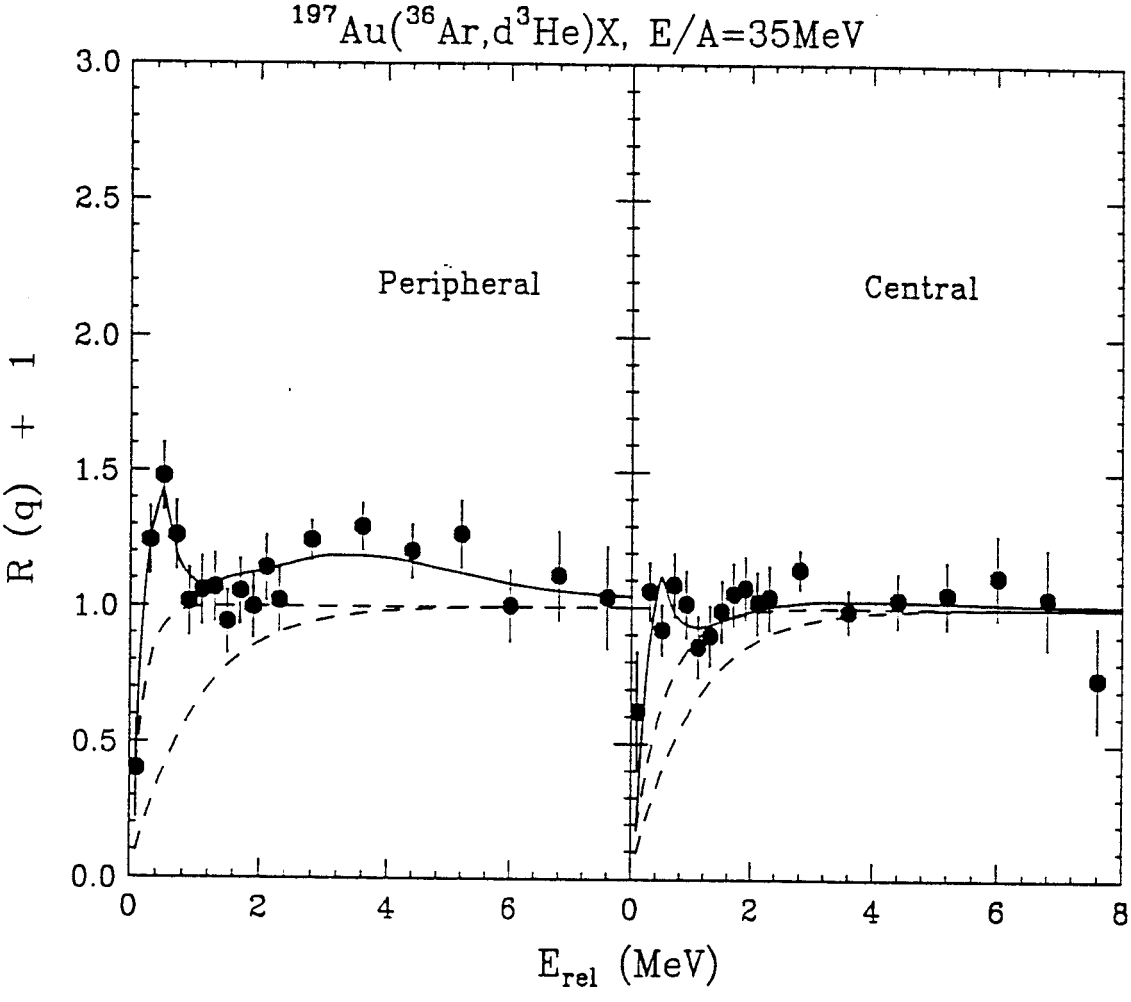


Figure 5.14: The $d-^3He$ correlation function measured in the $^{36}Ar + ^{197}Au$ reaction at E/A=35 MeV. The spectra obtained for peripheral and central collisions are shown on the left and right hand sides, respectively. The solid lines depict the best fit to the data, and the dashed lines depict extreme assumptions about the background used to estimate the systematic uncertainties due to background subtraction.

collision gates. The population probabilities for the pair of states at $E_{rel} \approx 3$ MeV were statistically insignificant and were not analyzed further.

$$^{7}Be \rightarrow {}^{3}He + \alpha$$

The impact parameter selected correlation function for the decay $^{7}Be \rightarrow {}^{3}He + \alpha$ are shown in Figure 5.16. The left panel is gated on peripheral collisions and the right panel is gated on central collisions. The R-matrix formula was used to fit the peak at $E^* = 4.57$ MeV, with $J^\pi = \frac{7}{2}^-, \Gamma = 0.175$ MeV, $\Gamma_c/\Gamma = 1.0$. The relevant R-matrix parameters are, $E_\lambda = 3.855$ KeV, $\gamma^2(\alpha) = 1.595$ MeV, $l_\alpha = 3, a_\alpha = 4$ fm, $B_\alpha = -3$. At slightly higher energies are two peaks at $E^* = 6.73$ MeV, with $J^\pi = \frac{5}{2}^-, \Gamma = 1.2$ MeV, $\Gamma_c/\Gamma = 1.0$, and $E^* = 7.21$ MeV, with $J^\pi = \frac{5}{2}^-, \Gamma = 0.5$ MeV, $\Gamma_c/\Gamma = 0.03$. These two peaks are analysed with the two level R-matrix formula [Naya 92]. The parameters for the $E^* = 6.73$ MeV level are, $E_\lambda = 9.007$ MeV, $\gamma^2(\alpha) = 3.1$ MeV, $l_\alpha = 3, a_\alpha = 4$ fm, and for the $E^* = 7.21$ MeV level are, $E_\lambda = 5.993$ MeV, $\gamma^2(\alpha) = 0.023, l_\alpha = 3, a_\alpha = 4$ fm, $\gamma^2(p) = 1.2, l_p = 1, a_p = 4$ fm. Both sets of parameters were determined by using the boundary conditions $B_\alpha = -3$ and $B_p = -1$ [spig 67, Bark 72]. The energy spectra for stable $^{7}Be$ nuclei were used to calculate the efficiency functions. The population probabilities for the $^{7}Be$ excited state at $E^* = 4.57$ in Table 5.2 are defined relative to the yield of stable $^{7}Be$ nuclei. These population probabilities were used to extract an apparent temperature shown in Figure 5.18 as solid points for both central and peripheral collision gates. The population probabilities for the pair of states at $E^* \approx 7$ MeV were statistically insignificant and were not analyzed further.

$$^{7}Be \rightarrow p + {}^{6}Li$$

The impact parameter selected correlation function for the decay of $^{7}Be \rightarrow p + {}^{6}Li$ are shown in Figure 5.17. The left panel is the data gated on peripheral collisions

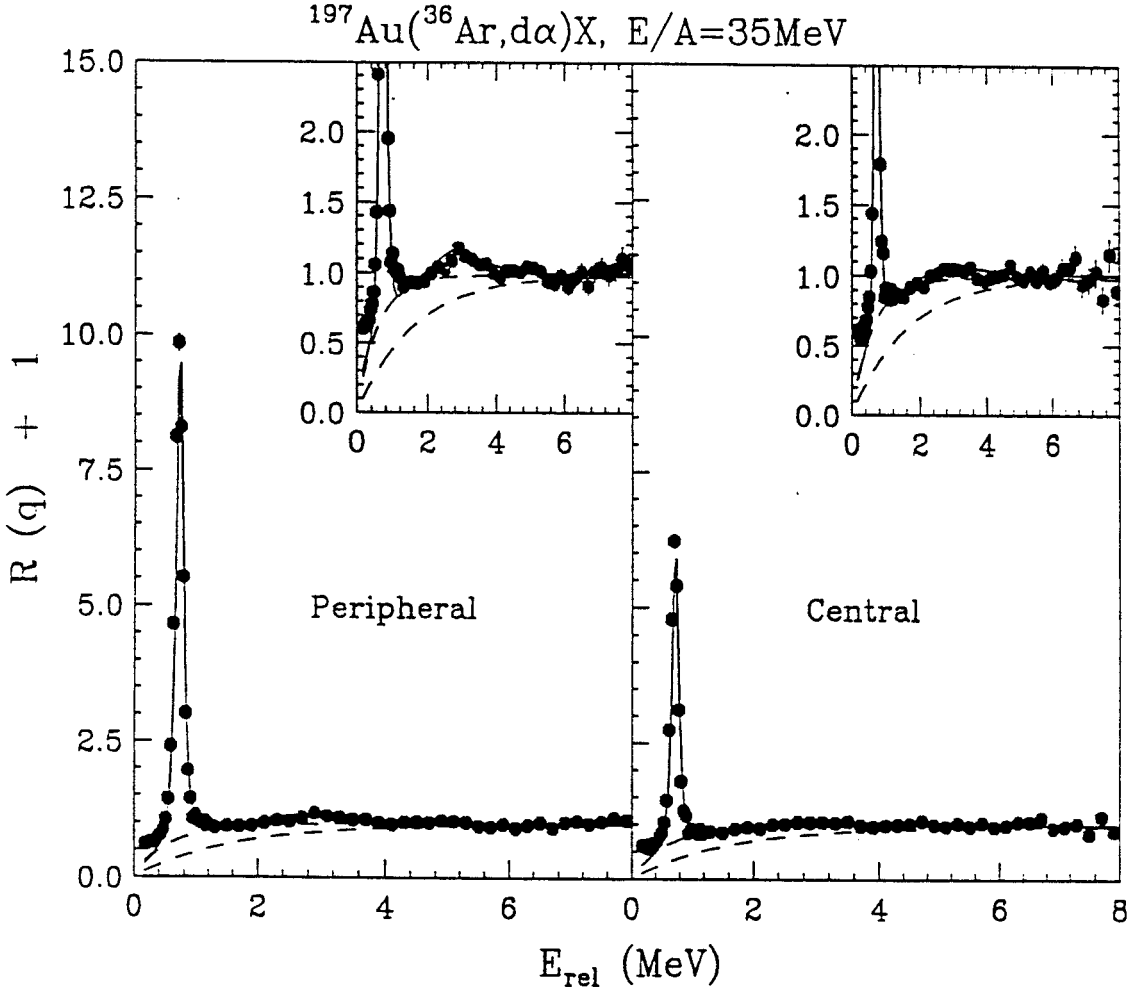


Figure 5.15: The correlation function of $d$+$\alpha$ measured in the $^{36}$Ar + $^{197}$Au reaction at E/A=35 MeV. The spectra obtained for peripheral and central collisions are shown on the left and right hand sides, respectively. The dotted lines are the estimated background and the solid lines are the fits to the data explained in the text.

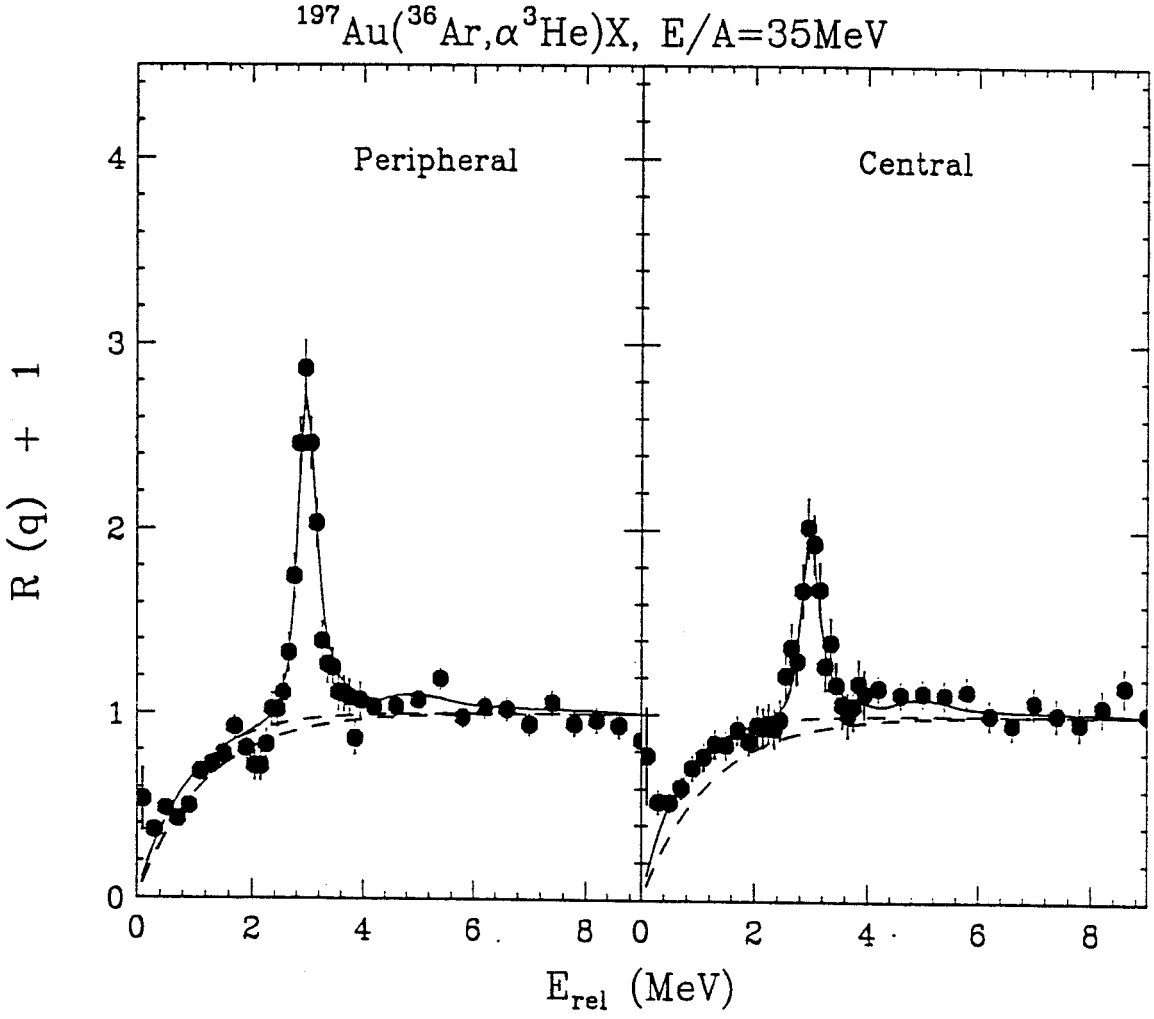


Figure 5.16: The $^3He-\alpha$ correlation function measured for the $^{36}$Ar + $^{197}$Au reaction at E/A=35 MeV. The spectra obtained for peripheral and central collisions are shown on the left and right hand sides, respectively. The solid lines depict the best fit to the data, and the dashed lines depict extreme assumptions about the background used to estimate the systematic uncertainties due to background subtraction.

and the right panel is the data gated on central collisions. The peak at $E_{rel} \approx 1.6$ MeV is from the decay of the $^7Be$ excited state at $E^* = 7.21$ MeV with the spectroscopic parameters $J^\pi = \frac{5}{2}^-, \Gamma = 0.5$ MeV, $\Gamma_p/\Gamma = 0.97$. The Breit-Wigner formula is used to fit the energy spectrum. The energy spectra for stable $^7Be$ fragments are used to calculate the efficiency functions and the extracted population probabilities are given in Table 5.2. The population probabilities in Table 5.2 for $^7Be^*$ excited state at $E^* = 7.21$ are compared with $^7Be$ stable yields, and also with the population probability of the state at $E^* = 4.57$, to obtain the apparent temperatures for central and peripheral collision gates, shown in Figure 5.18 as solid points.

Obviously, the apparent temperatures shown in Figure 5.18 are not all equal. Some modifications of population probabilities and apparent temperatures are expected due to the sequential feeding of these states by heavier particle unstable fragments. To see what value of the initial temperature of the sequential decay calculation will best fit the overall measurement, we calculated the $\chi^2_\nu(T)$ defined by,

$$\chi^2_\nu(T) = \frac{1}{\nu}\sum_{i=1}^{\nu} \frac{(T_{exp,i} - T_{cal,i}(T))^2}{\sigma^2_{exp,i} + \sigma^2_{cal,i}}. \tag{5.3}$$

Here the summation is over the five measured apparent temperatures. $T_{exp,i}$ is the apparent temperature calculated from the experimental data and shown as the solid points in Figure 5.18. T is the initial temperature of the sequential decay calculation and $T_{cal,i}(T)$ is the apparent temperature calculated in analogy to the experimental apparent temperature $T_{exp,i}$, using the final calculated population probabilities. $\sigma^2_{exp,i}$ is the experimental uncertainties, and $\sigma^2_{cal,i}$ is the theoretical uncertainties due to the unknown spin and parities. Figure 5.19 is the plot of $\chi^2(T)$ as a function of T, the initial freezout temperature assumed in the sequential decay calculations. The upper panel is for the central collision gate and the lower panel is for the peripheral gate. The $\chi^2(T)$ has its minimum between 4-5 MeV for central collision gate. The

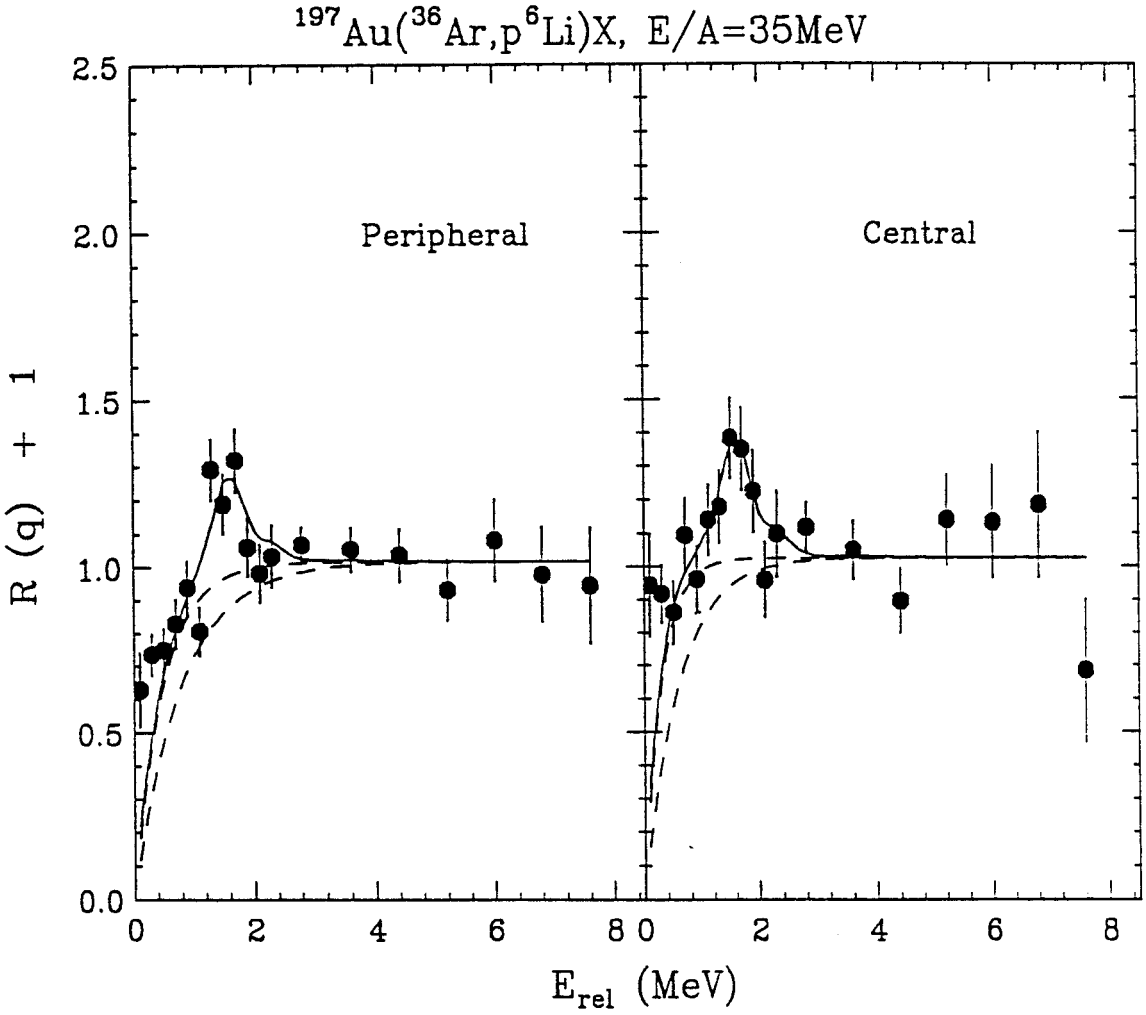


Figure 5.17: The $p-^6Li$ correlation function measured for the $^{36}$Ar + $^{197}$Au reaction at E/A=35 MeV. The spectra obtained for peripheral and central collisions are shown on the left and right hand sides, respectively. The solid lines depict the best fit to the data, and the dashed lines depict extreme assumptions about the background used to estimate the systematic uncertainties due to background subtraction.

minimum for peripheral gate is at 3-4 MeV. The minimum of $\chi^2(T)$ function for central collision gate is smaller than for the peripheral gate, meaning the measured data from the central collisions deviates less from an initially equilibrated system than the peripheral collisions. Greater equilibration for the central collisions is in agreement with the conclusions derived from the excited states of $^{10}$B nuclei discussed in the previous section.

In Figure 5.18, we plot as the open points, the predictions of the sequential decay calculations for the apparent temperatures for an initial temperature of T = 4 MeV as the open points. The error bars here corresponds to a range of calculated values for 12 calculations for different assumptions about the unknown spins and parities of excited states included in the calculation. Clearly, this figure also shows that the calculations are in better agreement with data for central collisions than for peripheral collisions. Again, this observation is consistent with the trend observed for $^{10}B$ excited states.

To summarize all the comparisons between measurements and calculations for the excited states of intermediate mass fragments emitted in the $^{36}Ar + ^{197}Au$ reaction at E/A=35 MeV, we plot both $\chi^2_\nu$ analysis from Figure 5.12 and 5.19 in Figure 5.20. The open circles are for $^{10}B$ excited states, the solid squares are for $^{5,6}Li$ and $^{7}Be$ excited states. The upper panel is for central collisions and the lower panel is for peripheral collisions. For central collisions, both $\chi^2_\nu$ analysis yield minima for $T \approx 4-5$ MeV. The overall value for $\chi^2_\nu$ are close to one, indicating that the experimental and theoretical excited state populations are close to being in statistical agreement. In contrast, the minimum for $^{10}B$ excited state populations in peripheral collisions occurs at $T \approx 5$ MeV. For $^{5,6}Li$ and $^{7}Be$ excited states, the minimum occurs at 3-4 MeV. The overall $\chi^2_\nu$ for peripheral collisions are rather large, indicating a significant disagreement between theoretical and experimental population probabilities.

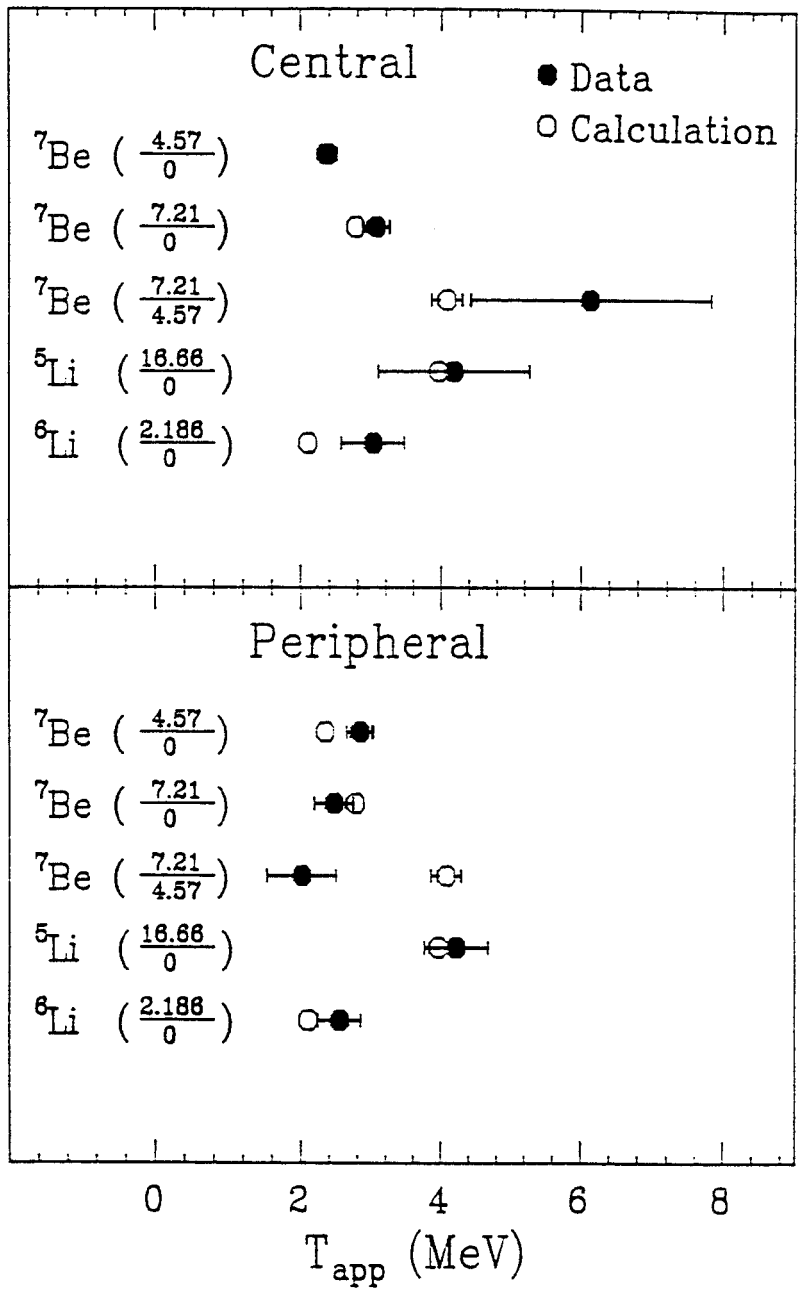


Figure 5.18: The compilation of extracted temperatures of $^{6}$Li, $^{5}$Li, and $^{7}$Be nuclei in the reaction of $^{36}$Ar + $^{197}$Au at E/A=35 MeV with peripheral(lower) and central(upper) collisions gate. The solid points are experimental measurements and the open points are the results of sequential decay calculation for an initial temperature of T = 4 MeV.

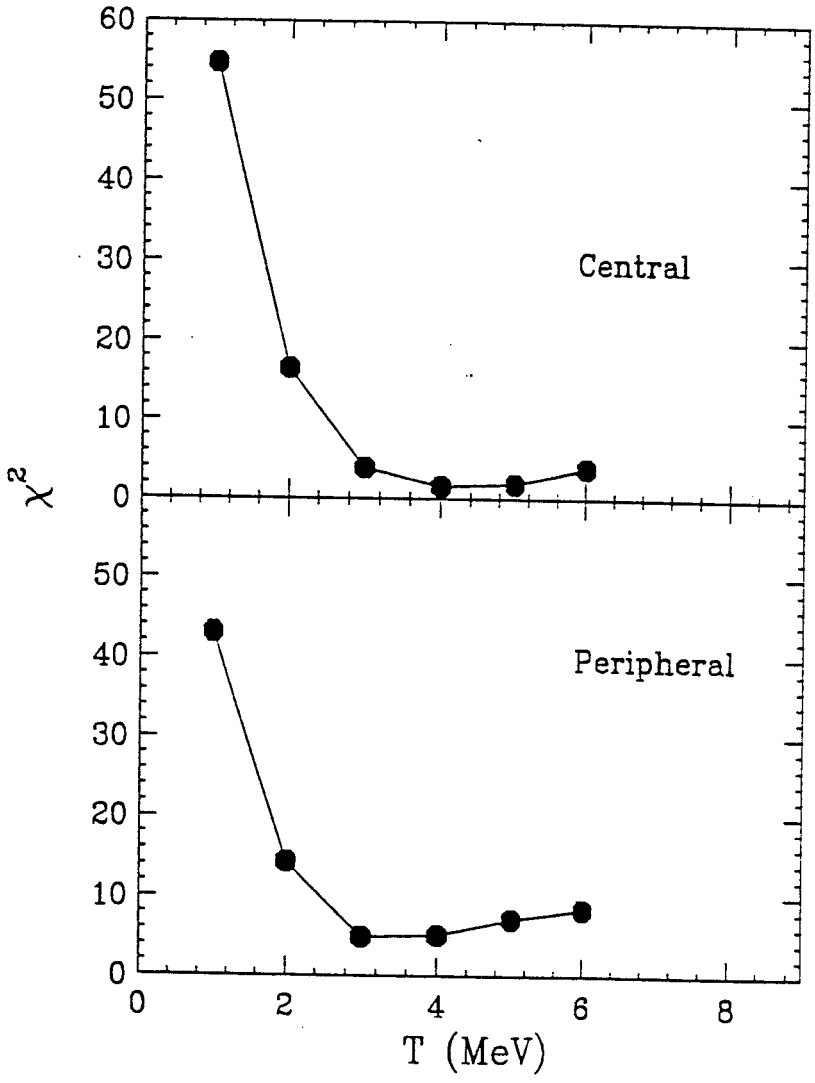


Figure 5.19: The $\chi^2(T)$ as a function of T from Equation 5.3 for the reaction of $^{36}$Ar + $^{197}$Au at E/A=35 MeV with peripheral(lower) and central(upper) collisions gate. The lines are drawn to guild the eye.

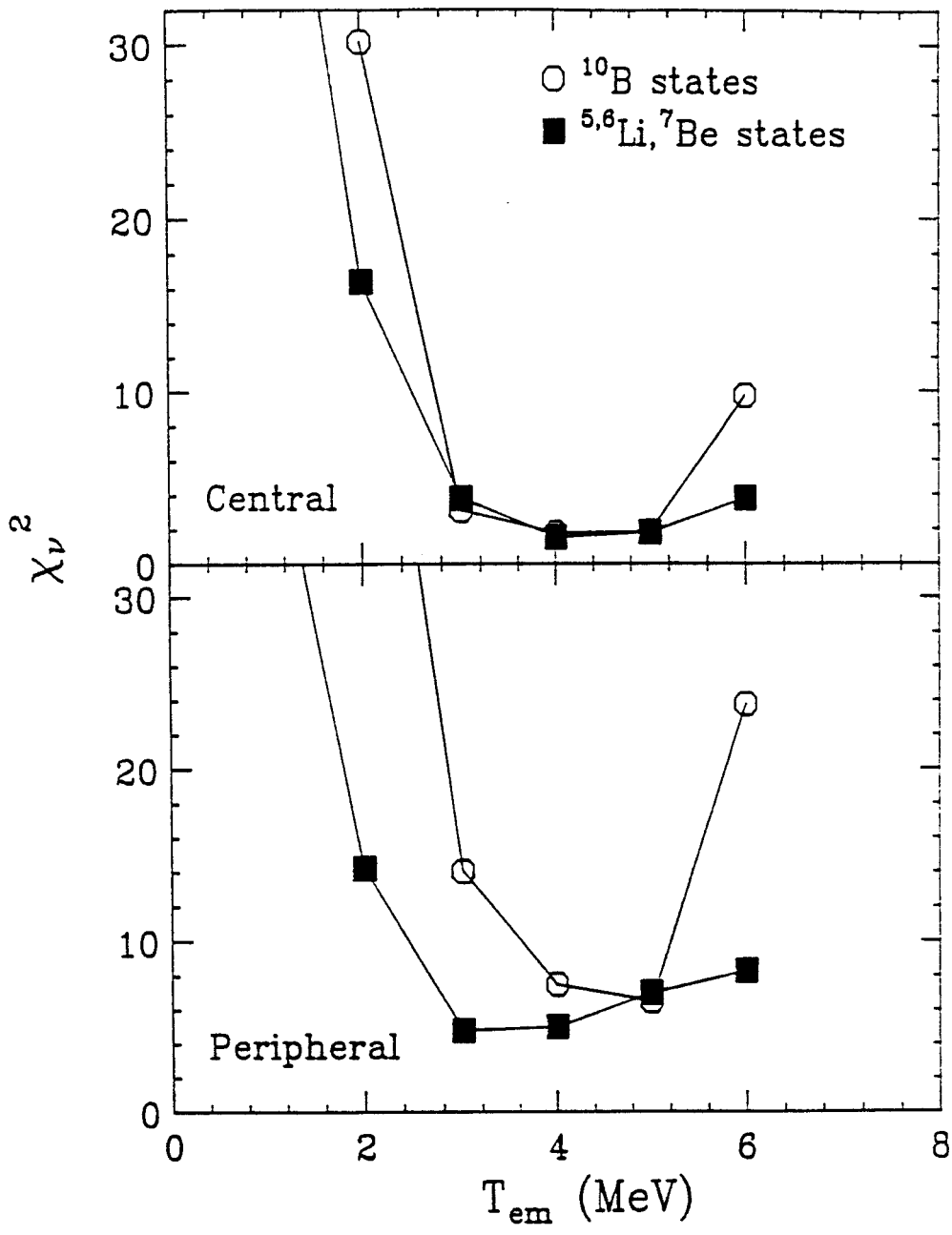


Figure 5.20: The $\chi^2(T)$ as a function of T from Figure 5.12 and Figure 5.19 for the reaction of $^{36}$Ar + $^{197}$Au at E/A=35 MeV with peripheral(lower) and central(upper) collisions gate. The lines are drawn to guild the eye.

To summarize this chapter, the impact parameter dependence of excited state populations of intermediate mass fragments has been investigated with a $4\pi$ charged particle array. Non-statistical populations, indicative of non-thermal excitation mechanisms, are observed in peripheral collisions characterized by low associated charged particle multiplicities. These effects largely disappear for central collisions, consistent with a trend towards greater thermalization as the complexity of the breakup configuration is increased. The remaining discrepancies observed in central collisions, however, indicate that the limit of local equilibrium has not yet been observed.

Table 5.2: Spectroscopic information for $^{5,6}Li$, $^{7}Be$, and $^{10}B$ isotopes which was used to extract excited state populations. Branching ratios are given in percentage. The group structure and population probabilities $n_\lambda$ are explained in the text. The $n_\lambda(P)$ are for peripheral collisions and $n_\lambda(C)$ are for central collisions.

| | G | E*(MeV) | J$^\pi$ | $\Gamma_c$(MeV) | Decay | $\Gamma_c/\Gamma$ | $n_\lambda(P)$ | $n_\lambda(C)$ |
|---|---|---|---|---|---|---|---|---|
| $^5$Li | 1 | g.s | $\frac{3}{2}^-$ | 1.5 | $\alpha - p$ | 100 | $0.325 \pm 0.041$ | $0.212 \pm 0.085$ |
| | 2 | 16.66 | $\frac{3}{2}^+$ | 0.20 | $^3He - d$ | 86 | $6.25 \times 10^{-3} \pm 2.55 \times 10^{-3}$ | $3.93 \times 10^{-3} \pm 3.77 \times 10^{-3}$ |
| $^6$Li | 1 | 2.186 | $3^+$ | 0.024 | $\alpha - dp$ | 100 | $0.173 \pm 4.4 \times 10^{-3}$ | $0.152 \pm 6.3 \times 10^{-3}$ |
| $^7$Be | 1 | 4.57 | $\frac{7}{2}^-$ | 0.175 | $^3He - \alpha$ | 100 | $0.0497 \pm 1.6 \times 10^{-3}$ | $0.0364 \pm 1.1 \times 10^{-3}$ |
| | 2 | 6.73 | $\frac{5}{2}^-$ | 1.2 | $^3He - \alpha$ | 100 | $0.0134 \pm 4.2 \times 10^{-3}$ | $0.0237 \pm 2.8 \times 10^{-3}$ |
| | | 7.21 | $\frac{5}{2}^-$ | 0.5 | $^3He - \alpha$ | 3 | | |

| | G | E*(MeV) | J$^\pi$ | $\Gamma_c$(KeV) | Decay | $\Gamma_c/\Gamma$ | $n_\lambda(P)$ | $n_\lambda(C)$ |
|---|---|---|---|---|---|---|---|---|
| $^{10}$B | 1 | 4.774 | $3^+$ | 0.0084 | $^6Li - \alpha$ | 100 | $0.0144 \pm 0.66 \times 10^{-3}$ | $0.0148 \pm 1.1 \times 10^{-3}$ |
| | 2 | 5.1103 | $2^-$ | 0.98 | $^6Li - \alpha$ | 100 | $0.0122 \pm 0.66 \times 10^{-3}$ | $0.0132 \pm 1.1 \times 10^{-3}$ |
| | | 5.1639 | $2^+$ | 0.00176 | $^6Li - \alpha$ | 13 | | |
| | | 5.10 | $1^+$ | 110 | $^6Li - \alpha$ | 100 | | |
| | 3 | 5.9195 | $2^+$ | 6 | $^6Li - \alpha$ | 100 | $0.0177 \pm 1.1 \times 10^{-3}$ | $0.0133 \pm 0.99 \times 10^{-3}$ |
| | | 6.0250 | $4^+$ | 0.05 | $^6Li - \alpha$ | 100 | | |
| | | 6.1272 | $3^-$ | 2.36 | $^6Li - \alpha$ | 97 | | |
| | 4 | 6.56 | $4^-$ | 25.1 | $^6Li - \alpha$ | 100 | $0.00924 \pm 1.2 \times 10^{-3}$ | $0.00814 \pm 1.21 \times 10^{-3}$ |
| | 5 | 7.430 | $2^-$ | 100 | $^9Be - p$ | 70 | $0.00726 \pm 0.96 \times 10^{-3}$ | $0.00693 \pm 0.99 \times 10^{-3}$ |
| | | 7.467 | $1^+$ | 65 | $^9Be - p$ | 100 | | |
| | | 7.478 | $2^+$ | 74 | $^9Be - p$ | 65 | | |
| | | 7.5599 | $0^+$ | 265 | $^9Be - p$ | 100 | | |

# Chapter 6

# Summary and Conclusions

In this thesis, we have measured two particle correlation function and excited state populations for $^3He+Ag$ reactions at $E_{beam}$ = 200 MeV, and $^{36}Ar+^{197}Au$ reactions at $E/A$ = 35 MeV. Two-proton correlation functions measured for $^3$He induced reactions on Ag at $E_{beam}$ = 200 MeV increase dramatically with the energy of the detected protons. Consistent with other correlation function data, these measurements suggest that the spatial extent of the emitting region is governed initially by the overlap of the projectile with the target. For proton energies less than 50 MeV, the measured correlation functions gated on the proton energies, are consistent with those predicted by the Boltzmann-Uehling-Uhlenbeck equation. This suggests that the localization in spacetime of the emission of protons with these energies is reasonably well described by the model. The correlation functions of more energetic protons are underpredicted by the model, an effect which may reflect remnant spin correlations from the ground state of the $^3$He projectile. The source radii extracted from two proton correlation functions has been compared with other projectile induced reactions. This comparison suggests a natural scaling of the correlation functions for energetic protons with the projectile mass. The extracted source size scale with the projectile radius, $A_{proj}^{1/3}$ [Zhu 91]. The source radii extracted for low energy protons, however, do not follow this scaling relationship because of a large contributions from evaporative processes

which have large source lifetimes. Thus one might expect that correlation functions which have large contributions from evaporative processes would not be sensitive to the source radius. This may explain why the measured correlation functions for proton and $^{14}N$ induced reactions on Ag at incident energies of 500 MeV, which included all protons above the detection threshold, showed no sensitivity to the projectile radius [Cebr 89].

The gaussian source radii extracted from d-$\alpha$ correlation functions have also been compared with other measurements, and a similar scaling relation have been obtained. This scaling relationship was actually obtained from the scaling relationship for p-p correlation functions and simply multiplied by a factor of 0.7. This scaling factor, 0.7, may reflect the fact that the mean free paths for deuterons and alpha particles in the nuclear medium are somewhat shorter than the mean free paths for protons. This would make the effective source volume for emission of these two particles smaller. The source radii for $d - \alpha$ correlation functions follow the scaling line quite nicely, even at low energies, in contrast to the p-p correlation systematics, where the data at low energies deviate significantly from the scaling trend. This may reflect the fact that the contributions to the deuteron spectra from evaporative processes are smaller than for protons.

In this thesis experiment, we also measured excited state populations for $^5Li$ and $^6Li$ nuclei. At forward angles, where pre-equilibrium processes were dominant, the extracted emission temperature from the excited state populations was about 4 MeV, consistent with the 3-5 MeV range established from the systematic studies of excited state populations [Chen 88]. At backward angles, the extracted emission temperature was about 1 MeV, corresponding to a relatively cold target-like residue. This latter result is consistent with the predictions of the quasiparticle dynamics model.

For my second thesis measurement of $^{36}Ar + ^{197}Au$ reactions at $E/A = 35$ MeV,

we investigated the impact parameter dependence of excited state populations for intermediate mass fragments using the high resolution hodoscope and the Miniball $4\pi$ charged particle array. A strong population inversion, indicative of non-thermal excitation mechanisms, was observed for excited states of $^{10}B$ nuclei measured for peripheral collisions characterized by low associated charged particle multiplicities. This results is consistent with the observations previously reported for the $^{14}N + Ag$ reactions at $E/A = 35$ MeV [Naya 89, Naya 92], which motivated this measurement. These population inversions largely disappear for central collisions, consistent with a trend towards greater thermalization as the complexity of the breakup configuration is increased. Small discrepancies between measured and calculated population probabilities observed for central collisions indicate that the limit of local equilibrium has not yet been observed [Zhu 92].

Additional comparisons of experimental and calculated population probabilities were made for $^{5,6}Li$, and $^{7}Be$ fragmentation products. As observed for the $^{10}B$ excited states, the difference between measured and calculated population probabilities were smaller for central collisions than for peripheral collisions. This suggest a general trend of greater thermalization in central collisions than in peripheral collisions.

Impact parameter selected deuteron-alpha correlation functions have also been measured in this reaction by gating on the charged particle multiplicity. The extracted source size from $d - \alpha$ correlation functions is larger for central collisions than those observed for peripheral collisions. This is consistent with the trends predicted by the participant spectator model and by BUU simulations [Goss 77, Gong 91].

# Bibliography


[Abbo 90] T. Abbott et al, E802 collaboration, Phys. Rev. Lett. **64**, 847 (1990).

[Agak 87] G.N. Agakishiyev et al, Z. Phys. **A327**, 443 (1987).

[Awes 81] T.C. Awes, G. Poggi, C.K. Gelbke, B.B. Back, B.G. Glagola, H. Breuer, and G.D. Westfall Phys. Lett. **103b** (1981) 417.

[Awes 84] T.C. Awes, R.L. Ferguson, R. Novotny, F.E. Obenshain, F. Plasil, S. Pontoppidan, V. Rauch, G.R. Young, and H. Sann, Phys. Rev. Lett. 52 (1984) 251.

[Awes 88] T.C. Awes et al, Phys. Rev. Lett. **61**, 2665 (1988).

[Ajze 87] F. Ajzenberg-Selove, Nucl. Phys. **A475** (1987) 1; **A413** (1984) 1; **A433** (1985) 1; **A449** (1986) 1; **A460** (1986) 1.

[Bark 62] F.C. Barker, P.B. Treacy, Nucl. Phys. **38** (1962) 33.

[Bark 63] F.C. Barker et. al. Nucl. Phys. **45** (1963) 449.

[Bark 72] F.C. Barker, Aust. J. Phys. **25** (1972) 341.

[Baue 88] W. Bauer, Michigan State University report MSUCL-699.

[Bern 85] M.A. Bernstein, W.A. Friedman, W.G. Lynch, C.B. Chitwood, D.J. Fields, C.K. Gelbke, M.B. Tsang, T.C. Awe, R.L. Ferguson, F.E. Obenshain, F. Plasil, R.L. Robinson, and G.R. Young, Phys. Rev. Lett. **54** (1985) 402.

[Bert 84] G.F. Bertsch, H. Kruse, and S. Das Gupta, Phys. Rev. **C29**, 673 (1984).

[Bert 88] G.F. Bertsch and S. Das Gupta, Phys. Rep. **160**, 189 (1988).

[Bloc 87] C. Bloch, W.Benenson, A.I. Galonsky, E. Kashy, J. Heltsley, L. Heilbronn, M. Lowe, B. Remington, D.J. Morrissey, J. Kasagi Phys. Rev. **C36** (1987) 203

[Bohr 36] N. Bohr, Nature **137** (1936) 344.

[Boal 86] D.H. Boal and J.C. Shillcock, Phys. Rev. **C33** (1986). 549

[Boal 88] D. Boal, J. Glosli, Phys. Rev. **C37** (1988) 91.

[Boal 88a] D. Boal, J. Glosli, Phys. Rev. **C38** (1988) 1870; Phys. Rev. **C38** (1988) 2621.

[Boal 89] D. Boal, J. Glosli, and C. Wicentowich, Phys. Rev. **C40** (1989) 601.

[Boal 90a] D. Boal, J. Glosli, Phys. Rev. **C42** (1990) R502.

[Boal 90b] D.H. Boal, C.K. Gelbke and B.K. Jennings, Rev. Mod. Phys. **62** (1990) 553

[Bond 83] P.D. Bond and R.J. de Meijer, Phys. Rev. Lett. **52** (1984) 3201.

[Bond 85] J.P. Bondorf, R. Donangelo, L.N. Mishustin, C.J. Pethick, H.Schulz and K. Sneppen, Nucl. Phys. **A443** (1985) 321.

[Bowm 91] D.R. Bowman, G.F. Peaslee, R.T. de Souza, N. Carlin, C.K. Gelbke, W.G. Gong, Y.D. Kim, M.A. Lisa, W.G. Lynch, L. Phair, M.B. Tsang, C. Williams, Phys. Rev. Lett. **67** (1991) 1527.

[Cebr 89] D.A. Cebra, W. Benenson, Y. Chen, E. Kashy, A. Pradhan, A. Vandermolen, G.D. Westfall, W.K. Wilson, D.J. Morrisey, R.S. Tickle, R. Kortelling, and R.L. Helmer, Phys. Lett. **B227** (1989) 336.

[Chen 87a] Z. Chen, C.K. Gelbke, W.G. Gong, Y.D. Kim, W.G. Lynch, M.R. Maier, J. Pochodzalla, M.B. Tsang, F. Saint-Laurent, D. Ardouin, H. Delagrange, H. Doubre, J. Kassagi, A. Kyanowski, A. Peghaire, J. Peter, E. Rosato, G. Bizard, F. Lefebvres, B. Tamain, J. Quebert, and Y.P. Viyogi, Phys. Lett. **B199** (1987) 171.

[Chen 87b] Z. Chen, C.K. Gelbke, W.G. Gong, Y.D. Kim, W.G. Lynch, M.R. Maier, J. Pochodzalla, M.B. Tsang, F. Saint-Laurent, D. Ardouin, H. Delagrange, H. Doubre, J. Kassagi, A. Kyanowski, A. Peghaire, J. Peter, E. Rosato, G. Bizard, F. Lefebvres, B. Tamain, J. Quebert, and Y.P. Viyogi, Phys. Rev. **C36** (1987) 2297.

[Chen 88] Z. Chen , Thesis, Michigan State University.

[Chit 86] C.B. Chitwood, C.K. Gelbke, J. Pochodzlla, Z. Chen, D.J. Fields, W.G. Lynch, R. Morse, M.B. Tsang, D.J. Boal, and J.C. Shillcock, Phys. Lett. **B172** 27 (1986).

[Chit 86a] C.B. Chitwood, D.J. Fields, C.K. Gelbke, D.R. Klesch, W.G. Lynch, M.B. Tsang, T.C. Awes, R.L. Ferguson, F.E. Obenshain, F. Plasil, R.L. Robinson, and G.R. Young, Phys. Rev. **C34** (1986) 858

[Cser 86] L.P. Csernai, and J.I. Kapusta, Phys. Rep. **131** (1986) 223, and references contained therein.

[DeYo 90] P.A. DeYoung, C.J.Gelderloos, D. Kortering, J.Sarafa, K. Vienert, M.S. Gordon, B.J. Fineman, G.P. Gilfoyle, X. Lu, R.L. McGrath, D.M. de

Castro Rizzo, J.M. Alexander, G. Auger, S. Kox, L.C. Vaz, C. Beck, D.J. Henderson, D.G. Kovar, and M.F. Vineyard, Phys. Rev. **C41** (1990)R1885

[Doss 85] T. Dssing and J. Randrup, Nucl. Phys. **A433** (1985) 215; **A433** (1985) 280.

[Faty 87] M. Fatyga et al. Phys. Rev. Lett. **58** (1987) 192527.

[Fiel 84] D.J. Fields, W.G. Lynch, C.B. Chitwood, C.K. Gelbke, M.B. Tsang, H. Utsunomiya, and J. Aichelin, Phys. Rev. **C30** (1984) 1912.

[Frid 83] W.A. Fridman, and W.G. Lynch Phys. Rev. **C28** (1983) 16

[Frid 88] W.A. Fridman Phys. Rev. Lett. **60** (1988) 2125

[Frid 90] W.A. Fridman Phys. Rev. **C42** (1990) 667.

[Fung 78] S.Y. Fung, W. Gorn, G.P. Kiernan, J.J. Lu, T.T. Oh, and T.T. Poe, Phys. Rev. Lett. **41** (1978) 1592.

[Gelb 87] C.K. Gelbke, and D.H. Boal, Prog. Part. and Nucl. Phys. **19** (1987) 33. and references contained therein.

[Gilb 65a] A. Gilbert, F.S. Chen, A.G.W. Cameron, Canadian Jour. of Phys., **43** (1965) 1248.

[Gilb 65b] A. Gilbert, A.G.W. Cameron, Canadian Jour. of Phys., **43** (1965) 1446.

[Gold 60] G. Goldhaber, S. Golhaber, W. Lee, and A. Pais, Phys. Rev. **120** (1960) 300.

[Gong 91] W.G. Gong, W. Bauer, C.K. Gelbke, and S. Pratt, Phys. Rev. **C43** 781. (1991).

[Gong 91a] W.G. Gong, C.K. Gelbke, W. Bauer, N. Carlin, R.T. de Souza, Y.D. Kim, W.G. Lynch, T. Murakami, G. Poggi, D.P. Sanderson, M.B. Tsang, H.M. Xu, S. Pratt, D.E. Fileds, K. Kwiatkowski, R. Planeta, V.E. Viola,Jr., and S.J. Yennello, Phys. Rev. **C43** 1804 (1991).

[Gong 90] W.G. Gong, W. Bauer, C.K. Gelbke, N. Carlin, R.T. de Souza, Y.D. Kim, W.G. Lynch, T. Murakami, G. Poggi, D.P. Sanderson, M.B. Tsang, H.M. Xu, S. Pratt, D.E. Fileds, K. Kwiatkowski, R. Planeta, V.E. Viola,Jr., and S.J. Yennello, Phys. Rev. Lett. **65**, 2114 (1990).

[Goss 77] J. Gosset, H.H. Gutbroad, W.G. Meyer, A.M. Poskanzer, A. Sandoval, R. Stock, and G.D. Westfall Phys. Rev. **C16**, (1977) 629.

[Goul 82] F.S. Goulding, and D.A. Landis IEEE Tran. Nucl. Phys. Vol. NS-29, No. 3, **1125** (1982) June

[Goul 75] F.S. Goulding, and B.G. Harvey Annu. Rev. Nucl. Sci., **25** (1975) 167

[Gros 88] D.H.E. Gross, Phys. Lett. **B203** (1988) 26.

[Guer 89] D. Guerreau, "Nuclear Matter and Heavy Ion Collisions", Plenum Press, Nato ASI Series B 205 (1989) 187, and references contained therein.

[Gust 84] H.A. Gustafsson, H.H. Gutbrod, B.Kolb, H. Ludewigt, A.M. Poskanzer, T. Renner, H. Riedesel, G.G. Ritter, A. Warwick, F. Weik, and H. Wieman Phys. Rev. Lett. **53** (1984) 544.

[Haus 52] W. Hauser and H. Feshbach, Phys. Rev. **87** (1952) 366.

[HBT 56] R. Hanbury-Brown and R.Q. Twiss, Nature **178** (1956) 1046.

[Huan 63] K. Huang, Statistical Mechanics Wiley, New York, (1963) 310

[Jenn 86] B.K. Jennings, D.H. Boal, and J.C. Schillcock, Phys. Rev. **C33** (1986) 1303

[Kim 92] Y.D. Kim, R.T. de Souza, D.R. Bowman, N. Carlin, C.K. Gelbke, W.G. Gong, W.G. Lynch, L. Phair, M.B. Tsang, and F. Zhu, Phys. Rev. **C45** (1992) 338.

[Kim 92a] Y.D. Kim Thesis, Michigan State University

[Kim 89] Y.D. Kim, M.B. Tsang, C.K. Gelbke, W.G. Lynch, N. Carlin, Z. Chen, R. Fox, W.G. Gong, T. Murakami, T.K. Nayak, R. M. Ronningen, H.M. Xu, F. Zhu, W. Bauer, L.G. Sobotka, D. Stracener, D.G. Sarantites, Z. Majka, V. Abenate, and H. Griffin, Phys. Rev. Lett. **63** (1989) 494.

[Koon 77] S.E. Koonin, Phys. Lett. **B70** (1977) 43.

[Kopy 74] G.I. Kopylov, Phys. Lett. **B50** (1974) 472.

[Kund 91] G.J. Kund, J. Pochodzalla, J. Aichelin, E. Berdermann, B. Berthier, C. Cerruti, C.K. Gelbke, J. Hubele, P. Kreutz, S. Keray, R. Lucas, U, Lynen, U. Milkau, W.F.J. Muller, C. Ngo, C.H. Pinkenburg, G. Raciti, H. Sann and W. Trautmann Phys. Lett. **B272** (1991) 202.

[Kwia 86] K. Kwiatkowski, J. Bashkin, H. Karwowski, M. Fatyga, and V.E. Viola Phys. Lett. **B171** (1986) 41.

[Land 80] L. Landau, E.M. Lifshitz, Course of Theoretical Physics: Statistical Mechanics Pergamon, New York, (1980) 236

[Lee 90] J. Lee, W. Benenson, and D.J. Morrissey, Phys. Rev. **C41** (1990) 1562. Phys. Rev. **C41** (1990) 2406.

[Levi 84] S. Levit and P. Bonche, Nucl. Phys. **A437** (1984) 426.

[Lisa 91] M.A. Lisa, W.G. Gong, C.K. Gelbke, and W.G. Lynch, Phys. Rev. **C44** (1990) 2865.

[Lync 83] W.G. Lynch, C.B. Chitwood, M.B. Tsang, D.J. Fields, D.R. Klesch, C.K. Gelbke, G.R. Young, T.C. Awe, R.L. Ferguson, F.E. Obenshain, F. Plasil, R.L. Robinson, and A.D. Panagiotou, Phys. Rev. Lett. **51** (1983) 1850.

[Lync 87] W.G. Lynch, Ann. Rev. Nucl. Part. Sci. **37** (1987) 493, and references contained therein.

[Marm 69] P. Marmier and E. Shelton, Physics of Nuclei and Particles, Vol. 1, Academic Press (1969) 38.

[Morr 84] D.J. Morrissey, W. Benenson, E. Kashy, B. Sherrill, A.D. Panagiotou, R.A. Blue, R.M. Ronningen, J. van der Plicht, and H. Utsunomiya, Phys. Lett. **B148** (1984) 423.

[Morr 85] D.J. Morrissey, W. Benenson, E. Kashy, C. Bloch, M. Lowe, R.A. Blue, R.M. Ronningen, B. Sherrill, H. Utsunomiya, and I. Kelson, Phys. Rev. **C32** (1985) 877.

[Mura 89] T. Murakami, T.K. Nayak, W.G. Lynch, K. Swartz, Z. Chen, D.J. Fields, C.K. Gelbke, Y.D. Kim, M.R. Maier, J. Pochodzalla, M.B. Tsang, H.M. Xu, and F. Zhu Nucl. Instr. and Meth. **A275** (1989) 112

[Naya 89] T.K. Nayak, T. Murakami, W.G. Lynch, K. Swartz, D.J. Fields, C.K. Gelbke, Y.D. Kim, J. Pochodzalla, M.B. Tsang, H.M. Xu, F. Zhu, and K. Kwiatkowski, Phys. Rev. Lett. **62** (1989) 1021.

[Naya 90] T.K. Nayak, Thesis, Michigan State University.

[Naya 92] T.K. Nayak, T. Murakami, W.G. Lynch, K. Swartz, D.J. Fields, C.K. Gelbke, Y.D. Kim, J. Pochodzalla, M.B. Tsang, H.M. Xu, F. Zhu, and K. Kwiatkowski, Phys. Rev. C, **C45**, (1992) 132.

[Ogil 91] C.A. Ogilvie, J.C. Adloff, M. Begemann-Blaich, P. Bouissou, J. Hubele, G. Imme, I. Iori, P. Kreutz, G.J. Kunde, S. Leray, V. Lindenstruth, Z. Liu, U. Lynen, R.J. Meijer, U. Milkau, W.F.J. Mller, C. Ng, J. Pochodzalla, G. Raciti, G. Rudolf, H. Sann, A. Schttauf, W. Seidel, L. Stuttge, W. Trautmann, and A. Tucholski, Phys. Rev. Lett. **67** (1991) 1214.

[Phai 92] L. Phair, D.R. Bowman, N. Carlin, R.T. de Souza, C.K. Gelbke, W.G. Gong, Y.D. Kim, M.A. Lisa, W.G. Lynch, G.F. Peaslee, M.B. Tsang, H.M. Xu, and F. Zhu, Phys. Rev. ? (1992) ?. in press.

[Poch 85] J. Pochodzalla, W.A. Friedman, C.K. Gelbke, W.G. Lynch, M.R. Maier, D. Ardouin, H. Delagrange, H. Doubre, C. Gregoire, A. Kyanowski, W. Mittig, A. Peghaire, J. Peter, F. Saint-Laurent, Y.P. Viyogi, B. Zwieglinski, G. Bizard, F. Lefebvres, B. Tamain, and J. Quebert, Phys. Lett. **B199** (1987) 2297.

[Poch 86] J. Pochodzalla et al, Phys. Lett. **B174**, 36 (1986).

[Poch 87] J. Pochodzalla et al, Phys. Rev. **C35**, 1695 (1987).

[Prat87] S. Pratt and M.B. Tsang, Phys. Rev. **C36**, (1987) 2390

[Rand 78] J. Randrup, Nucl. Phys. **A307** (1978) 319; **A327** (1979) 490.

[Reid 68] R.V. Reid, Ann. Phys. 50 (1968) 411

[Shim 79] T. Shimoda, M. Ishihara, K. Nagatani, and T. Nomura, Nucl. Instr. and Meth. **A165** (1979) 261.

[Sobo 83] L.G. Sobotka, M.L. Padgett, G.J. Wozniak, G. Guarino, A.J. Pacheco, L.G. Moretto, Y. Chan, R.G. Stokstad, I. Tserruya, and S. Wald Phys. Rev. Lett. **51** (1983) 2187.

[Souz 90] R.T. de Souza, N. Carlin, Y.D. Kim, J. Ottarson, L. Phair, D.R. Bowman, C.K. Gelbke, W.G. Gong, W.G. Lynch, R.A. Pelak, T. Peterson, G. Poggi, M.B. Tsang, and H.M. Xu, Nucl. Instr. and Meth. **A295** (1990) 109

[Souz 91] R.T. de Souza, L. Phair, D.R. Bowman, N. Carlin, C.K. Gelbke, W.G. Gong, Y.D. Kim, M.A. Lisa, W.G. Lynch, G.F. Peaslee, M.B. Tsang, H.M. Xu, and F. Zhu, Phys. Lett. **B268** (1991) 6.

[spig 67] R.J. Spiger, and T.A. Tombrello, Phys. Rev. **163** (1967) 964.

[Sura 89] E. Suraud, C. Grgoire, and B. Tamain, Prog. Part. Nucl. Phys. **23** (1989) 357, and references contained therein.

[Tsan 89] M.B. Tsang, Y.D. Kim, N. Carlin, Z. Chen, C.K. Gelbke, R. Fox, W.G. Gong, W.G. Lynch, T. Murakami, T.K. Nayak, R. M. Ronningen, H.M. Xu, F. Zhu, L.G. Sobotka, D. Stracener, D.G. Sarantites, Z. Majka, V. Abenate, and H. Griffin, Phys. Lett. **220** (1989) 492.

[Vand 84] R. Vandenbosch, A. Lazzarini, D. Leach, D.K. lock, A. Ray, and A. Seamster, Phys. Rev. Lett. **52** (1984) 1964.

[Weis 37] V.F. Weisskopf, Phys. Rev. **52** (1937) 295.

[West 76] G.D. Westfall, J. Gosset, P.J. Johansen, A.M. Poskanzer, W.G. Meyer, H.H. Gutbroad, A. Sandoval, and R. Stock, Phys. Rev. Lett. **37** (1976) 1202.

[West 78] G.D. Westfall, R.G. Sextro, A.M. Poskanzer, A.M. Zebelman, G.W. Butler, and E.K. Hyde, Phys. Rev. **C17** (1978) 1368.

[Xu 86] H.M. Xu, W.G. Lynch, C.K. Gelbke, M.B. Tsang, D.J. Fields, M.R. Maier, D.J. Morrissey, J. Pochodzalla, D.G. Sarantites, L.G. Sabotka, M.L. Halbert, D.C. Hensley, D. Hahn, and H. Stocker, Phys. Lett. **B182** (1986) 155.

[Xu 89] H.M. Xu, W.G. Lynch, C.K. Gelbke, M.B. Tsang, D.J. Fields, M.R. Maier, D.J. Morrissey, T.K. Nayak, J. Pochodzalla, D.G. Sarantites, L.G. Sabotka, M.L. Halbert, D.C. Hensley, Phys. Rev. **C40** (1989) 186.

[Xu 92] H.M. Xu, P. Danielewicz, and W.G. Lynch, to be published.

[Zajc 84] W.A. Zajc, J.A. Bistirlich, R.R. Bossingham, H.R. Bowman, C.W. Clawson, K.M. Crowe, K.A. Frankel, J.G. Ingersoll, J.M. Kurck, C.J. Martoff, D.L. Murphy, J.O. Rasmussen, J.P. Sullivan, E. Yoo, O. Hashimoto, M. Koike, W.J. McDonald, J.P. Miller, and P. Truol, Phys. Rev. **C29** (1984) 2173.

[Zhu 91] F. Zhu, W.G. Lynch, T. Murakami, C.K. Gelbke, Y.D. Kim, T.K. Nayak, R. Pelak, M.B. Tsang, H.M. Xu, W.G. Gong, W. Bauer, K. Kwiatkowski, R. Planeta, S. Rose, V.E. Viola, Jr., L.W. Woo, S.J. Yennello and J. Zhang, Phys. Rev. **C44** (1991)R582

[Zhu 92] F. Zhu, W.G. Lynch, D.R. Bowman, R.T. de Souza, C.K. Gelbke, Y.D. Kim, L. Phair, M.B. Tsang, C. Williams, H.M. Xu, and J. Dinius Phys. Lett. **B282** (1992) 299